

POLITECNICO DI TORINO

Master of Science Program in
Energy and Nuclear Engineering

Master's Degree Thesis

Solid State Sodium Batteries: Synthesis and characterization of a sodium based composite electrode, in combination with NaSICON and glass-ceramic solid electrolyte



In collaboration with



Thesis advisors:

Prof. Monica Ferraris

Prof. Federico Smeacetto

Dr. Ing. Mihails Kusnezoff

Dr. Ing. Jochen Schilm

Candidate:

Federica Cappelletti

December 2020

Acknowledgements

I express all my thankfulness and gratitude to my academic supervisor Prof. Monica Ferraris and my co-supervisor Prof. Federico Smeacetto, they sparked my interest in advanced materials to be applied in the Energy field and suggested the opportunity of Master's Thesis at Fraunhofer Institute in Dresden.

I am grateful to my work supervisor Dr. Ing. Mihails Kusnezoff, to Dr. Ing. Jochen Schilm and to all the colleagues I worked with in the group of Joining Technology at Fraunhofer IKTS in Dresden: I improved my technical background and my practical skills, working in an extremely professional and challenging environment. I absolutely appreciated the possibility I had to attend the institute and the laboratories even during the first spreading of Corona Virus, coinciding with the starting of my research activity.

I am so grateful to my family, always supportive and encouraging to overcome the harder moments.

A special thanks to my beloved lifelong friends and to the new friends I met in these years and during this experience: they helped me to face problems with smile and from another perspective.

Finally, I could not forget to thank my boyfriend, on which I can always count and without which I would not be the same person now.

Table of contents

Introduction.....	I
Aim of the study	II
Chapter 1: State of the art	1
1.1 Working principle of a battery	1
1.2 Na-ion solid-state battery.....	4
1.3 Cathode material: sodium iron phosphate $\text{Na}_2\text{FeP}_2\text{O}_7$	7
1.4 Electrolyte materials: NaSICON and glass-ceramic Na07	11
1.5 Summary of the State of the art	15
Chapter 2: Experimental Methods	17
2.1 HSM analysis on glass powders	18
2.2 TGA-DTA analysis on glass powders	20
2.2 XRD analysis	23
2.3 FESEM and EDX analysis.....	25
2.4 Density measurement.....	28
2.5 Measurement of electronic conductivity.....	30
2.6 Electrochemical Impedance Spectroscopy analysis	32
2.7 Charge-discharge measurements of the cell	36
Chapter 3: Experimental Procedures	39
3.1 Synthesis of glass powders	41
3.1.1 Working principle of TURBULA [®] machine	41
3.1.2 Glass synthesis in oxidizing atmosphere	42
3.1.3 Glass synthesis in reducing atmosphere	44
3.1.4 Working principle of Vibratory Disc Mill and Planetary Ball Mill	45

3.2 Sintering procedure.....	48
3.3 Addition of carbon as conducting agent	51
3.4 Interface resistance to metallic sodium electrode	53
3.5 Preparation of cathode slurry and sintering on solid electrolyte	55
3.6 Battery cell assembly	57
Chapter 4: Results and Discussion.....	59
4.1 Sintering behaviour in air	60
4.1.1 HSM and TGA-DTA procedures in air	61
4.1.2 Sintering and phase formation in air.....	63
4.2 Sintering behaviour in nitrogen	70
4.3 Sintering behaviour in Varigon.....	74
4.3.1 HSM and TGA-DTA procedures in Varigon	74
4.3.2 Sintering and phase formation in Varigon	79
4.3.2.1 Optimization of sintering temperature and soaking time.....	87
4.4 Influence of carbon conducting agent.....	96
4.4.1 Addition of citric acid: HSM and Sintering in Varigon.....	96
4.4.2 Addition of graphite: HSM and Sintering in Varigon	101
4.5 Electrochemical characterization of solid electrolytes and half-cell composites ..	112
4.6 Electrochemical charge-discharge testing	123
Conclusions.....	128
References.....	130

Introduction

The current energy needs and the increasing demand for electricity raised the issue of energy production from diversified sources, to face the imminent problem of shortening of fossil fuels, of the environmental pollution and the emission of greenhouse gases into the atmosphere. Most of the renewable energy sources, as sun, wind, sea waves, are largely diffused in space and variable during time, requiring good systems of transmission and energy storage. It is predicted that in future the electricity generation from solar and wind sources will increase its competitiveness, due to programs of incentives and reduction of production costs [1]. Hence, the employment of electrochemical energy storage devices is the right solution to achieve balance between demand and supply of electricity, smoothing the electrical grid fluctuations and supplying power during peaks of energy demand. The rechargeable energy storage technologies are requested to be cheap and reliable, of easy production and maintenance, highly safe and environmentally friendly.

One of the first types of rechargeable devices, the lead-acid battery, is still largely employed because of its reliability and durability; nonetheless, it provides limited gravimetric and volumetric energy density, and the high toxicity of constituting components is a severe problem.

Among the various available technologies, the conventional Li-ion batteries are nowadays vastly utilized in the portable electronics market, because of the large energy density, output voltage and versatility in the choice of positive and negative electrode materials [2]. However, the use of liquid electrolyte reduces the quality and cycle life of the devices, exposing to risks of fires and explosions due to leakage and possible dendrites formation. Moreover, the uneven distribution of Lithium in remote or politically unstable areas of the globe will inevitably lead to an increase in cost of batteries in future.

Thus, a growing number of studies and investigations focus on the employment of solid-state batteries as suitable storage technologies in the long term. The risk of flammability and hazards related to undesired reactions are minimal, thanks to the presence of solid electrolytes: acting as mechanical separators, they guarantee structural and mechanical stability, and higher volumetric and gravimetric energy density, due to the increase in

compactness. The minimal wear and tear processes lead to long-cycle life, secure and reliable devices.

Aim of the study

The success of solid-state batteries strongly depends on the constituting materials for electrodes and electrolytes, and on the adoption of suitable eco-efficient synthesis processes. The Na-ion batteries are considered possible substitutes of Li-ion technologies, due to the natural abundance of sodium and to the similar electrochemical properties between the two elements. In fact, sodium is the second lightest and smallest alkali metal next to lithium, and shows the higher voltage after Li [3] (2.7 V for Na/Na⁺, 3.03 V for Li/Li⁺). The larger ionic radius leads to reduced energy density production compared with Li-ion batteries, anyway the intercalation processes are comparable and all the knowledge acquired in Li-ion investigation can be easily transferred in Na-ion solid-state batteries.

Among the several cathode materials, the polyanionic elements are the most widely studied, because of good ionic conductivity, long cycle stability and adjustable voltage properties [4]. Phosphates and pyrophosphates are particularly relevant, ensuring rapid conduction of alkali ions through the system, high thermal stability and good rate capability. The triclinic Sodium-Iron-Phosphate Na₂FeP₂O₇, with 97 mAh/g theoretical capacity for Fe²⁺/Fe³⁺ reaction, is reported to show good electrochemical performances when co-fired via glass-ceramic production with a β''-Al₂O₃ solid electrolyte [5]. The process, performed in reducing atmosphere, ensured a good coupling cathode-solid electrolyte without the application of pressure forces, and the creation of a strong electronic and ionic-conducting junction.

The goal of the study consists in the investigation of the most suitable sintering process to be applied to a batch of pulverised glass (Fe₂O₃ and NaPO₃ mix) for the realization of a glass-ceramic active cathode material. To increase the electronic conductivity, the batch

will be mixed with different amounts of conductive graphite. It is expected to create a crystalline structured cathode with composition similar to the triclinic $\text{Na}_2\text{FeP}_2\text{O}_7$, by regulating the heating parameters as atmosphere, heating rate, sintering temperature, soaking time. The effectiveness of process is verifiable from the good material densification during the sintering step, the high percentage of crystalline phases over the amorphous ones and the presence of Fe^{2+} in the structure, indicating the construction of the proper crystalline scaffold necessary for Na^+ migration. Following the research of Yamauchi et al., the explored procedure has to be applied for the co-firing of cathode material on a disk of solid-state electrolyte (the experimental work focuses on a glass-ceramic and on a NaSICON-type electrolyte). The stack, to be coupled with metallic Na as anode, will be investigated with charge-discharge measurements, to validate the possibility of electrochemical activity and the effectiveness as a storage device.

Chapter 1: State of the art

1.1 Working principle of a battery

A battery is an electrochemical system aimed at producing useful electrical power and energy from a redox chemical reaction. The chemical species involved are exchanged between two electrodes: during the discharge phase, the negative electrode is the anode, at which the oxidation reaction occurs, the positive is the cathode, where reduction reaction takes place. The ions originated are transported through the electrolyte, a medium with high ionic and poor electronic conductivity; the electrons instead, move through external connections. During discharge, the internal chemical energy spontaneously decreases and some electrical energy is produced; conversely, in the charge phase some electrical energy is spent to increase the internal chemical energy of the batteries. Based on this aspect, they are divided in two categories: the primary batteries (as Zn/MnO₂ alkaline cells), only subject to discharge mode and next discarded, and the secondary or rechargeable batteries, for which it is possible to discharge and charge the system several times, depending on the constituting materials, components and the working principle.

In major part of batteries, the chemical reactants and products are already present and enclosed in the device. The two electrodes must be characterised by good electronic conductivity and high ionic conduction, occurring through intercalation and extraction mechanisms in the volume of the structure. An exception is constituted by the flow batteries (as Vanadium Redox Flow Batteries [6]), rechargeable semi-open cells in which electrodes are ionic aqueous solutions pumped into the system from external vessels. Being the solutions electronic insulators, the electrical conductivity is guaranteed by some graphite felt, wet by the ionic solution and providing contact to the solid electrolyte on one side, to the current collectors on the other. Those devices are advantageous because of their long life, due to the absence of electrode volumetric deformation during the charge-discharge phases.

It is necessary to have highly electropositive anode electrodes: the oxidation potential, indicating the tendency of the chemical element to donate electrons and form positively charged ions, is a fundamental parameter to take into consideration.

The cathode electrode must contain elements easy to get reduced (or oxidised, in the charge phase) and must have a high electrochemical window.

The electrolyte material can be of liquid or solid type. The former consists in a solution of solvent with dispersed conductive salt, providing good ionic conductivity thanks to solvation/de-solvation processes and penetrating at the interface with electrodes. Nonetheless, it limits the battery life due to the continuous shear; moreover, the possibility of leakage and dendritic growth at interface lead to risks of fires, runaway reactions and explosions. The solid-type electrolyte ensures the ionic conductivity with ionic diffusion mechanisms in the lattice, and provides higher mechanical, chemical and thermal stability; even if the possibility of dendrite growth is limited, the interface still represents the main bottleneck in the conduction of ions.

The following image represents the main components for a common rechargeable solid-state device (Fig. 1.1).

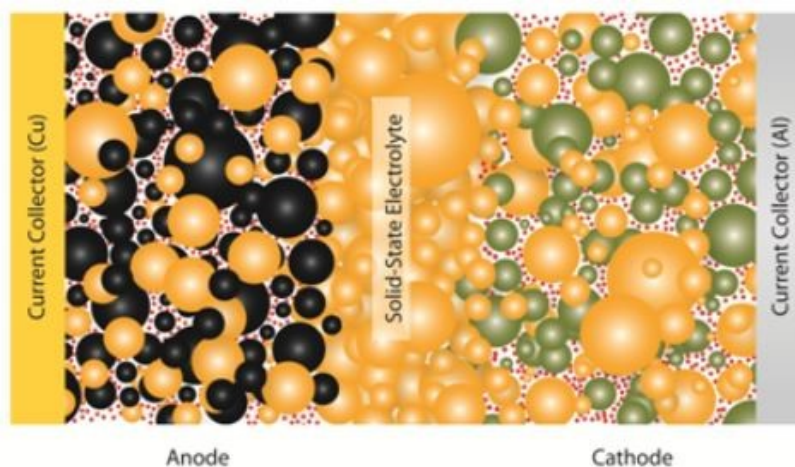


Figure 1.1 – Example of solid-state battery with the main components: the solid-state electrolyte (in orange), the composite cathode (with active material in green and conductive additive in red), the anode active material (in black)
(Source: <http://smeng.ucsd.edu/supercapacitors/>)

The main important parameters to be considered when dealing with batteries are the operating voltage, depending on the starting open circuit voltage and on the characteristic polarization effects of the device, and the capacity, extensive parameter indicating the

quantity of charge cumulated or released from the cell (usually measured in mAh/g). According to voltage and capacity, the energy density and the power density are defined with respect to the mass or volume of active material in the battery. As already mentioned, the good electrodes electronic conductivity and the high ionic conductivity of electrolyte are fundamental tasks. Moreover, a good battery is required to have small self-discharge during non-operation moments, high cycle life (high number of cycles the cell can be operated through, before its capacity becomes too degraded) and high rate capability, hence being able to keep high production efficiency even at high current loads, without suffering from polarization effects.

1.2 Na-ion solid-state battery

The Sodium-ion batteries are electrochemical cells characterised by sodium-conducting electrolyte and electrodes. The working principles and intercalation mechanisms are basically the same of the more common Li-ion batteries, highly employed nowadays because of their long lifetime, high capacity and output voltage, and large energy density. Lithium and sodium are both alkaline elements, highly electropositive and defined by similar redox potential (3.03 V for Li/Li⁺, 2.7 V for Na/Na⁺). The higher density and radius of elemental Na hinder the intercalation processes, resulting in limited energy densities and lower electrochemical performance compared to the same battery employing Li-ions. Despite that, sodium is cheap and naturally abundant, representing a solution to the scarce availability and the growing price of lithium, extracted from socially and politically unstable areas of the globe.

The commercially available sodium batteries are the Na-S batteries and the ZEBRA devices (Zero Emission Battery Research Activity) [7]. Promising candidates for stationary applications and electrical battery vehicles, they provide high voltage and high gravimetric energy density, with no emissions, small self-discharge and low maintenance requirements. The Na-S batteries are cells of tubular shape, constituted by internal sodium anode and external sulphur cathode, both in molten state, spaced-out by a β'' -Al₂O₃ solid electrolyte. The structure is visible in Fig. 1.2. In order to keep the electrodes in liquid state and increase the ionic conductivity, the cell works at high temperature (300 °C). This aspect raises the problem of safety in case of leakage of electrodes material, or of rupture of the solid electrolyte, with possible fire or explosion hazards; the high corrosive environment requires good sealings and highly resistive containers. Additionally, the need for thermal devices to constantly guarantee the thermal equilibrium constitutes an additional cost.

The ZEBRA cells have a similar configuration, with liquid sodium as anode element, β'' -Al₂O₃ solid electrolyte and a metal chloride cathode, usually NiCl₂, formed by Ni and NaCl porous structure and impregnated with NaAlCl₄ as second electrolyte in molten state. The battery operates at high temperature to ensure the better ionic conduction and to keep the molten state, but produces higher voltage than the Na-S cells. Moreover, it is

intrinsically safer, because of corrosiveness reduction due to the mainly solid state of cathode material. Nonetheless, the battery faces several problems, as the formation of low-conducting NiCl_2 during time, its solubility in melted NaAlCl_4 and the reduced cycle life.

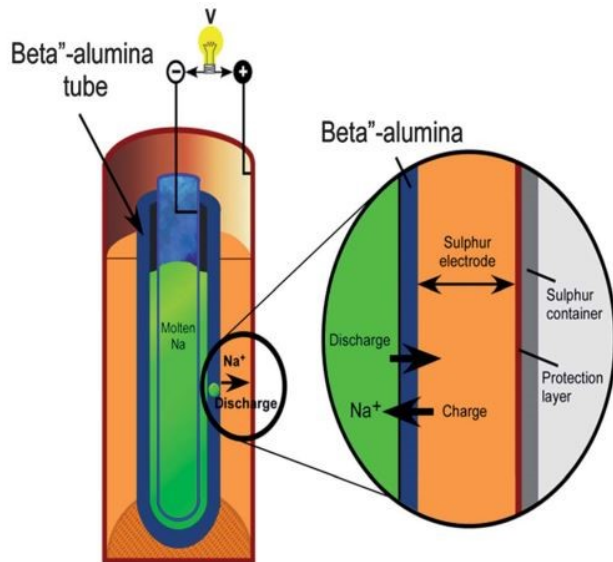


Figure 1.2 – Schematic structure of Na-S battery

(Source: Karina B. Hueso, Michel Armand and Teófilo Rojo, *High temperature sodium batteries: status, challenges and future trends*, Energy Environ. Sci., 2013, 6, 734)

Thus, the current investigations and studies aim at focusing the attention on solid-state Na-ion batteries, working at ambient temperatures, with solid electrodes and solid electrolyte separator. With solid state components, the net weight and volume would be considerably reduced, increasing the energy density output. A solid-state battery is intrinsically compact, mechanically and structurally stable, minimizing vibrations and shear effects, hence with a possibly longer cycle life and higher reliability with respect to a conventional liquid electrolyte device. The different contact at the interface with electrolyte and electrodes makes possible the reduction of self-discharge, leading also to a more uniform output voltage [8].

The analyses on Na-ion solid-state batteries consider the possibility of employment of different materials for anode, cathode and solid electrolyte [9].

Concerning the negative electrode, the metallic Na is one of the possible candidates, due to its high redox potential and ease in Na^+ intercalation, even if the interface aging

problems and the possible dendrites formation still represent a severe issue. Other examined alternatives are the amorphous carbon (the disordered internal structure is suitable for Na^+ hosting and provides good electrical conductivity), metal alloys (as Sb alloys with Na, providing large reversible capacity and high energy density) and phosphates (the NaSICON $\text{Na}_3\text{V}_2(\text{PO}_4)_3$ or $\text{Na}_3\text{Ti}_2(\text{PO}_4)_3$ are possible materials).

Regarding the solid electrolytes, the most investigated are the β'' - Al_2O_3 , the NaSICON structure $\text{Na}_3\text{Zr}_2\text{Si}_2\text{PO}_{12}$ and glass-ceramic materials as Na_3PS_4 . The former, good ionic conductor even for ambient temperature applications, allows the Na^+ migration in its two dimensional layered structure. The NaSICON electrolyte guarantees good ionic movement thanks to the 3D channels formed in the monoclinic framework, and is chemically and thermally stable. The glass-ceramic material provides relevant ionic conductivity and small resistance to the grain boundaries present in its stable cubic structure. A deeper and more accurate analysis on solid electrolytes will be discussed in chapter 1.4.

For cathode materials, several options have been taken into consideration: among them, the mostly examined are the oxide materials, the organics and the polyanionic compounds [4]. An example of oxide cathode is NaCrO_2 , reported to have comparable good cycling performances to the ones of Li-ion batteries with an identical structure [10]; nevertheless, oxides are characterised by small ionic conductivity, high sensitivity to moisture and structural instability, penalizing their cycle durability. Organics are easily synthesized and environmentally friendly, but lack electronic conductivity and provide low energy density. The polyanionic compounds are the most interesting and widely studied, because of their excellent voltage and cycle properties. Phosphates and pyrophosphates, in particular, will be analysed in the following chapter.

1.3 Cathode material: sodium iron phosphate $\text{Na}_2\text{FeP}_2\text{O}_7$

Thermal and chemical stability, fast charge-discharge response over a prolonged usage, proper energy density production are the main characteristics expected from a good solid-state battery. As anticipated, the polyanionic compounds are one of the more promising and studied materials for positive electrode, since meeting the requirements in terms of stability, ionic conductivity and cyclability [4]. The cell structure is generally composed of MeO_x polyhedra (where Me is a transition metal as Fe, Mn, Co) linked to $(\text{XO}_4)^{n-}$ tetrahedra (where X can be Si, S, P). The tetrahedral group is the one ensuring the rapid conduction of alkali ions in the lattice and enhances the structural stability during the redox process, reducing therefore the volumetric changes with intercalation and extraction of ions. The X-O bond increases the stability of oxygen atoms in the framework and positively influences the ionic character of Me-O bond.

The sulphates, phosphates and pyrophosphates are the main investigated systems, due to their temperature stability, excellent rate capability and cycle life: the last two in particular, are presented as optimal electrode components because of higher crystallinity and the higher stability with increase of temperature with respect to the sulphates.

Among several compounds, the triclinic stoichiometric $\text{Na}_2\text{FeP}_2\text{O}_7$ is the considered structure for the experimental investigation. It is preferred to other polyanionic elements, as fluorophosphates $\text{Na}_2\text{FePO}_4\text{F}$ or vanadium phosphates $\text{Na}_3\text{V}_2(\text{PO}_4)_3$, because produced starting from cheap and highly available raw materials (Fe_2O_3 and NaPO_3), environmentally friendly and non-toxic. Its $\bar{P}1$ crystalline framework is constituted by FeO_6 octahedra and PO_4 tetrahedra, sharing edges and corners in staggered way: in opposition to compounds as the maricite-type NaFePO_4 , which creates isolated sites for Na^+ ions, hence a large barrier to the sodium migration [11], the $\text{Na}_2\text{FeP}_2\text{O}_7$ forms 3D large tunnels for movement and intercalation of the positive ions. Compared with an isostructural pyrophosphate $\text{Na}_2\text{MnP}_2\text{O}_7$ produced with same solid-state reaction [12], the iron-rich structure presents better cyclic stability and higher capacity, demonstrating to be a more suitable cathode material.

The electrochemical reaction advances between the discharged state of iron (Fe^{2+}) and the charged one (Fe^{3+}). For the cathode electrode, the reaction is the following:



The theoretical capacity is reported to be 97 mAh/g. The structure shows good performances during electrochemical measurements with liquid and aqueous electrolytes, reaching values of reversible capacities almost of 90 mAh/g during the first cycles [3]. The following figure (Fig. 1.3) depicts the crystalline structure of $\text{Na}_2\text{FeP}_2\text{O}_7$ and typical curves from electrochemical measurements: two plateaux are noticeable in the curves, the principal around 2.9 V and the second at 2.5 V, indicating reactions of ionic extraction from Na sites in the crystalline lattice.

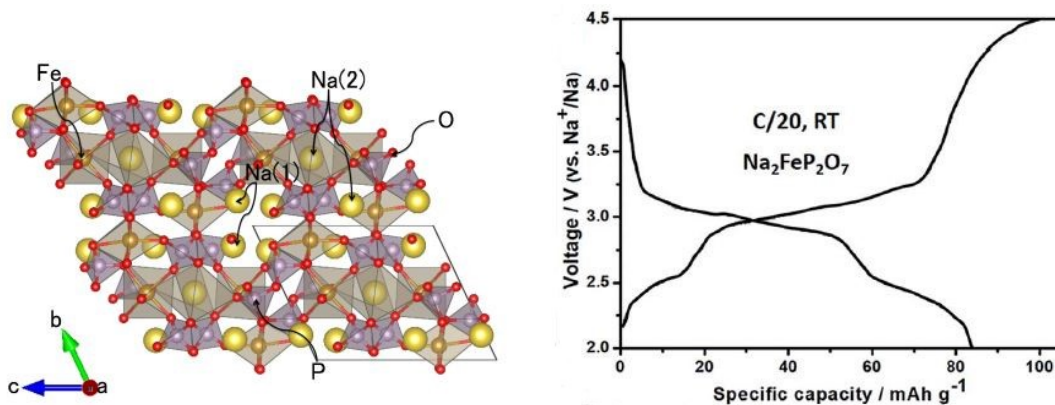


Figure 1.3 – On the left, crystalline structure of $\text{Na}_2\text{FeP}_2\text{O}_7$ cathode material: the FeO_6 octahedra (brown) and PO_4 tetrahedra (purple) create 3D tunnels for the movement of Na^+ ions (yellow)

(Source: T. Honma, T. Togashi, N. Ito and T. Komatsu, *Fabrication of $\text{Na}_2\text{FeP}_2\text{O}_7$ glass-ceramics for sodium ion battery*, Journal of the Ceramic Society of Japan 120 (2012), 344-346).

On the right, voltage-capacity curves for $\text{Na}_2\text{FeP}_2\text{O}_7$ as cathode material, working at C-rate C/20 and room temperature

(Source: Y. Niu, Y. Zhang, M. Xu, *A review on pyrophosphate framework cathode materials for sodium-ion batteries*, Journal of Materials Chemistry A 7 (2019), 15006-15025).

The material achieves also high performances when coupled with a solid electrolyte and operated at room temperature [5]. The electronic conductivity, issue affecting almost all the polyanionic compounds, is enhanced with the addition of carbon as conducting agent (acetylene black, citric acid, graphite) to the sodium-iron-phosphate. With a solid-state

electrolyte, the electrodes are not wetted by the ionic conducting medium: hence, the ionic conductivity is enhanced by intercalation of electrolyte powders in the batch.

The aim of the experimental investigation is to prove what previous studies report: the effective active cathode electrode is produced as glass-ceramic material, starting from an amorphous form and heating with controlled crystallization process. It is joined to the solid electrolyte via sintering heating treatment: the milled amorphous active powders undergo densification thanks to viscous flow mechanism, next face crystallization via steps of nucleation and crystal growth.

The procedure is advantageous with respect to a common solid-state reaction: it allows to simultaneously integrate the carbon conducting agent and the electrolyte powders, and to spend less energy and time in heating. For a glass-ceramic route, crystallization occurs above the glass transition temperature T_g (indicating the change of glass material characteristics, from brittle and amorphous behaviour, to viscous and rubbery state the higher is the temperature); for solid-state reaction, the calcination temperature to crystallize the same material would be certainly higher.

According to the Frenkel's theory of viscous flow [13], the sintering process is initially describable approximating the batch of pulverized parent glass as a group of spheres of same dimensions. When some heat is provided and the temperature is above T_g , the atomic motion is promoted and the particles tend to converge forming some contact points. Due to the viscous flow, more material is transported into the neck region between spheres, contributing to the neck growing and increasing the density of the batch. The procedure is illustrated in Fig. 1.4.

When the radius of necks is comparable to the radius of particles, the Scherer's cylinder model describes the completion of sintering: the compact is approximated as a cubic arrangement made of intersecting cylinders, indicating the particles rows and with average radius corresponding to the average one of particles. With the proceeding of heating process, the cylinders get thicker and shorter, contributing to higher densification and isolating the present pores. The smaller particle size and the uniformity are helpful to promote sintering and densification, leading to a less porous structure. Also the heating atmosphere, as well as heating rate, soaking time and sintering temperature, influence the density increase.

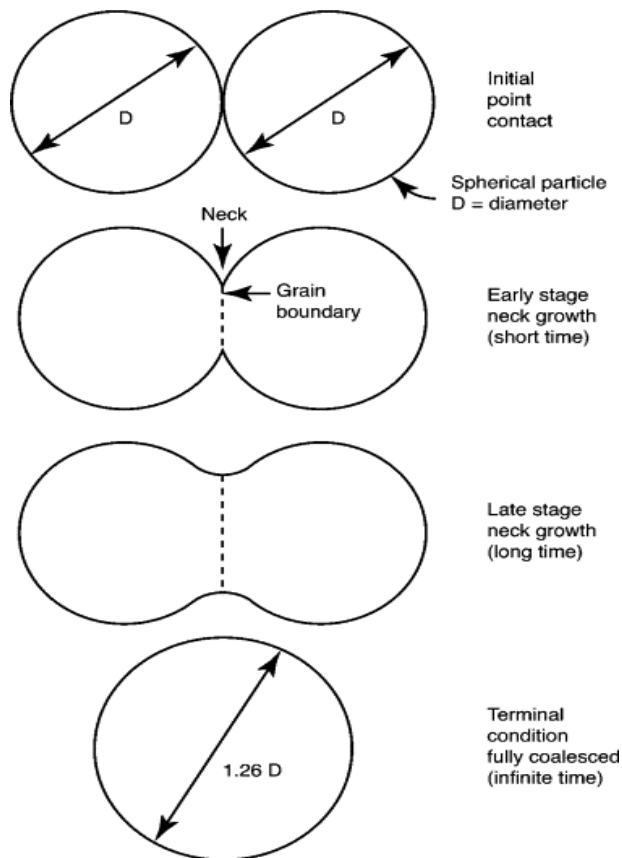


Figure 1.4 – Sintering model for two spheres with neck growing between them, to the point they form a single sphere with higher dimensions
 (Source: Fang Zhigang Zak, *Sintering of Advanced Materials – Fundamentals and Processes*, 2010)

With further heating treatment, the crystallization of particles is promoted and the densification process hindered. Crystallization starts with heterogeneous nucleation, consisting in the formation of stable small crystals in preferred nucleation sites, in which the energy received is sufficient to overcome the formation energy of crystalline embryos. Fostered by longer heating time, high temperature and small particle size, the embryos tend to aggregate in nuclei, centres of crystallization. Crystallization is completed with the addition of atoms and molecules by diffusion, hence with crystalline growth and finally, with the formation of solid crystalline grains. The higher the number of nucleation sites, the many the grains formed at the end of the process.

Hence, the desired conducting framework in the cathode electrode can be realised with sintering procedure, starting from the consolidation of parent glass, then with the densification of particles and the formation and growth of crystalline grains.

1.4 Electrolyte materials: NaSICON and glass-ceramic Na07

The solid state electrolyte material is employed in Na-ion batteries as substitute of liquid electrolyte, due to safety issues as risk of flammability, explosion and leakage. A good solid electrolyte must be environmentally friendly, of easy preparation and with high compatibility with electrodes materials. Fundamentals are the high ionic conductivity and negligible electronic conductivity (to avoid the risk of short circuit), the good thermal and chemical stability, the strong mechanical properties and ability to inhibit the dendrite growth at interface with anode element. Due to high degree of compactness, the use of a solid electrolyte ensures higher gravimetric and volumetric energy density, minimization of wear and vibrations, small self-discharge and wider voltage window.

The major challenge for solid electrolytes to be co-sintered with cathode materials, as in the following study, is the reduction of impedance through the inner grain boundaries, but especially at the interface with electrodes. Differently to the conventional electrolytes in fact, there is no possibility of liquid penetration into the electrodes, and the satisfactory ionic conductivity must be achieved with a properly structured electrolyte material and through the intercalation of electrolyte powders in the framework of electrode.

The polycrystalline beta-alumina solid electrolyte (β'' -Al₂O₃), successfully utilised in high-temperature Na-S and ZEBRA batteries, has ionic conductivity about $2.0 \cdot 10^{-3}$ S/cm at ambient temperature and 0.2-0.4 S/cm at 300 °C [14]. It has been tested in association with NFP cathode material, mixed with 25 %wt. solid electrolyte powders and 3 %wt. conductive acetylene black, demonstrating good electrochemical performance during charge-discharge measurements at T_{amb} [5]. Its rhombohedral disposed lattice is formed by stacked Al-O spinel blocks and conduction planes, along which the Na⁺ migration occurs (Fig. 1.5). Despite the good electrochemical properties, the electrolyte is sensitive to moisture and thermodynamically unstable: the preparation via solid-state reaction, in fact, leads to the formation of impurities as β -Al₂O₃ and NaAlO₂, cause of the scarce mechanical strength of the material. The toughness of β'' -Al₂O₃ is reported to be

enhanced by incorporation in the matrix of ZrO_2 element, which anyway is a scarce sodium conductor and would probably hinder the electrolyte ionic conductivity.

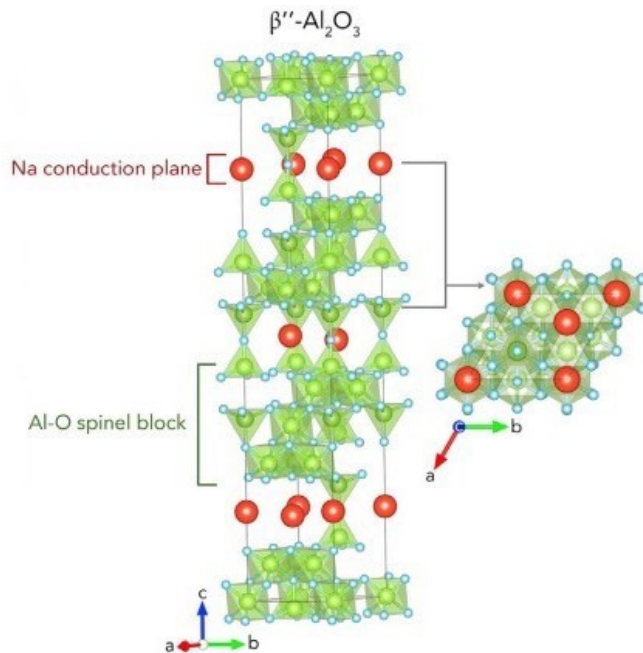


Figure 1.5 – Crystalline structure of $\beta''\text{-Al}_2\text{O}_3$, with spinel blocks and conduction planes alternatively stacked
(Source: Yong Lu, Lin Li, Qiu Zhang, Zhiqiang Niu, Jun Chen, *Electrolyte and Interface Engineering for Solid-State Sodium Batteries*, Joule 2 (2018), 1747–1770)

The electrolyte materials employed in the following investigation have a different structure: the Na07 is a glass-ceramic material, the NaSICON-type electrolyte is a Sodium-Super-Ionic-Conductor with monoclinic structure.

The Na07 electrolyte is composed by 57.1 %mol. SiO_2 , 35.7 %mol. Na_2O , 7.2 %mol. Y_2O_3 , sintered in air atmosphere with heating rate of 5 K/min to 1170 °C: the resulting glass-ceramic tablets are dense, chemically and thermally resistant, hence suitable to be co-fired with the active cathode element without undesired reactions. The HSM procedure (Fig. 1.6) proves that the batch, up to 800 °C, is not subject to linear shrinkage. From previous experiments in IKTS, the ionic conductivity results to be in the range $10^{-4} \div 10^{-3}$ S/cm at ambient temperature.

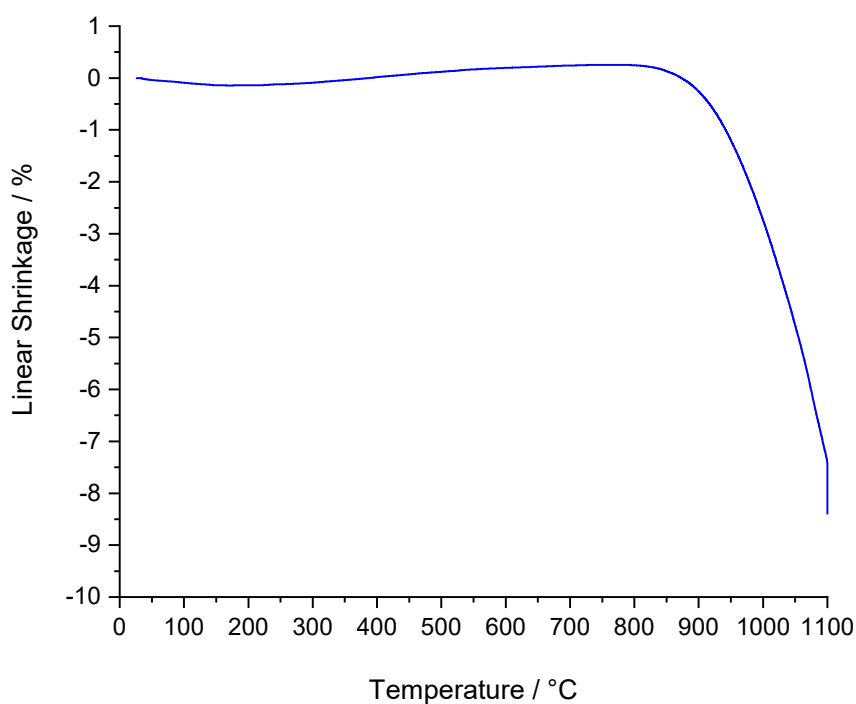


Figure 1.6 – HSM procedure applied to Na07 samples, heated to 1100 °C
(Source: IKTS)

The NaSICON-type solid electrolyte, whose chosen chemical composition is $\text{Na}_3\text{Zr}_2\text{Si}_2\text{PO}_{12}$, consists in a monoclinic structure formed by PO_4 and SiO_4 tetrahedra, sharing corners with octahedral ZrO_6 and forming 3D tunnels for Na ions movement (Fig. 1.7). During operation, the conductor cations move from one site to another passing through some bottlenecks, whose size is dependent on the crystalline skeleton and must be sufficiently large to promote the ionic conduction. The highly dense and stable framework is created by solid-state reaction procedure: starting from bulk powders, the slow process includes a phase of de-hydration up to 550-600 °C, next a phase of calcination at around 700 °C and finally a long phase of sintering, for temperatures higher than 1200 °C. It is proved that the high sintering temperature and the prolonged holding time promote the increase in grains size, hence reducing the amount of grain boundaries and the resistance to ionic movement through them [7]. The ionic conductivity of material, dependent on the fabrication process, in this case is around 10^{-3} S/cm at ambient temperature, hence closed to the conductivity of β'' - Al_2O_3 . As the Na07, also the

NaSICON material is expected not to react with cathode during the co-sintering procedure, but forming a tough, stable and ionic conductive physical separator.

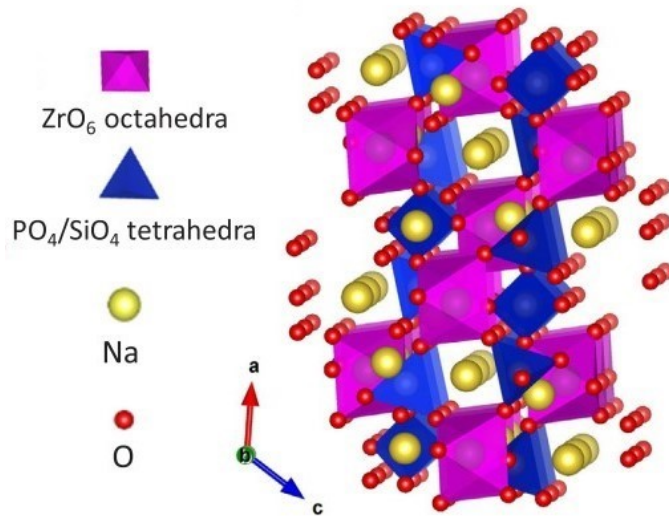


Figure 1.7 – NaSICON monoclinic structure, forming 3D channels for Na⁺ transport
(Source: Wenru Houa, Xianwei Guoa, Xuyang Shena, Khali Amineb, Haijun Yua, Jun Lu, *Solid electrolytes and interfaces in all-solid-state sodium batteries: Progress and perspective*, Nano Energy 52 (2018), 279-291)

1.5 Summary of the State of the art

The global market requires cheap, reliable and non-polluting solutions for storage and supply of electrical energy. The rechargeable sodium-ion solid-state batteries can meet the requirements, due to the low cost of sodium extraction and to the similar working mechanisms with the Li-ion technologies. The ambient working temperature allows to avoid additional thermal management problems, as in case of Na-S and ZEBRA-type sodium batteries. The solid electrolyte material, which must guarantee high thermal and chemical stability and good ionic conductivity, has to be produced with high temperature processes, so that the number of grain boundaries (bottlenecks for ions to move) is as low as possible. Concerning the electrode material, the glass-ceramic sodium-iron-phosphate $\text{Na}_2\text{FeP}_2\text{O}_7$ results a good conducting framework, with high cycle life and electrochemical stability. The intrinsic low electronic conductivity is compensated by addition of electrical conducting agent to the batch, the ionic conductivity is enhanced with intercalation of electrolyte powders.

The challenge to be faced in the experimental work is the realization of cathode electrode via glass-ceramic route, on a layer of glass-ceramic or NaSICON solid-type electrolyte. In conventional investigations, the electrolyte material is co-fired or distributed on the cathode active material, already provided; in the following study instead, the task consists in creating the cathode element starting from its amorphous phase, sintered and crystallised on the stable solid electrolyte layer. Starting from inexpensive raw materials and from the creation of parent glass via melt-quenching, the purpose is to promote the densification of composite powders on the electrolyte, in order to form a strong junction and to reduce the impedance at the interface. With further heating, the intent is to boost the crystallization of cathode material and the formation of ordered conductive channels for motion of Na^+ ions during the normal battery operation.

The study attempts to prove the effectiveness of sintering procedure for the creation of an active electrode, properly working with a solid electrolyte and with metallic Na anode. With that goal, it is necessary to vary several heating parameters to find the optimal combination for sintering. The sintering atmosphere, leading to oxidation or reduction

effects, has an influence on the material densification and on the valence state of forming elements: it is reported that reducing conditions are the more effective in densification and creation of the proper atomic active scaffold. The high sintering temperature affects the type and amount of crystalline phases. The long holding time at high temperature promotes the molecular diffusion, inducing to more crystals formation in the composite structure.

Chapter 2: Experimental Methods

The amorphous sodium-iron-phosphate powders have been produced by conventional melt-quenching method (Chapter 3.1). After that, the material reactivity in the heating process has been verified by means of Hot Stage Microscopy (HSM) and Differential Thermo-Gravimetric Analysis (TGA-DTA).

Some coin-shaped samples have been created by mechanical pressing, and the density has been calculated starting from the sample mass, measured with a laboratory scale, and sample geometry, measured with a calliper. The same measurement has been carried out after the sintering process.

Subsequently, X-Ray Powder Diffraction method (XRD) has been performed on the as-fired grinded samples, to investigate the crystalline structure and explore what is the contribution of the different crystalline phases in the diffracted spectrum generated.

Energy-Dispersive X-Ray Spectroscopy (EDX) and Field-Emission Scanning Electron Microscopy (FESEM) have been helpful in the chemical characterization of samples, allowing a deeper focus on the forming elements of each structure, on their concentration and on their distribution internally to the lattice.

The sintered samples have been gold sputtered on the surface and the electronic conductivity has been measured by contact with a multi-meter; hereafter, the measurement has been repeated with the same samples coated with silver conductive paste.

Electrochemical Impedance Spectroscopy analysis (EIS) has been performed to quantify the interface resistance with sodium metallic layer and with cathode active material.

Finally, the electrochemical activity of the created battery has been investigated with some charge-discharge measurements, made both with a conventional liquid electrolyte, and with the solid electrolytes under investigation.

2.1 HSM analysis on glass powders

When dealing with glass-ceramics production, it is important to focus on the temperature dependence and on the effect of the heating procedure on the specimen. The Hot Stage Microscopy is a technique employed to perform qualitative analysis on the material specimen: with a single experiment, it is possible to extract information about the linear shrinkage of the sample, to detect characteristic temperatures as the onset temperature for densification, the one of maximum deformation and the melting temperature, and to make studies about sample wettability and coefficient of thermal expansion.

The microscope (Hesse Instruments) is constituted by a heating furnace, working in controlled atmosphere and water cooled; the powders under investigation are pressed and located internally to the heating chamber, in contact with a thermocouple.

A light source hits the sample, whose shadowed image is projected on the opposite side and, for each variation of temperature, collected by a camera; the pictures are transmitted to a computer program, which elaborates them and performs the necessary calculations.

The working scheme is showed in the figure below (Fig. 2.1).

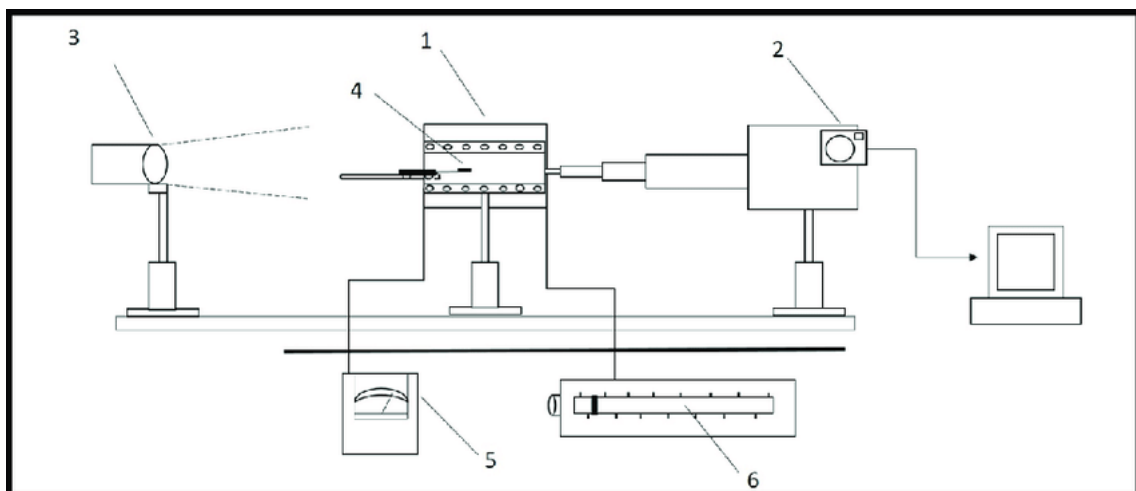


Figure 2.1 - Scheme of HSM working bench: 1-Electric furnace; 2-Camera for image and video recording; 3-Light source; 4-Specimen on thermocouple; 5-Temperature controller; 6-Heating system

(Source: J. Pawlik, K. Cholewa-Kowalska, Temperature behaviour of ceramic biocomposites investigated via Hot-Stage Microscopy, *J. of Polish Society for Biomaterials and Faculty of Material Science and Ceramics* (150), 22-28)

The images received, showing the cylindrical sample as a 2D rectangle, are interpreted by the software EMI III (Hesse Instruments), which simultaneously elaborates the axial and radial variations on the shadowed images during the heating process.

The Linear Shrinkage is represented in a graph with respect to the heating temperature: it is possible to distinguish the onset temperature for the densification, the one of maximum densification and the softening temperature.

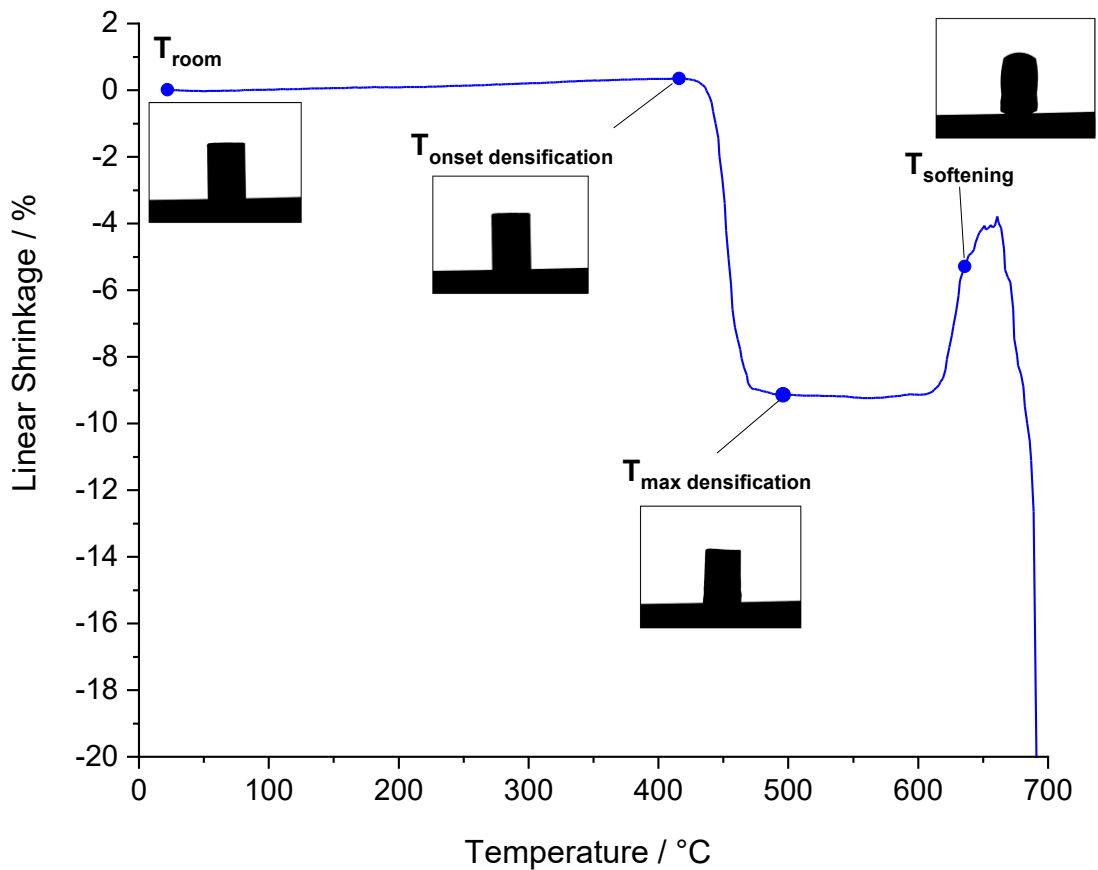


Figure 2.2 – Graph of linear shrinkage in function of temperature; the curve is associated to the shadowed images collected by the camera during the heating process (Source: IKTS)

2.2 TGA-DTA analysis on glass powders

The Differential Thermo-Gravimetric Analysis is a combination of two different measurements, performed at once in the same machine (Netzsch-Gerätebau GmbH): the Differential Thermal Analysis detects the temperature variation during a heating procedure, comparing the desired specimen with respect to a reference refractory sample; the Thermo-Gravimetric Analysis measures the mass variation of the specimen in the same heating process.

Hence, the obtained graph allows identifying the range of temperatures in which the phase transition occurs, together with the presence of possible side reactions (such as evaporation or oxidation) by analysing the mass reduction trend.

The device is composed of two symmetrically disposed Platinum crucibles, filled with few milligrams of the desired sample and the reference one, both in form of powders. They lay in a heating chamber and are controlled by two thermocouples and by a precision balance, detecting their temperature and mass during the heating process. The thermocouples are connected to a voltmeter, registering a deflection ($\mu\text{V}/\text{mg}$) each time a temperature variation between the studied sample and the refractory takes place. The chamber can be filled with different gases, to investigate oxidation and reduction effects. The temperature variation control is made by a software, which collects and elaborates each measurement.

A generic scheme is illustrated in Fig. 2.3.

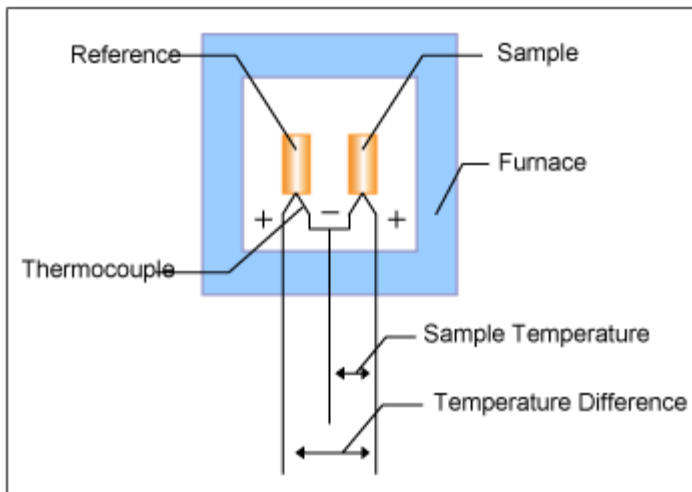


Figure 2.3 – Working scheme of furnace for TGA-DTA measurements
 (Source: Gen Consulting Company, Global Differential Thermal Analysis Market Outlook 2019-2027 (2018))

The measured voltage deflection and the mass loss are combined in a graph in function of the heating temperature (Fig. 2.4). If dealing with a glass sintered to a glass-ceramic, from the former curve are generally expected three different zones: a first one represented by an endothermic trend, ending with the onset temperature for the start of densification (T_g) and viscous flow; a successive exothermic peak, related to the progressive crystallization of structure up to the maximum crystallization at T_c , and finally a following endothermic peak connected to the gradual heating and melting of batch.

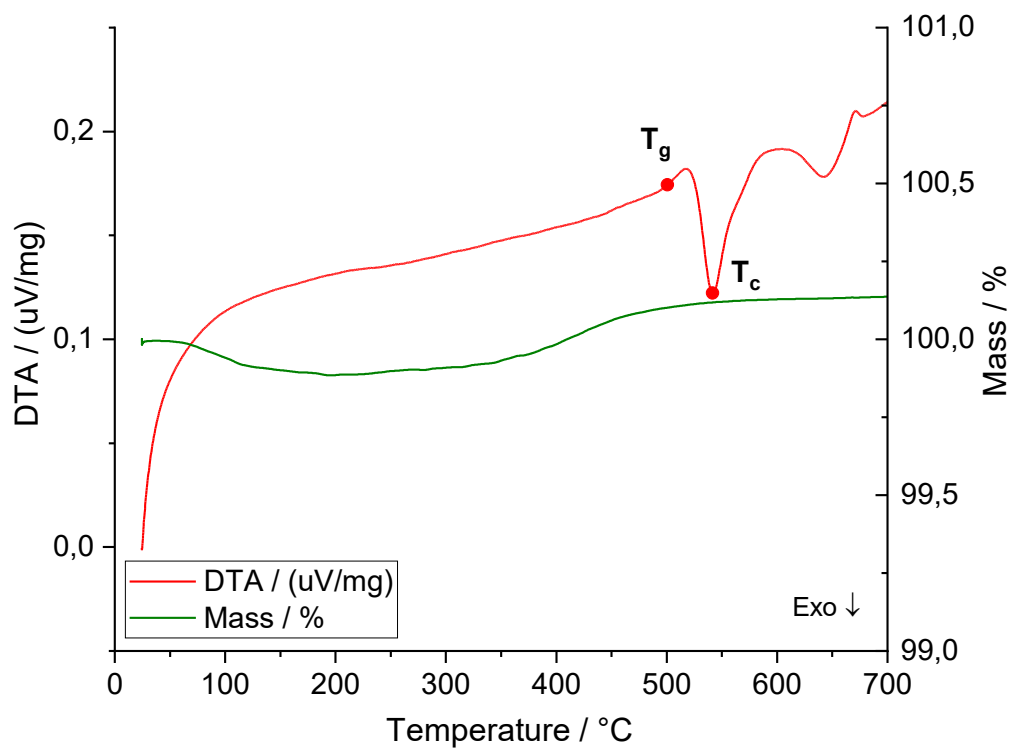


Figure 2.4 – Differential Thermal Analysis curve (in red) and percentage mass loss curve (in green) in function of temperature (Source: IKTS)

2.2 XRD analysis

The X-Ray Powder Diffraction is one of the most accurate methods for analysing the chemical composition and crystalline structure of a given material: it consists in hitting the pulverised sintered sample with X-Rays and measuring the diffraction angle and the intensity of the diffracted X-Ray waves into the structure. The created diffractogram is studied in comparison to the diffraction paths generated by several crystalline structures, with the aim of characterising the material in terms of crystalline content with respect to the amorphous content.

Cu K α X-Rays are the radiation source. After being generated, the X-Ray beams hit the sample surface and penetrate internally, where they reflect on the constituting crystalline structure.

The lattice can be imagined as a sequence of parallel planes [15]. If two beams are considered, the condition for the diffraction to occur is to have constructive interference: the waves will be summed in phase if they have the same path length, or if the difference in their path lengths is equal to a multiple of their wavelength. This aspect is described by the Bragg equation (Eq. 2.1):

$$\delta = 2d \sin \theta = n\lambda \quad (2.1)$$

where δ is the difference in the path lengths, θ is the angle formed by the outgoing ray with the crystalline plane, d is the distance between planes, λ is the wavelength (Fig. 2.5).

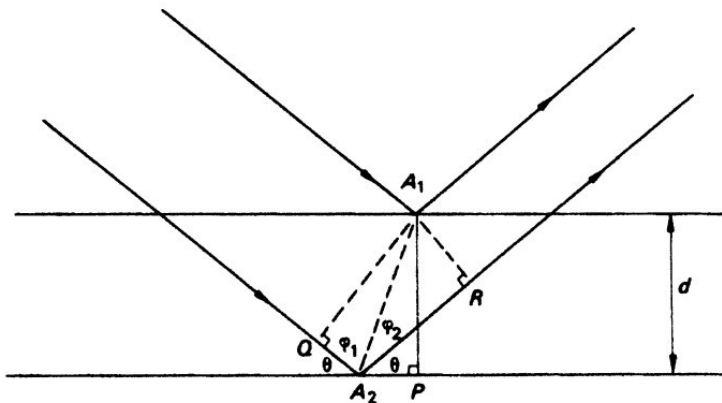


Figure 2.5 – Schematic representation of two crystalline planes, with collision of X-Ray beams (Source: Structure Determination by X-ray Crystallography – Analysis by X-rays and Neutrons, Springer)

The diffracted X-Ray beams are recorded outside of the sample by a detector and transmitted to a software, which elaborates in a graph the intensity of diffracted peaks in function of the angle formed by beams with the crystalline planes.

The software DIFFRAC.SUITE EVA is the tool employed to analyse the PDF (Powder Diffraction Files) and to detect what crystal phases are responsible for the generated patterns. The shape and dimension of the crystalline unit cell are deduced from the position of the Bragg reflections, the content of the unit cell from the intensity of diffracted peaks. With reference to a database, different crystalline patterns are overlapped to the one under investigation, in order to identify the real crystalline phases constituting the sintered material.

The study is made in combination with DIFFRAC.SUITE TOPAS, a graphics-based profile analysis program, exploiting a mathematical fitting algorithm to calculate the weight percentage of crystalline structures in the sample. The program cannot detect nor calculate the presence of residual amorphous phases: indeed, those phases have no parallel planes, hence X-Ray beams passing through them cannot originate constructive interference and no reflexes are generated. For that reason, before performing the XRD analysis, the sintered sample has been pulverised and thoroughly homogenised with the 33 %wt. of Silicon. The element is added as an internal standard to calculate the amount of amorphous content. However, since it is not expected to be present in the real glass-ceramic composition, its contribution is subtracted by the overall contributions: hence, the remaining $2/3$ of the structure can be considered as formed by the crystalline frameworks (whose weight percentage was calculated by the software) and by the residual amorphous phase content.

Thus, with the XRD analysis the nature of the atomic structure has been investigated and the main composing crystalline phases identified.

2.3 FESEM and EDX analysis

The FESEM analysis (Field-Emission Scanning Electron Microscopy) on the sintered samples allows the reproduction of accurate microscopic scale images, revealing details on the glass-ceramic structure as the size, the shape and disposition of the molecular aggregates. It consists in striking high-energy electron beams against the samples under investigation, collecting the energy and orientation of the scattered elements with several detectors; the material response is reproduced as a 2D image with a software.

The machine used is the NVISION 40 type (Carl Zeiss Microscopy GmbH). The sintered samples have been prepared for the analysis by embedding them in epoxy through vacuum infiltration.

The high-energy beam is constituted by a flow of electrons generated from a negatively charged source and accelerated by voltage potential [16]. By passing in the vacuumed FESEM chamber, the beam is deflected through a series of apertures and lenses, which focus the ray on precise points of the target specimen. The lenses movement is governed by the electromagnetic field excitation created by application of electrical current.

Once penetrated the specimen, the incoming electrons are scattered, losing some energy, and the trajectory is altered with respect to the incident beam direction.

The most relevant scattered electrons for this investigation have been the “BackScattered Electrons” (BSE) and the “Secondary electrons” (SE). The formers derive from beam electrons experiencing elastic scattering and being deflected out of the specimen surface with still high energy; the images obtained analysing the intensity of the outgoing BSE reveal important aspects on the specimen composition, topography and crystallography. The SE are low-energy electrons expelled from the outer atomic shell following the collision with high-energy beams: together with the X-Rays (emitted after collision of high-energy beams with tightly bound inner shell electrons) they provide information concerning the phase composition of the studied material.

Each time an electron beam hits the target surface, the computer control memorizes the spatial coordinates in the specimen and the data from the detectors, measuring the effect of interaction between the high-energy beam and the target. Hence, the FESEM image is

obtained by reproducing these effects in a geometrical reconstruction with magnified dimensions.

The difference in grey shades (Fig. 2.6) depends on the atomic number of the scattered species: normally, the higher it is, the higher the number of atomic electrons, hence the greater and stronger the interaction with the incoming beam, leading to lighter imaged parts. Contrarily, atoms with small atomic number have less electrons and the intensity of scattered beam is reduced, leading to darker parts in the image.

In association to the FESEM, the EDX analysis (Energy-Dispersive X-Ray Spectroscopy) is useful to identify the elements of each structure.

The study is conducted by detecting the emitted X-Rays with the X-MAX 150 Silicon Drift Detector (OXFORD Instruments) embedded in the FESEM machine. Absorbing the incoming X-Rays, the device material emits some electrons from the outer atomic shell, which are internally scattered in the crystalline structure of the semiconductor. As a consequence, the valence shell electrons are promoted in the conductive band, leaving some positively charged particles behind. With the application of voltage to the ends of the detector, the electrons in conductive band are free to move and the charges are deposited in the anodic part.

The photonic energy received and the measured cumulated energy are the units employed for identification of characteristic elements in the sample: as shown in Fig. 2.6, the EDX spectrum, representative of a defined position in the specimen, is constituted horizontally by the collected energy (in keV), vertically by the number of photons whose energy is indicated in the horizontal axis.

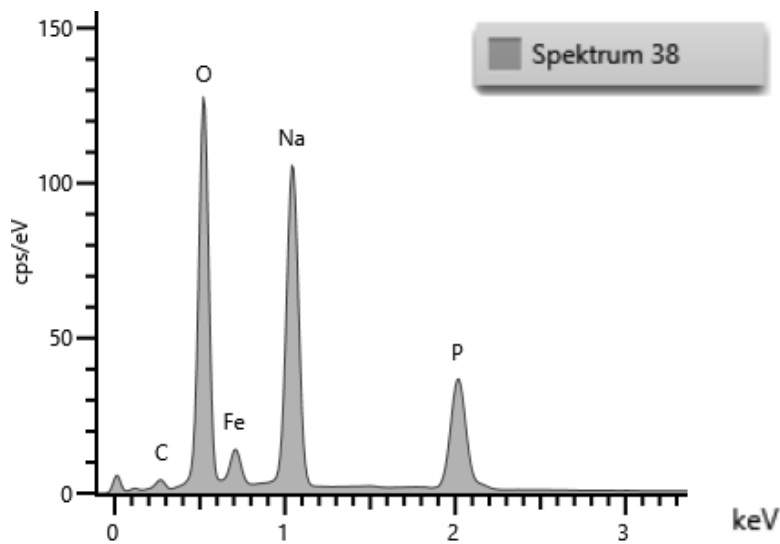
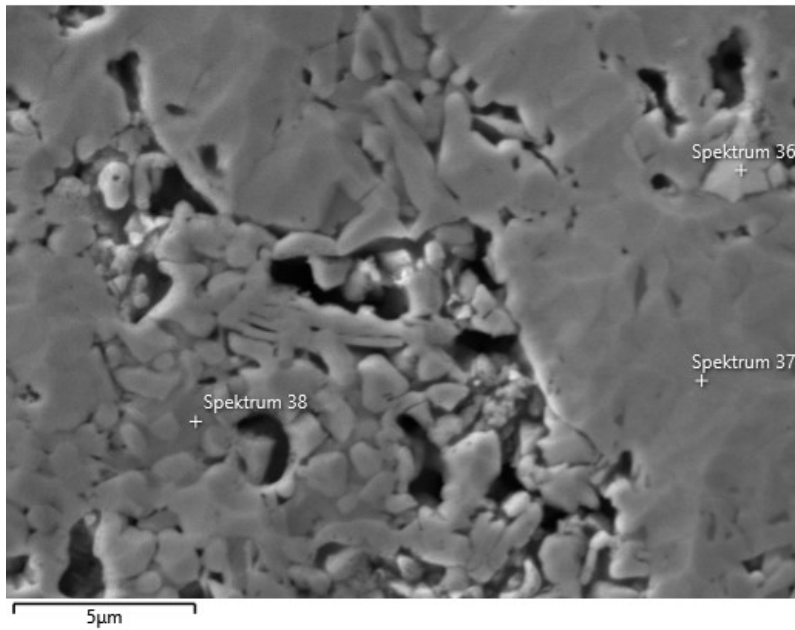


Figure 2.6 – EDX spectrum for a precise point detected in the crystalline structure displayed in FESEM image (Source: IKTS)

Thus, with FESEM and EDX analysis is possible to have an additional evidence of the expected densification behaviour, porosity and crystalline phase formation in studied samples.

2.4 Density measurement

In order to investigate the most suitable sintering procedure, the pulverised amorphous material has been pressed and coin-shaped.

The operation requires the employment of a testing machine (Inspekt 20-1 Table, Hegewald & Peschke) for pressing the powders by means of a cylindrical die. The pressing device is constituted by a fixed part, in which the die containing powders is located, and by a servo motor-driven traverse, which moves toward the sample exerting a pressure force for a fixed time.

Similarly to some Literature studies [3,17,18], it has been defined a sample diameter of 15 mm and a mass of 0.8 g, pressed with a force of 8.5 kN. Due to the scarce stiffness of the as-pressed sample, it has not been possible to directly measure the thickness, which has been instead calculated from the difference in the heights of cylindrical die with and without the amorphous powders.

The mass and geometry have been also determined after the sintering process.

The mass is measured with a laboratory scale (measurement error of ± 1 mg) and the sample geometry with a calliper (measurement error of ± 0.01 mm).

The following image (Fig. 2.7) shows a picture of powders pressed in form of tablets.

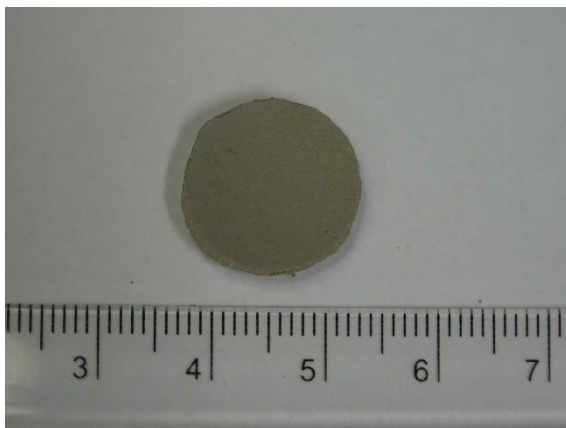


Figure 2.7 – Coin-shaped tablets from pressed sodium-iron-phosphate powders

The series of measurements performed is essential for the estimation of the material density, calculated as the ratio of the mass over the volume (g/cm^3): indeed, the material

densification is the first physical expected effect during the realization of the glass-ceramic component. Hence, the geometry and mass data collected before and after sintering are proof of the effectiveness, or not, of the sintering path in the creation of a sufficiently densified sample.

Due to the measurement errors of the measuring tools, the density value is always summed to its relative standard deviation.

Being the density a function of mass, diameter, and thickness (Eq. 2.2):

$$\rho = \rho(m, d, h) \quad (2.2)$$

the error is defined in Eq. 2.3:

$$\sigma_\rho = \sqrt{\left(\frac{\partial \rho(m, d, h)}{\partial m}\right)^2 \sigma_m^2 + \left(\frac{\partial \rho(m, d, h)}{\partial d}\right)^2 \sigma_d^2 + \left(\frac{\partial \rho(m, d, h)}{\partial h}\right)^2 \sigma_h^2} \quad (2.3)$$

where σ_m is the measurement error of the scale and σ_d, σ_h the measurement errors related to the calliper.

2.5 Measurement of electronic conductivity

The electronic conductivity, together with the ionic conductivity, is one of the basic requirements for a material employed as an electrode in a battery. It indicates the ability of a structure to move some electrons and provide electrical current (Eq. 2.4), and it is the inverse of the electronic resistivity (ρ_{el}), which on the contrary quantifies how the current flow is limited into the material:

$$\sigma_{el} = 1/\rho_{el} \quad (2.4)$$

The resistivity is an intrinsic property of the material, therefore not dependent on the size, shape and geometry; it is calculated with the following formula (Eq. 2.5):

$$\rho_{el} = R(A/l) \quad (2.5)$$

where R is the electrical resistance, A is the measured cross-sectional area of sample and l is the measured thickness.

The electronic conductivity estimation on some glass-ceramic material is made by measuring the electrical resistance at the ends of one sample, whose cross-sectional surface is covered with some conductive substance.

The procedure has been firstly made by gold sputtering (Fig. 2.8) the cross-sectional areas of sintered samples in a DC-sputtering machine (BAL-TEC SCD 050, ©Wiemer EM-Service oHG). Some protective Teflon layer was previously applied to avoid gold sputtering in the lateral surface of the samples.

Thereafter, the DC-resistance has been measured by connecting both sides of the sample to the test probes of a multi-meter (measurement error of $\pm 1 \text{ m}\Omega$).

Nonetheless, it is not rare to happen to repeat the procedure, due to excessive oscillation in measurement values, and to cover the cross-sectional area of tablets with another conductive element.

Hence, the sample surfaces have been coated with a silver conductive paste (CONRAD Electronic), in contact with some small platinum wires, submerged in the conductive paste and folded to increase to surface of contact (Fig. 2.9).

Again, the DC-resistance has been measured connecting the extremities of Pt wires with another testing multi-meter (measurement error of $\pm 0.01 \text{ m}\Omega$).

Knowing the geometry of each sample, finally the electronic conductivity has been calculated at ambient reference temperature T_{amb} .



Figure 2.8 – Picture of sintered gold sputtered samples: on the left, a scarcely densified sample, in which gold was partially internally absorbed; on the right, a sufficiently densified tablet



Figure 2.9 – Gold sputtered sample with silver conductive paste coating and Pt wires

2.6 Electrochemical Impedance Spectroscopy analysis

In an electrical system, the Electrochemical Impedance can be defined as the complex resistance experienced when the current flows through a circuit made of resistors, capacitors and inductors [19]. In fact, as a resistance, it indicates the ability of the circuit to circulate electrons and electrical current; at the same time, it is also comparable to a capacitor or an inductor, showing the ability of the electrical circuit to store the magnetic energy created by the application of an electric field.

The Electrochemical Impedance Spectroscopy is measured by applying a small signal AC voltage at various frequencies, detecting the current output through the sample: in this way, it is possible to identify the mainly circuit resistive elements, to detect the weak points of structure under investigation and to calculate the conductivity.

Being ω the radial frequency (Eq. 2.6)

$$\omega = 2\pi f \quad (2.6)$$

and φ the phase angle between the voltage signal $V(t)$ and the current signal $I(t)$, the complex impedance is defined in Eq. 2.7:

$$Z^* = \frac{V(t)}{I(t)} = \frac{V_a \sin(\omega t)}{I_a \sin(\omega t + \varphi)} = Z_a \frac{\sin(\omega t)}{\sin(\omega t + \varphi)} \quad (2.7)$$

Considering the Euler's relationship (Eq. 2.8)

$$e^{j\varphi} = \cos \varphi + j \sin \varphi \quad (2.8)$$

the complex impedance becomes (Eq. 2.9)

$$Z^* = Z_a e^{j\varphi} = Z_a \cos \varphi + j Z_a \sin \varphi \quad (2.9)$$

where the first term ($Z_a \cos \varphi$) is the “Real impedance part” and the second term ($j Z_a \sin \varphi$) is the “Imaginary impedance part”.

Hence, the complex impedance is always expressible in terms of magnitude Z_a , of module $|Z|$ and of phase angle φ .

In the work investigation, the solid electrolyte is coupled on one side with a coin-shaped metallic sodium layer, working as anode electrode, on the opposite side it is coated with a slurry of cathode active material. The Impedance Spectroscopy allows the detection of resistive and capacitive elements in the system, due to the different conduction processes occurring at electrolyte level and at its interface with the anodic and cathodic material. In particular, the interface level is the most critical to analyse, because characterised by charge carrier shift (transition between the ionic and electronic conduction) and the formation of a double-layer.

The charge carrier shift, also defined as charge transfer, takes place each time there is an electrode potential and an electrochemical reaction between electrodes: it is related to the transfer of electric charges between electrolyte and electrode, and dependent on the rate of electrons transfer to the electroactive species near the electrode surface. Since the charge transfer effect represents a limit to the current to flow throughout the interface layer, for the EIS analysis it is modelled as a resistance (charge transfer resistance R_{CT}).

The double-layer forms at the interface level because of presence of deposited species, non-participating to the electrochemical process. Of opposite charge with respect to the electrode charges, they stick on the electrode surface, contributing to the formation of a non-uniform distribution of charges and of an electrochemical potential drop.

The phenomenon, usually modelled as a capacitor because of the presence of separation of charges, is indicated here as a Constant Phase Element (*CPE*): referring to an element with frequency-independent phase angle φ , the *CPE* represents a double-layer capacitance in case of non-ideality of electrochemical effects.

To give a correct interpretation of data from the Electrochemical Impedance Spectroscopy, it is primarily necessary to associate the physical system under investigation to an equivalent electrical circuit. Generally, it consists of a combination of ideal resistors and capacitors, even if the real system is far to be ideal due to several physical aspects (as the surface roughness, the possible non-parallelism of stack layers, the uneven current and voltage distribution at the surface, and so on).

Considering the interface physical effect, the system commonly used is constituted by the charge transfer resistance R_{CT} disposed in parallel with the Constant Phase Element *CPE*. The current flowing through the system will always choose the path of least impedance:

hence, for high applied frequencies it will pass through the capacitor (here indicated with a CPE element), whose impedance is inversely proportional to the frequency and thus smaller than the impedance related to the resistive element; conversely, for low frequency, the current will preferably flow through the resistor and the impedance is completely resistive.

The electrical equivalent system is completed by usually connecting in series another parallel circuit, composed by the resistance and capacitance related to the ionic movement in the electrolyte. If the electrolyte is a polycrystalline solid material, an additional circuit in series (with resistor and capacitor) is necessary due to the presence of the grain boundaries (Fig. 2.10).

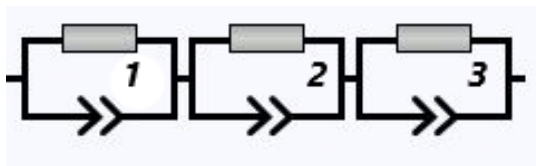


Figure 2.10 - Electrical equivalent system for EIS analysis: three R|CPE systems are disposed in series, respectively indicating the resistance and real-capacitance related to the bulk electrolyte (n.1), to the grain boundaries (n.2) and to the interface with the electrode material (n.3) (Source: IKTS)

The software for the impedance analysis RelaxIS (rhd instruments GmbH & Co.) associates the data collected from impedance measurements with the electrical equivalent circuit, creating best fit curves represented in Nyquist plots. The graph reproduces the calculated Imaginary and Real part of impedance as frequency varies, with growing frequency values the closer the points to the origin of axes.

The plot is composed by two curves (Fig. 2.11), associable to two depressed semicircles: at higher frequencies the AC voltage change of direction is fast and only fast-response-electrochemical processes are detected (typically the ones related to the electrolyte); on the contrary, at lower frequencies the change in voltage direction is slower and it is possible to characterise the response of slow electrochemical processes, as the ones occurring at the interface level.

Thus, each curve is associated to a proper time constant τ , depending on the resistance and capacitance effects of the electrolyte or the interface:

$$\tau = RC \quad (2.10)$$

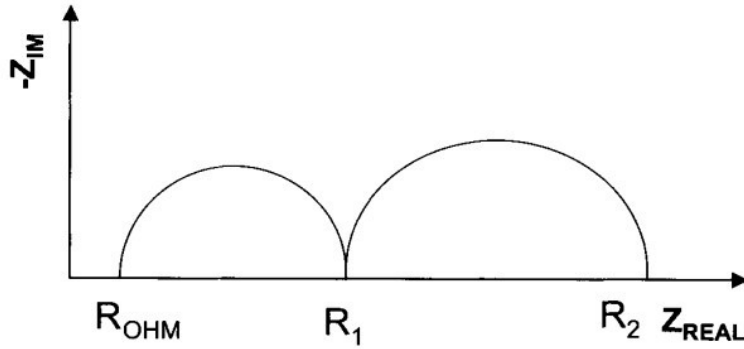


Figure 2.11 – Example of Nyquist plot with two depressed semicircles: on the left, the one detected at high frequency, related to electrolyte resistive and capacitive processes, on the right the curve at low frequency, characteristic of interface processes. The Ohmic resistor R_{OHM} is also added to the system
 (Source: Vadim F. Lvovich, IMPEDANCE SPECTROSCOPY – Applications to Electrochemical and Dielectric Phenomena, (2012) John Wiley & Sons, Inc.)

The resistance values are detectable from the intersection of the plot with the Real Impedance axis.

The conductivity value is calculated starting from the resistance and the geometric factor, given by the ratio between the area of the sample and the thickness (Eq. 2.11):

$$\sigma_{ionic} = \frac{1}{R(A/l)} \quad (2.11)$$

The measurements are usually performed for a broad range of temperatures, to have a wider overview of how the system resistivity and conductivity change in different working conditions.

2.7 Charge-discharge measurements of the cell

After the characterization of the cathode and electrolyte materials, the performance investigation in a “full cell” configuration is essential. The electrodes and electrolyte are stacked and positioned in specific testing devices: with accurate testing software, the electrical current passing through the stack is measured in response to the DC voltage applied during the loading phase, or released during the discharging phase. The amplitude of voltage signal is limited and defined according to previous studies [3,17,18]. The process is characterised by a certain speed, referred as “C-rate”, indicating the rate at which the system can be fully charged or discharged.

The charge-discharge cycles are repeated several times and the performance degradation is calculated in function of the charge or discharge capacity (Eq. 2.12):

$$C\text{-Efficiency (\%)} = \frac{Q_i - Q_{i-1}}{Q_{i-1}} \quad (2.12)$$

where Q_i is the charge or discharge capacity measured at a certain cycle, Q_{i-1} is the measurement at the previous cycle.

For the electrochemical performance investigation with a conventional liquid electrolyte, the sintered cathode material is pulverized, mixed with electrical conducting agent and reduced in form of slurry with the addition of a binder and a solvent material; after the drying in vacuum atmosphere, the batch is punched out in form of disks of defined geometry. It is employed as working electrode and coupled with a layer of metallic sodium as counter electrode in a Swagelok[®] cell (Fig. 2.12). The device connects the two electrodes with stainless steel plungers, working as current collectors, kept at a proper pressure with the auxilium of a compression spring. The ionic transport is ensured by the presence of a separator, commonly made of a glass-fiber filter, which is wetted by the liquid electrolyte and positioned between the working and the counter electrode. Once properly stacked and closed, the cell is connected in the ends with wires for the charge-discharge measurements.

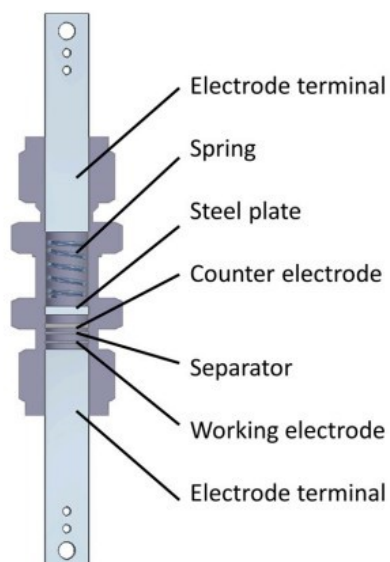


Figure 2.12 – Schematic design of Swagelok®-type electrochemical cell
 (Source: D. Klein, Y. Xu, R. Schögl, S. Cap, Low Reversible Capacity of Nitridated Titanium Electrical Terminals, *Batteries 5* (2019), 17)

For the battery performance with a solid-type electrolyte, the cathode material is again mixed with electrical conducting agent and reduced to a slurry with a binder and a solvent material; differently to the previous case, it is directly applied on the electrolyte surface and, after a drying period, the stack is co-sintered in oven. The coated-electrolyte is pressed in controlled atmosphere with coin-shaped metallic sodium, working as anode electrode, and disposed in EL-CELL® device (Fig. 2.13). Internally to a small metallic cylinder, the battery stack is surrounded by a PEEK sleeve, which ensures a good current distribution, and covered by a stainless steel plunger protecting from possible corrosion phenomena; a gold spring provides the necessary mechanical load, and the system is isolated and tightly closed with an external bracket. Again, the measurements are performed by connecting some electrical wires to the banana jacks in the front part of the apparatus.

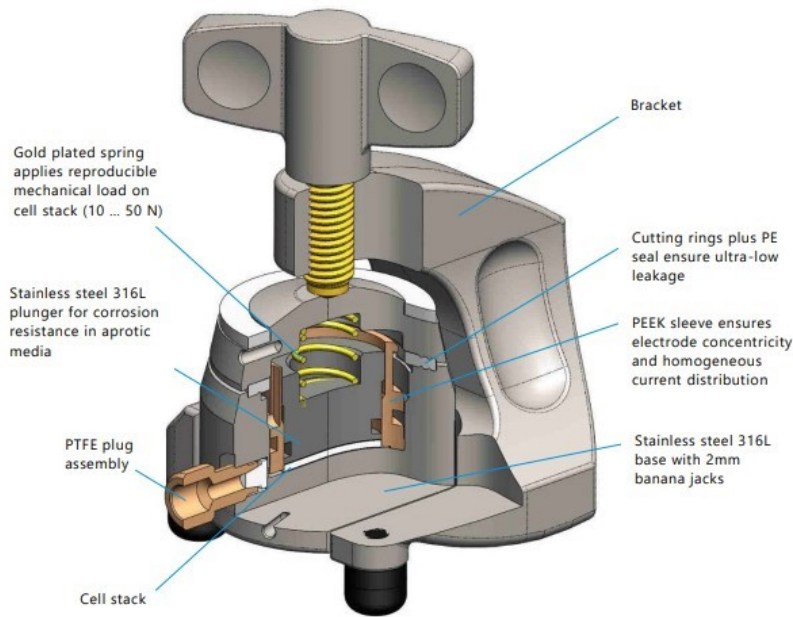


Figure 2.13 – Vertical cross section of *EL-cell* device
 (Source: *EL-CELL*[®] - electrochemical test equipment)

The data obtained with these measurements are crucial for the feasibility evaluation of the system under investigation, and for giving a critical estimation on the main characteristic aspects of the stack.

Chapter 3: Experimental Procedures

In order to produce the cathode material, the precursor elements NaPO_3 and Fe_2O_3 have been firstly thoroughly blended in a mechanical mixer for 30 minutes, next treated at high temperature by melt-quenching method. The melted batch has been produced both in oxidizing and reducing atmosphere. After drying, the glassy particles have been roughly crushed in a Vibratory Disc Mill for few minutes, and next additionally milled and reduced to a desired particle size in a Planetary Ball Mill for 12 hours. To examine the homogeneity and powders distribution in the compound, a Particle Size Distribution has been performed.

The obtained powders have been properly pressed and several sintering processes have been investigated, with the aim of identifying the conditions for the creation of a glass-ceramic material, whose composition is suitable for electronic and ionic conduction if employed as a cathode element in a battery.

To complete the analysis on sintering methods, the glass powders have been mixed with additional carbon source, as citric acid and graphite: the insertion of those elements is required to guarantee the electronic conductivity of the material, and is fundamental for the reduction process to occur during the oven treatment. The optimal sintering procedure has been obtained by studying the effects of variation of different parameters, such as the quantity of carbon source added, the sintering atmosphere, the temperature, and so on.

The Na07 and NaSICON type solid-state electrolytes have been investigated in association to a layer of metallic sodium, representing the anode component in the battery configuration. The resistance to the ionic conduction through the interface has been detected by Electrochemical Impedance Spectroscopy analysis on a stack composed by coin-shaped solid electrolyte, pressed on both sides with Na circular layers.

Afterwards, the mixture of pulverised glass material and conductive carbon source has been transferred into a slurry by adding a solvent and a polymeric binder: the compound has been stirred with Speed Mixing method, spread on the surface of the solid electrolyte

samples and dried overnight. The electrolyte tablets, coated with the cathode slurry, have been co-fired in oven according to the optimal sintering configuration.

Finally, the battery has been assembled stacking the solid electrolyte coated with cathodic material, and metallic sodium layer on the other side. The new configuration has been submitted to EIS analysis for the evaluation of the resistance to the ions movement through the interface between electrolyte and cathode, and to charge-discharge cycle measurements for analysing the electrochemical activity in the entire stack.

3.1 Synthesis of glass powders

The study of the most suitable cathode material has begun with the glass production by conventional melt-quenching method, as reported in Literature [3,17]. The starting compounds have been homogeneously dry stirred in a blender machine, which allows the accurate mixing of substances of different specific weights and particle size. The batch has been melted at high temperature in different atmosphere conditions, to experiment how the melting atmosphere influences the material properties during glass-ceramic production via sintering. After drying, the glass pieces have been grinded in crushing machines to be homogenized and reach a uniform particle distribution.

3.1.1 Working principle of TURBULA[®] machine

The TURBULA[®] machine (WAB, WILLY A. BACHOFEN AG) is a 3D shaker mixer, employed in several industrial fields for mix and homogenization of different substances. It is constituted by an electrical motor-driven articulated bracket, activated by eccentric drive gear mechanism. The bracket is connected to an empty cage, inside which there is space for the location of container with the substances to be blended. The canister, which could be of different dimensions, is fixed in the cage by lateral rubber straps and a tension collar on the top. The batch is rhythmically moved due to the harmonic interaction of translation, rotation, and inversion, as showed in Fig. 3.1 hereunder.

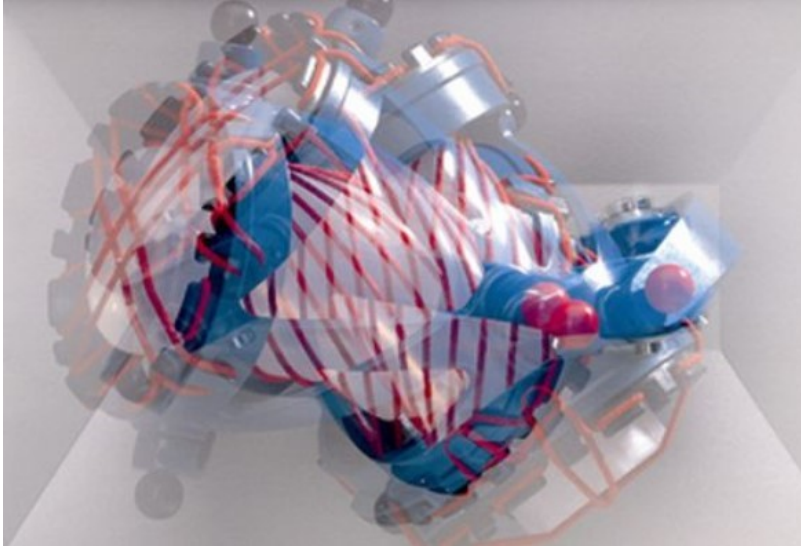


Figure 3.1 – Scheme of movement of blender machine in different directions
(Source: WAB, WILLY A. BACHOFEN AG, 3D shaker mixer)

The desired quantities of starting compounds for glass production have been weighted with a scale, and mixed in a canister inside the mechanical blender at constant speed for 30 minutes.

3.1.2 Glass synthesis in oxidizing atmosphere

The glass material precursors have been chosen following the previous studies [3,17]. For the calculation of the effective quantities of Fe_2O_3 and NaPO_3 to be mixed, it has been supposed to create a 200 g batch composed by FeO (molar mass 71.84 g/mol) and NaPO_3 (molar mass 101.92 g/mol). The molar fractions of 33.3 mol% of FeO and 66.7 mol% of NaPO_3 were stated according to the desired chemical reaction.

The mass fraction (ω_i) has been calculated with the following equation (Eq. 3.1):

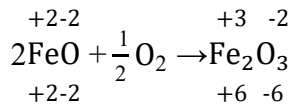
$$\omega_i(\%wt.) = \frac{x_i M_i}{\sum_j x_j M_j} \quad (3.1)$$

where x_i and M_i are respectively the molar fraction and the molar mass of the i component, $\sum_j x_j M_j$ is the average molar mass of the mixture.

Finally, the mass of FeO and NaPO₃ has been calculated considering the mass fraction ω_i (Eq. 3.1) and the total desired mass m_{tot} , in Eq. 3.2:

$$m_i (g) = \frac{\omega_i \cdot m_{tot}}{100} \quad (3.2)$$

In air, the iron oxide FeO easily transforms into Fe₂O₃ because of oxidation process: therefore, Fe₂O₃ has been the raw material used in mixing and melting with the sodium phosphate NaPO₃. Considering the oxidation reaction



the Multiplication Factor has been defined as the ratio between the obtained quantity of Fe₂O₃ in oxidizing conditions and the starting quantity of FeO (Eq. 3.3):

$$\text{Multiplication Factor} = \frac{M_{\text{Fe}_2\text{O}_3} \cdot \text{mol}_{\text{Fe}_2\text{O}_3}}{M_{\text{FeO}} \cdot \text{mol}_{\text{FeO}}} \quad (3.3)$$

where $M_{\text{Fe}_2\text{O}_3}$, M_{FeO} are the molar masses of Fe₂O₃ and FeO, $\text{mol}_{\text{Fe}_2\text{O}_3}$ is the final number of moles obtained from the oxidation reaction, mol_{FeO} is the starting number of moles employed in the reaction.

The Multiplication factor for the sodium phosphate is equal to 1, since the composition does not change.

Lastly, the mass of the glass precursors has been obtained with Eq. 3.4:

$$m_i (g) = \frac{\text{Multiplication Factor} \cdot m_{i,old}}{\text{Comp}} \quad (3.4)$$

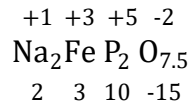
with $m_{i,old}$ as the mass previously calculated (Eq. 3.2), and Comp as the number of precursor elements (in this case 2).

Once properly blended, the batch composed by Fe₂O₃ (Dainichiseika Color & Chemicals MFG.Co) and NaPO₃ (VWR Chemicals BDH[®]) has been poured into a Platinum crucible for the melting phase. The crucible was placed inside a High-Frequency coil, in a furnace chamber exposed to air: when the AC current flows through the wire, the magnetic field and the induced eddy currents cause the heating of the batch by Joule effect.

The powders were melted for 1 hour, during which the iron oxide Fe₂O₃ and sodium phosphate NaPO₃ combined according to the following chemical reaction:



It can be easily proved that the resulting glass composition is constituted by iron elements with oxidation number equal to 3:



It is assumed that the sintering process in reducing atmosphere would lead to the reduction of Fe³⁺ to Fe²⁺, hence to a glass-ceramic material as Na₂FeP₂O₇, having better performances in terms of electric and ionic conductivity with respect to the oxidised structure.

After the melting completion, the glass material has been poured on a plate and rapidly dried using a CuZn-alloy die.

3.1.3 Glass synthesis in reducing atmosphere

Some other glass material has been created with the same melt-quenching procedure, but in a controlled reducing atmosphere. In fact, since it is stated that reducing conditions are favourable for the iron reduction and the possible achievement of an active cathode material, it has been decided to investigate the sinterability of a structure whose starting glass composition was produced in non-oxidizing conditions.

The batch was composed by the starting elements Fe₂O₃ and NaPO₃ in the same molar fraction as the melting in air conditions, and the heating has been carried out with the so-called “Pot-In-Pot” technique: the mixed powders were placed in a small Alumina crucible, leant on a graphite block inside a bigger Alumina pot. The whole was closed by a refractory top in the upper part, to guarantee insulation to the external atmosphere, and was internally purged with nitrogen. The presence of graphite, not in direct contact with

the sodium-iron-phosphate to avoid any undesired reaction as fumigation or combustion of the carbon source, provided the reducing environment inside the crucible.

This set-up has been heated in electrical furnace for 3 hours, next dried similarly to the procedure in air.

3.1.4 Working principle of Vibratory Disc Mill and Planetary Ball Mill

After the melting phase, the glass powders have been submitted to a process of size reduction, which is required whenever a product is constituted by coarse and non-homogeneous particles. Several experimental analyses (as the HSM) necessitate a small quantity (few milligrams) of the produced substance: hence, the sample should be representative for the properties of the whole material, and this aspect is achievable with homogeneous distribution and sufficiently small particle dimension. Moreover, a wide particle surface increases the contact points among particles and promotes the crystallization during the sintering procedure.

Firstly, the batch has been grinded in a Vibratory Disc Mill, which reduces the powder dimensions to a size range of 50-60 μm . The powders have been comminuted in a cylindrical metal jar, subject to circular horizontal vibrations produced by an electrical motor. Internally, a disc and some grinding rings are moved by the centrifugal force created and exert high pressure and friction by striking against the metallic jar and the glass material in the middle. The procedure is adjustable in speed and brings to high fineness in a short period of time.

First, the powders have been crushed at 700 rpm for 30 s, next they have been refined by setting a higher rotational speed (1400 rpm) for a time of 80 s.

A cross section of the metal jar employed is shown in Fig. 3.2 hereunder.

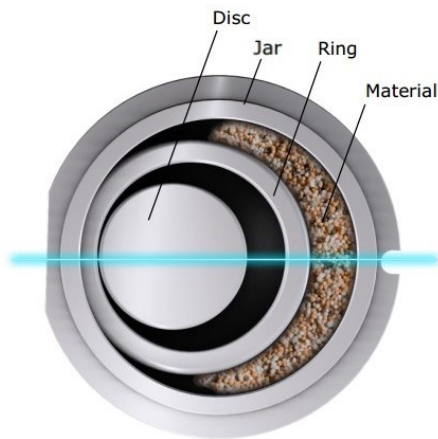


Figure 3.2 – Horizontal cross section of the cylindrical metal jar in Vibratory Disc Mill machine (Source: Retsch® GmbH)

Afterwards, the milling procedure has been extended and refined using a Planetary Ball Mill (PULVERISETTE, FRITSCH GmbH). The device is formed by four grinding jars, arranged eccentrically on a “sun wheel”: while the latter rotates in one direction, each cylindrical jar moves on its axis in the opposite direction, originating high dynamic energies. The powders are poured into the grinding jar with some quartz balls, subject to Coriolis forces during rotation and impacting against the particles. Some water was also added, to improve the process efficiency and limit the production of dust.

The glass powders have been milled for 12 hours at a rotational speed of 200 rpm.

The following scheme (Fig. 3.3) presents a Planetary Ball Mill constituted by two cylindrical jars.

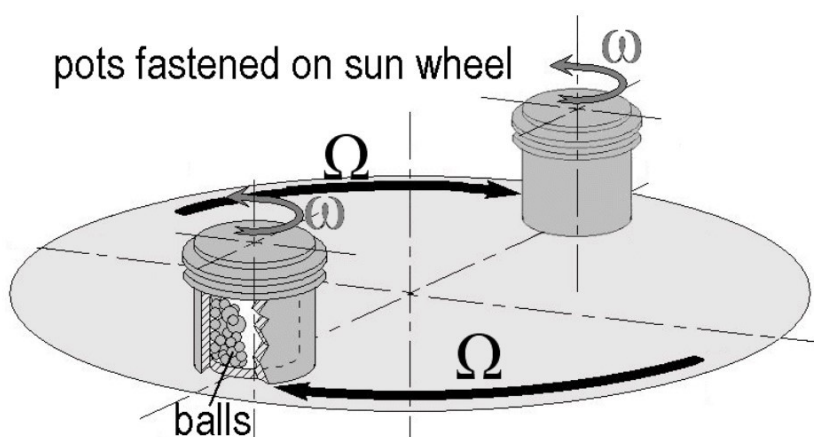


Figure 3.3 – Schematic working principle of a Planetary Ball Mill with two cylindrical jars: the sun wheel rotates in Ω direction, the jars in opposite ω direction (Source: E. Roblot, P. Grosseau, B. Guilhot, B. Classen, C. Haehnel, E. Gaffet, A study on the action mechanisms of grinding aids used for clinker comminution, Conference Paper (2005))

Finally, a Particle Size Distribution study has been made (software MASTERSIZER 2000, Malvern Instruments) to investigate the inner dimensions and particles homogeneity of the resulting batch, and to prove the effectiveness of the milling processes.

3.2 Sintering procedure

The sintering process consists in heating the raw amorphous powders in a furnace, with the aim of promoting the densification and formation of a solid body. With the increase of temperature over the glass transition temperature T_g , the material starts to flow viscously, the atomic kinetic energy is enhanced and the bonding of particles is induced. The starting particle size distribution is important: sintering and densification are fostered with smaller particles, having higher surface energy to be given up in the formation of bonds. The heating rate is an influencing parameter as well: the higher it is, the less is the available time for atoms to move and to aggregate.

If the applied temperature is high enough and the material lasts in those conditions for a sufficiently long period of time (defined “dwelling time”), the nucleation and growth of crystals are promoted, allowing the creation of a more ordered arrangement suitable for ionic conduction; with increase of crystallization, the densification is limited.

The sintering atmosphere is imposed according to the crystalline structure desired: a process performed in air atmosphere leads to oxidizing effects, consequently to a glass-ceramic material whose crystalline phases are likely to be different with respect to the same process implemented in reducing conditions.

Thus, the sintering procedure is considered as a sequence of variations in the temperature steps over the time (Fig. 3.4). From room temperature, the furnace is heated with a certain speed, according to a heating rate user-defined; once reached the desired point, the temperature is kept as constant for a specific period of time and finally, it is decreased again at T_{room} with a precise cooling rate.

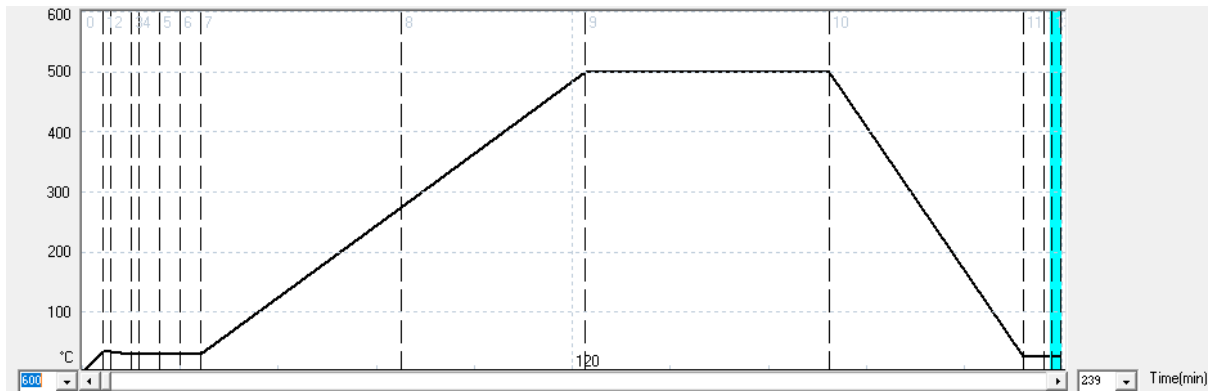


Figure 3.4 – Example of sintering profile set in oven, representing the temperature variation during time; the graph is divided in several steps, for each of which the atmosphere, heating rate and holding time are defined (Source: IKTS)

In the study performed, the sintering profile has been varied according to the maximum heating temperature, the soaking time, the heating rate and the oven atmosphere, basing on the window of temperatures detected by HSM and TGA-DTA analysis, and on the Literature references [3,5,17,18].

Laying on sodium-iron-phosphate powders over Al_2O_3 tile, the pressed tablets have been sintered in air atmosphere, with heating rate of 5 K/min up to $T_{\text{sintering}}$ of 550 °C and with soaking time of 15 minutes. Next, the temperature has been decreased again to T_{room} with a cooling rate of 10 K/min. The results have been compared with a sintering experiment made in same conditions, but at minor temperature of 500 °C. The oven employed is of type CARBOLITE® GERO.

The investigation proceeded with the sintering in reducing atmosphere (furnace ATV1, ATV Technologie GmbH), with heating rate of 5 K/min up to 550 °C, holding time of 15 minutes and cooling rate of 10 K/min. The reducing conditions have been achieved by employing “Varigon” gas (composed by hydrogen in a quantity range of 3-5 vol.%, and argon). To limit the risk of chemical reactions between the elements of glass material and the Alumina, the tablets were located on BN substrates, laying on the Al_2O_3 tile. Next, the behaviour in Varigon conditions has been studied varying the $T_{\text{sintering}}$ (reduced to 500 °C and 520 °C) and increasing the soaking time to 60 minutes: the goal was to identify the proper sintering temperature and examine, in the formed crystalline phases, the effects of the increase of dwelling time.

Thereafter, the $\text{Na}_2\text{FeP}_2\text{O}_7$ material melted in air (from here on, it will be indicated as “NFP”) has been submitted to a different sintering profile, according to previous studies [18]: the samples have been heated in Varigon conditions with 5 K/min rate to 560 °C, kept at the maximum temperature for 180 minutes and next cooled down to room temperature with rate of 10 K/min.

Finally, the same procedure has been carried out for NFP samples mixed with carbon agents $\text{C}_6\text{H}_8\text{O}_7$ (citric acid) and graphite, with the purpose of investigating the consequences, in crystallized structure, of sintering in reducing conditions with the addition of a reducing material in the batch.

Concerning the sodium-iron-phosphate deriving from the melting in reducing atmosphere (labelled as “NFPr”), the sintering behaviour was not analysed, because the material demonstrated poor densification either in air and in Varigon conditions, hence it was considered not suitable to be employed as a cathode electrode realised via glass-ceramic production.

3.3 Addition of carbon as conducting agent

As anticipated, the NFP powders have been mixed with citric acid and with graphite: the objective has been the analysis of reducing effects on the sintered material and the investigation of the electronic conductivity properties.

The citric acid $C_6H_8O_7$ ($\geq 99.5\%$, anhydrous, Carl Roth GmbH + Co.KG) is a colourless and odourless organic acid substance, often employed as reducing agent in sintering processes [3,18]. During the heating phase, the citric acid in contact with the glassy particles is subject to thermal decomposition, resulting in the possible formation of water vapour, carbon dioxide CO_2 , carbon monoxide CO and solid carbon, hence acting as reducing agent on the NFP material. The reductant action is expected to increase if the sintering occurs in a controlled reducing atmosphere, promoting the $Fe^{3+} \rightarrow Fe^{2+}$ reaction and the formation of a structure with better electrochemical properties.

The experiment has been conducted by mixing the NFP glass powders with the 10 wt.% of citric acid in the TURBULA[®] machine for 30 minutes [18]. The Hot Stage Microscopy analysis has been performed in Varigon to investigate the behaviour of material during heating and to verify the densification. Finally, after pressing some tablets, sintering process has been carried out: the heating profile was the same used for sintering of NFP glass, that is heating rate of 5 K/min up to 560 °C, with holding time of 180 minutes, in Varigon conditions.

With the combination of the reducing action of carbon source and Varigon atmosphere, it was expected to achieve a sintered structure whose crystalline phases are characterised by a higher percentage of reduced iron elements. Moreover, being the amorphous carbon a good electronic conductor, its addition to the NFP was fundamental for the realization of a suitable cathode material.

The same sintering experiment has been investigated by adding some graphite (Timcal Timrex[®] KS15 AD-172M) to the NFP. Because of the carbon reducing action on the iron elements of the glass material, it is predicted the release of gaseous products as CO_2 , CO and vaporised H_2O , similarly to the case of citric acid addition. Due to its laminar structure, the mixed graphite percolates in the glass matrix and surrounds partially the

glassy particles, ensuring a good conduction path for the electrons to move. Hence, a high graphite content guarantees good electrical conductivity, but simultaneously limits the densification of glass matrix during sintering and reduces the mechanical properties [20].

The NFP has been mixed with graphite in different quantities (3, 4, 5 wt.%), with the intention of verifying what is the best composition in terms of densification and crystallization of glass material, and electronic conductivity. The mixing occurred in the TURBULA[®] blender machine for 120 minutes. After the HSM analysis in Varigon with 5 K/min as heating rate, the different batches of powders have been pressed to obtain some tablets and submitted to sintering procedure (5 K/min to 560 °C, with holding time of 180 minutes and Varigon sintering atmosphere).

Lastly, the suitable composition has been chosen by studying the crystallised phases in the sintered tablets, the linear shrinkage detected with HSM analysis, and the measurements on electronic conductivity.

3.4 Interface resistance to metallic sodium electrode

Before the assembly of the battery, it has been fundamental to examine the coupling between the solid electrolyte and the anode material. Some Electrochemical Impedance Spectroscopy Analysis has been performed on the Na07 and NaSICON-type solid electrolytes stacked with metallic sodium, to investigate the resistance to the ionic movement through the interface. The results have been compared with outcomes from previous studies.

The Na07 samples were already sintered in IKTS and provided in form of small coin-shaped tablets, of 15.4 mm as average diameter. The thickness has been reduced by mechanical grinding to 1.4 mm.

The NaSICON tablets have been realised starting from powders (prepared in IKTS) pressed with a force of 7.5 kN to coin samples of 20 mm of diameter and 1 g of target mass. The pressed disks have been positioned on Al₂O₃ tile and covered on both sides by a protective polymer tape (made of NaSICON material) which during heating sticks to the samples and avoids any possible evaporation or reaction deriving from the contact with the substrate. The sintering occurred in air atmosphere, following the heating procedure from Literature [21]: phase of de-hydration heating at 0.5 K/min to 550 °C with holding time of 2 hours; phase of calcination with heating rate 0.5 K/min to 700 °C for 5 hours; finally, sintering phase with heating rate 3 K/min to 1230 °C held for 10 hours, and cooling to T_{room} with cooling rate of 3 K/min.

As the Na07 tablets, NaSICON sintered samples (average diameter of 16 mm) have been mechanically grinded to a uniform thickness of 1.25 mm.

Some coin-shaped disks of Na (12 mm of diameter) were stamped from a sodium stripe in protected environment (glovebox). The sodium anode has been stacked on both sides of the solid electrolyte disks and covered symmetrically by a layer of graphite (SIGRAFLEX®, SGL Carbon GmbH) to increase the electronic contact during measurements. The stack (Fig. 3.5) has been realised by applying a force of 1.5 kN with hydraulic press, with T_{pressing} equal to the room temperature.



Figure 3.5 – Picture of stacked sample in glovebox: the solid electrolyte (in the middle of the stack) has been coupled with metallic sodium and covered by graphite layers (in black)

The experiments have been repeated heating the pressing plates to 50 °C: the increase of pressing temperature is expected to enhance the surface contact between sodium metal and solid electrolyte, reducing the interface resistance.

Positioned in E1-cells, the stacked samples have been electrically connected in a Biologic Chamber (CTS Clima Temperatur Systeme GmbH) with imposed voltage amplitude of 25 mV, within a voltage range of -10 - 10 V.

The EIS investigation has been achieved varying the frequency from 100 mHz to 1 MHz and testing for different chamber temperatures, in the range -20 °C - 50 °C: at low temperatures in fact, the resistance and capacitance are higher, the EIS spectrum is well defined and this aspect facilitates the physical modelling of the stack.

3.5 Preparation of cathode slurry and sintering on solid electrolyte

The more suitable cathode material has been chosen according to the best results in terms of densification during sintering, crystalline phases with high Fe^{2+} content and electronic conductivity. Following the same procedure of Yamauchi et al. [5], the powders have been reduced to a slurry, applied over the solid electrolyte and co-fired according to the desired sintering conditions. The composition was the following: 50 wt.% of cathode active material, 5 wt.% of polymeric binder (PPC) and 45 wt.% of liquid solvent (MEK). The solvent and binder have been homogeneously mixed in a magnetic stirrer. Next, the mixture has been blended with the cathode material powders in a speed mixer: the procedure lasted 3 minutes, with repeated speed variation between 2000 and 3000 rpm to guarantee the thorough mixing procedure.

Then, the slurry has been applied over the Na07 and NaSICON solid electrolytes with a spatula (Fig. 3.6) and dried in essiccator overnight.

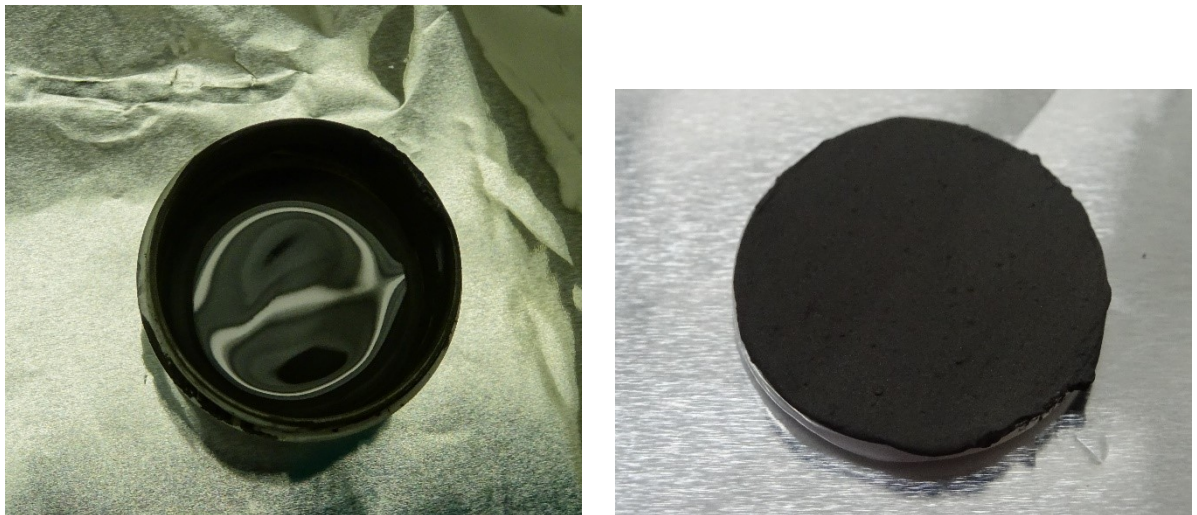


Figure 3.6 – Picture of produced slurry by speed mixing (left) and applied on the surface of solid electrolyte material (right)

Finally, the coated electrolytes have been sintered in Varigon conditions: firstly, the samples have been heated to 300 °C with heating rate of 2 K/min and holding time of 1 hour, to let the binder evaporate; afterwards, they have been treated with the already

investigated sintering procedure (heating rate of 5 K/min up to 560 °C, with soaking time of 3 hours).

The picture hereunder (Fig. 3.7) shows an example of solid electrolyte, after co-firing with cathode active material.



Figure 3.7 – Picture of Na07 solid electrolyte, sintered with slurry of cathode material

3.6 Battery cell assembly

The sintered solid electrolytes, co-fired with the cathode active material, have been gold sputtered over the densified slurry to increase the electronic contact. Afterwards, the battery has been assembled in protected atmosphere (glovebox) by stacking with the anode, constituted by metallic sodium.

Again, the stack has been obtained by mechanical pressing with a force of 1.5 kN, with press at room temperature and at 50 °C (Fig. 3.8). A plastic spacer was employed to avoid the direct pressure application on the cathode material. Some coin-shaped graphite foils were also pressed on both sides of the stack, to ensure a better electrical contact internally to the EI-cell.

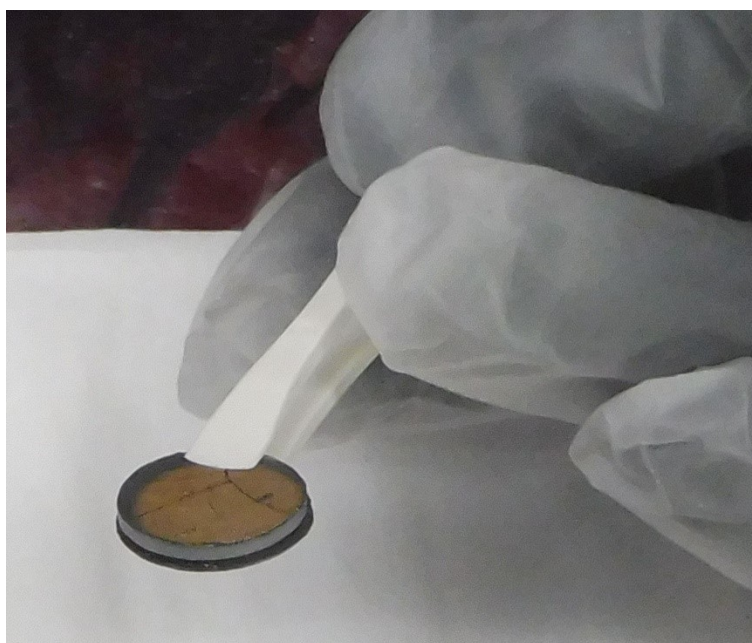


Figure 3.8 – Picture of battery stack pressed in protected atmosphere. From the bottom, it is composed by a layer of graphite, the sodium anode, the solid electrolyte, the gold sputtered cathode in form of slurry, and another graphite layer (here not depicted)

Once settled in the EI-cells, the battery has been characterised simultaneously with Impedance analysis and charge-discharge measurements in the Biologic Chamber.

For the electrochemical activity evaluation, the voltage has been set to vary in the range 2-3.8 V and the theoretical capacity has been defined as 97 mAh/g, according to the Literature studies [3,17]. The charge-discharge measurement has been carried out at 30

°C, with C/50 as C-rate. Thus, the frequency range of investigation for the EIS analysis has been limited to a minimum frequency of 50 Hz, starting from a maximum of 1 MHz. The impedance has been detected by applying a voltage amplitude of 25 mV, oscillating in the range -10 - 10 V. The measuring temperature was limited to the one of the charge-discharge measurements: hence, the Impedance spectra were calculated only for a chamber temperature of 30 °C.

In conclusion, the EIS results have been compared with the investigation performed in symmetrical configuration (stacking the solid electrolyte with metallic Na on both sides), to characterise the impedance at the interface with the cathode active material.

The charge-discharge measurements have been correlated with the analysis with liquid electrolyte and with the investigations from Literature: the comparison and the final outcome are fundamental to prove the electrochemical activity of the created stack and to detect imperfections and deficiency points to work on in future investigations.

Chapter 4: Results and Discussion

The techniques and methodologies described have been employed for the investigation on a suitable sintering procedure in the realization of a glass-ceramic cathode material, and for the successive coupling with two solid electrolytes. Basing on previous scientific publications, the main goal has been the creation of an active cathode material starting from a batch of glass powders, crystallized via sintering process. In particular, it is desired to demonstrate the possibility to produce a sintered material mainly composed by triclinic crystalline structure as $\text{Na}_2\text{FeP}_2\text{O}_7$, which has the ideal framework for Na^+ migration during battery operation.

According to Literature, it is expected to satisfy the requirements with the employment of a reducing sintering atmosphere, controlling the heating rate, the sintering temperature (generally, in the range 500-600 °C) and enhancing the soaking period, so that inner particles have more time for re-arranging in ordered configuration. The reducing action is promoted by mixing NFP powders with a carbon reducing agent, which enhances the electronic conductivity as well.

A good sintering operation is recognizable with the acquirement of highly dense tablets, with scarce porosity and defined by high percentage of crystalline content. The effectiveness of procedure in the creation of active material is verifiable by calculation of electronic conductivity and of the iron content: the framework in fact, is supposed to be ionic conductive if mainly formed by crystalline structures with reduced iron Fe^{2+} , promoting the generation of the 3D arrangement for Na^+ movement.

Once identified the proper sintering parameters, the operation is intended to be directly carried out on the solid electrolyte samples, coated with a slurry made of the desired cathode glass powders. The sintering process is predicted to be suitable for the realization, without any additional forces, of a strong and conductive interface connection between the two materials. Finally, it is expected to perform some charge-discharge measurement on the co-fired material, coupled on the other side with sodium anode, to examine the effectiveness of the created stack in terms of electrochemical performances.

4.1 Sintering behaviour in air

The sodium-iron-phosphate powders have been first of all characterised by heating in oxidizing atmosphere: as reported in previous studies [18], the sintered structure is expected not to be suitable for the realization of a cathode electrode, because characterised by crystalline phases with Fe^{3+} (non-reduced iron form), which does not guarantee the proper efficiency for Na^+ migration during phases of charge and discharge.

Uniformity and homogeneously distributed small particles are fundamental requirements for an efficient sintering and crystallization process [22]. The particle size distribution of NFP powders (obtained via melt-quenching production in air) is provided in Fig. 4.1. Starting from minimum dimension of $0.2 \mu\text{m}$, the graph indicates that the 10 % of volume of material is occupied by particles with particle size smaller than $0.7 \mu\text{m}$, arriving to the 90 % of volume with maximum particle size of $26.6 \mu\text{m}$: the results prove that NFP is characterised by sufficiently small particles with uniform size distribution.

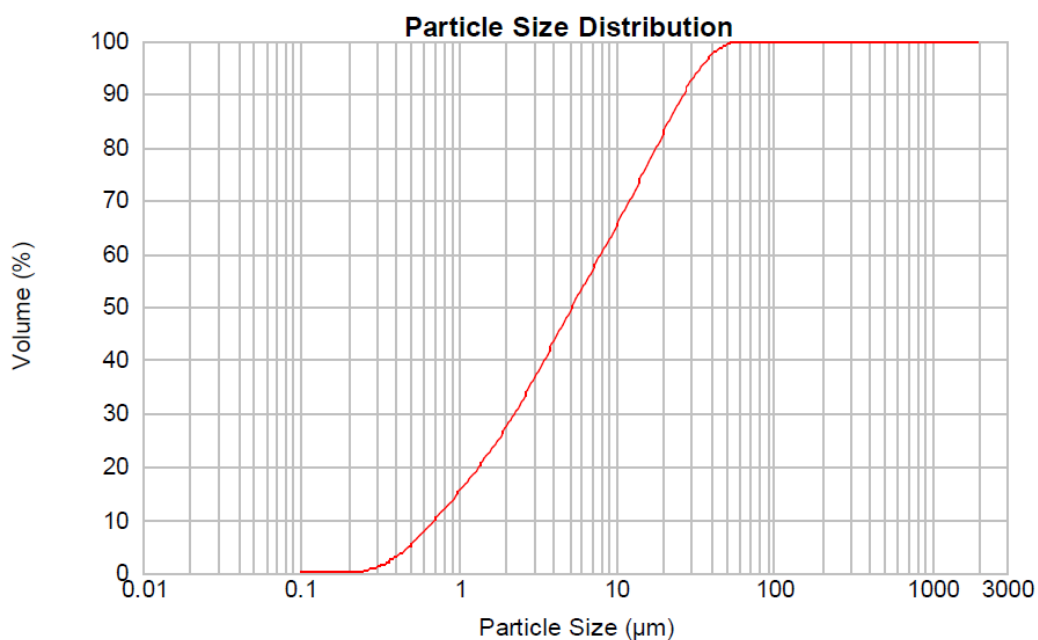


Figure 4.1 – Particle Size Distribution of NFP powders (Source: IKTS)

4.1.1 HSM and TGA-DTA procedures in air

The Hot Stage Microscopy analysis, combined with TGA-DTA, is depicted in Fig. 4.2. As visible, the mass variation is quite irrelevant (less than 0.2 % of mass loss), demonstrating the structure stability and the absence of decomposition, both at room temperature and during the heating treatment.

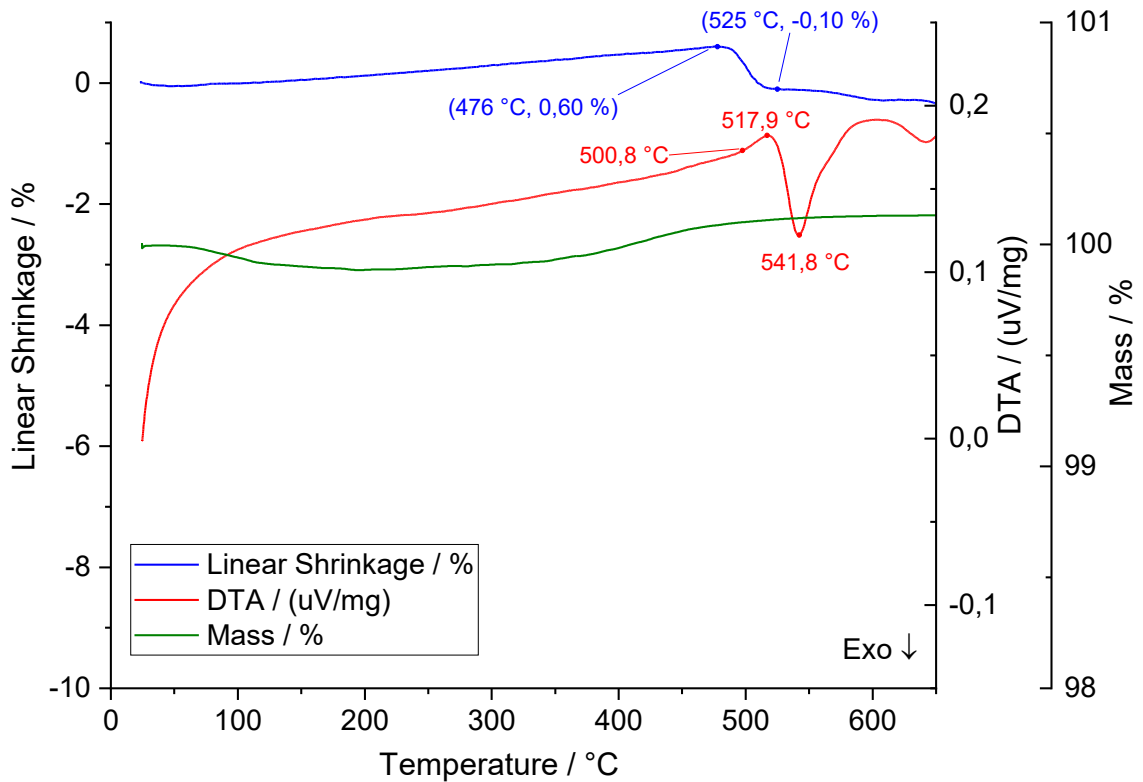


Figure 4.2 – HSM curve (blue), compared with TGA-DTA curves (red and green) for NFP material heated in air atmosphere at 5 K/min, up to 700 °C (Source: IKTS)

The curve deriving from Differential Thermal Analysis shows the expected trend for a sintering procedure. Indeed, it firstly grows in the endothermic direction, owing to the sample heat absorption with respect to the reference specimen; from the onset temperature at 500 °C (associable to the glass transition temperature T_g), the slope rises and the endothermic peak is reached at 517.9 °C, temperature closed to the maximum densification point. Keeping heating, the curve moves in exothermic direction, showing the probable structure aggregation in crystals and the point of maximum crystallization at 541.8 °C. For higher temperatures, the structure will be subject to melting phase.

Therefore, the window of temperatures for the sintering procedure is identifiable in the range 500-550 °C.

Nonetheless, the curve obtained from the HSM reveals scarce densification while heating: the insufficient volume reduction (less than 1 %) is expected to be the limiting factor to the creation of a stable composite in junction with the solid electrolyte.

The shrinkage behaviour has been tested for the NFPr powders (obtained by melting in reducing conditions with “Pot-In-Pot” technique) and associated to the results on NFP: since the volume reductions are small and comparable, the densification is likely to be hindered in oxidizing atmosphere, no matter the type of tested starting glass. The curves are reported hereunder in Fig. 4.3.

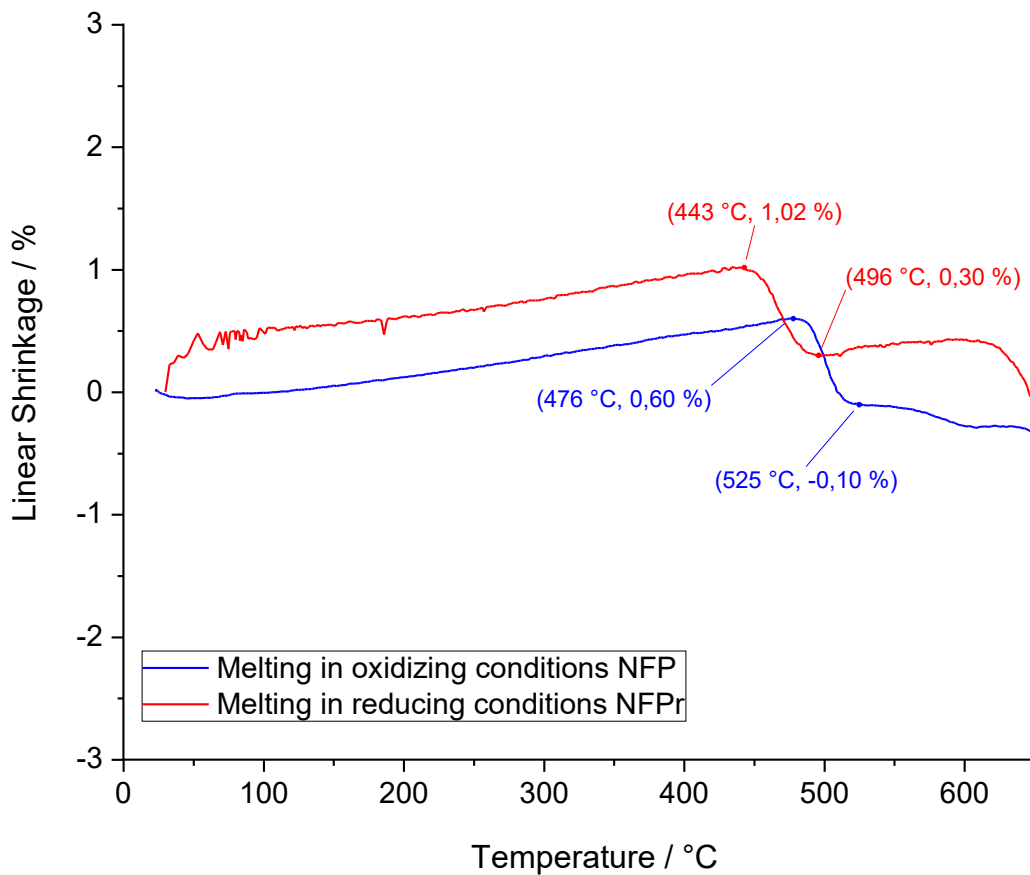


Figure 4.3 – Comparison of linear shrinkage curves for NFP (blue) and NFPr (red), heated in air atmosphere at 5 K/min, up to 700 °C (Source: IKTS)

4.1.2 Sintering and phase formation in air

The HSM analysis on NFPr demonstrated its non-suitability for the application as active cathode electrode, due to its scarce linear shrinkage while heating; thus, the sintering investigation has been performed only for NFP glass material. The suitable heating conditions have been derived from the HSM and TGA-DTA curves analysed in previous chapter: with same heating rate (5 K/min) and holding time of 15 minutes, sintering was performed at 550 °C (supposed to be the temperature at which the complete crystallization occurred) and 500 °C (possible glass transition temperature).

The density of sintered samples has been calculated and compared with density of the pressed glass powder: the values, with the relative standard deviation, are reported in the following Table 4.1.

Experiment	Density Before Sintering ρ [g/cm ³]	Density After Sintering ρ [g/cm ³]
$T_{\text{sintering}} = 550$ °C	1.89 ± 0.01	1.90 ± 0.01
$T_{\text{sintering}} = 500$ °C	1.85 ± 0.01	1.91 ± 0.01

Table 4.1 – Calculated density values, before and after sintering procedure, for samples treated in air at different sintering temperatures (Source: IKTS)

As predicted from the HSM curve, the samples sintered in air conditions undergo a scarce densification, probably caused by the occurring of crystallization.

The image in Fig. 4.4 shows the generated diffracted path and the responsible crystalline phases obtained from XRD investigation after sintering.

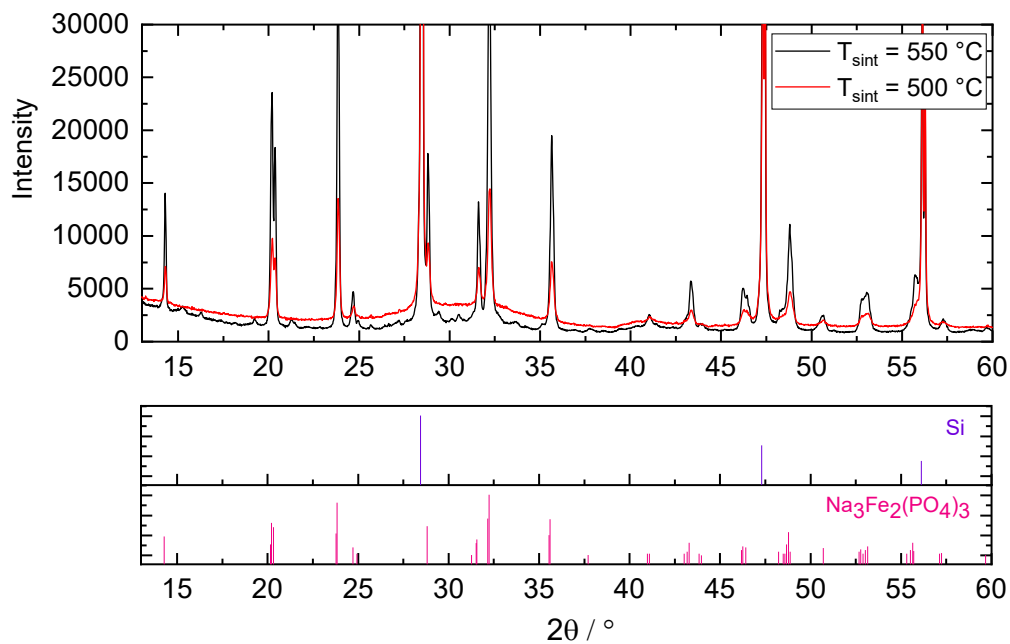


Figure 4.4 – Diffraction path generated by XRD analysis on NFP sintered tablets in air atmosphere, at $T_{sintering}$ of 550 °C and 500 °C, with responsible crystalline phases (Source: IKTS)

As foreseen, the sintering experiment performed at 500 °C generates few crystalline peaks of reduced intensity compared to the experiment at 550 °C: the former temperature, in fact, is closed to the glass transition temperature, at which the viscous flow and crystallization do not start yet.

The crystalline phases responsible for the detected peaks are the same for both experiments: excluding the higher peaks from silicon (added to identify the amorphous phases in XRD analysis), the main crystalline phase characterising the sintered samples is the NaSICON $\text{Na}_3\text{Fe}_2(\text{PO}_4)_3$. The crystallised phosphate has a monoclinic structure, mainly constituted by PO_4 tetrahedra and FeO_6 octahedra sharing edges and corners: they arrange in the so-called “lantern units” of $[\text{Fe}_2(\text{PO}_4)_3]$, creating an open and stable 3D framework for sodium ions migration [23].

The crystalline arrangement is showed in the following image Fig. 4.5.

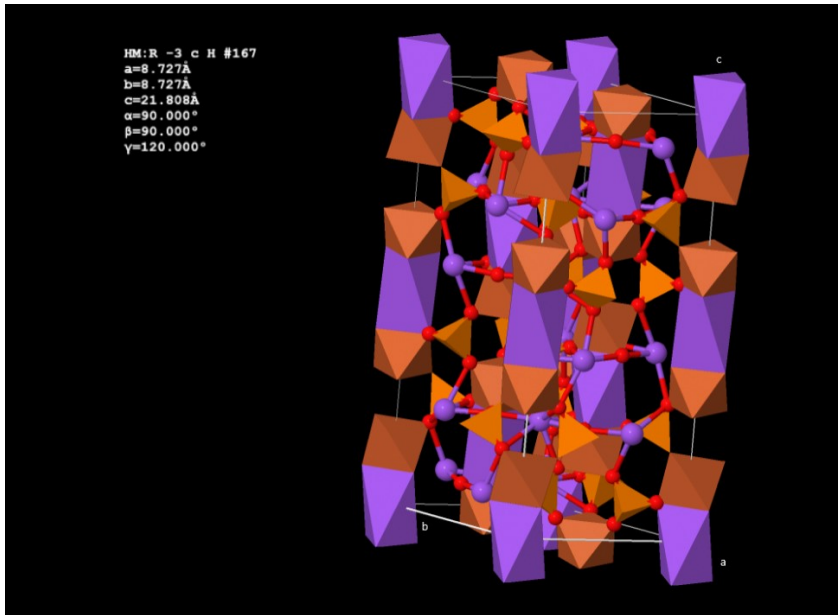


Figure 4.5 – Model of crystalline arrangement of $\text{Na}_3\text{Fe}_2(\text{PO}_4)_3$: PO_4 tetrahedra (light orange) connect to FeO_6 octahedra (dark orange) with oxygen atoms (red), leaving holes and channels for sodium to move (purple). Sodium atoms link also with oxygen to form trigonal bipyramids and octahedra (purple crystalline structures) (Source: ICSD database)

The weight percentage of Si and $\text{Na}_3\text{Fe}_2(\text{PO}_4)_3$ crystalline phases has been calculated with the software DIFFRAC.SUITE TOPAS; next, knowing the actual quantity of Si added to the powders (33 %wt.), the amount of detected crystalline phases has been proportionated and the residual has been identified as amorphous phase. Finally, the Si contribution has been subtracted and the effective percentage re-calculated, weighting the previous quantities on the remaining 2/3 of the structure.

The weight percentages of $\text{Na}_3\text{Fe}_2(\text{PO}_4)_3$ and amorphous residual phases are reported in Table 4.2, for both experiment at 550 °C and at 500 °C.

Experiment	$\text{Na}_3\text{Fe}_2(\text{PO}_4)_3$ phase [%wt.]	Amorphous phases [%wt.]
$T_{\text{sintering}} = 550 \text{ }^\circ\text{C}$	58.46	41.54
$T_{\text{sintering}} = 500 \text{ }^\circ\text{C}$	22.89	77.11

Table 4.2 – Calculated weight percentages of crystalline and amorphous phases in NFP glass-ceramics sintered in air atmosphere, at 550 °C and 500 °C (Source: IKTS)

Once more, the experimental data confirm the expectations: the amorphous phases constitute a high weight percentage, especially for the sintering experiment at 500 °C (77.1 %wt.), for which both the densification and the crystallization processes are limited by the reduced temperature for sintering procedure.

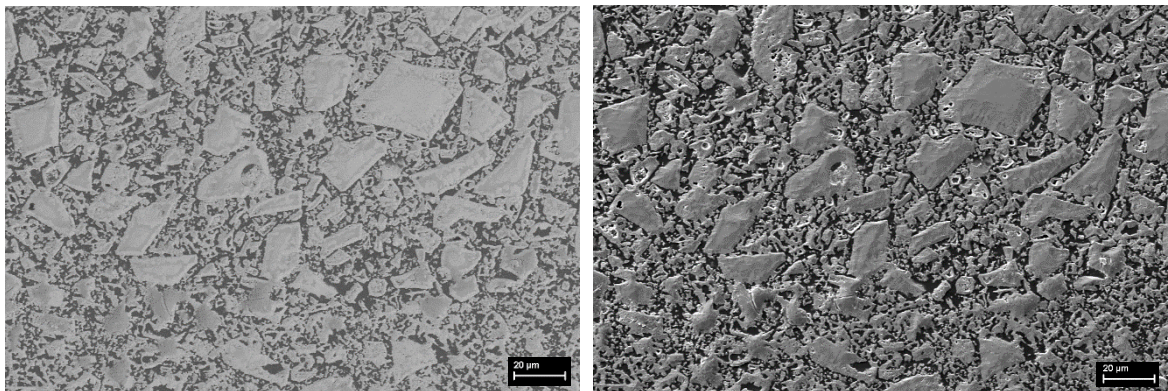
In addition, $\text{Na}_3\text{Fe}_2(\text{PO}_4)_3$ is composed by iron with oxidation number 3: this characteristic demonstrates that sintering in oxidizing conditions does not promote reduction, making the material not ideally usable as cathode.

The iron content (in this case, only Fe^{3+}) has been calculated and presented in Table 4.3.

Experiment	$\text{Na}_3\text{Fe}_2(\text{PO}_4)_3$ [%wt.]	$\text{Na}_3\text{Fe}_2(\text{PO}_4)_3$ [g/mol]	$\text{Na}_3\text{Fe}_2(\text{PO}_4)_3$ [moles]	Fe^{3+} [moles]
$T_{\text{sintering}} = 550 \text{ }^\circ\text{C}$	58.46	465.58	0.13	0.25
$T_{\text{sintering}} = 500 \text{ }^\circ\text{C}$	22.89	465.58	0.05	0.10

Table 4.3 – Moles of crystalline phase and iron content for 1 g of glass-ceramic material, sintered in air atmosphere at 550 °C and 500 °C (Source: IKTS)

To better identify the distribution of partially crystalline phases and their arrangement in the lattice, the structure sintered at 550 °C has been investigated with FESEM and EDX analyses. In Fig. 4.6 hereunder, FESEM images are showed for different degrees of magnification, obtained employing both BSE and SE.



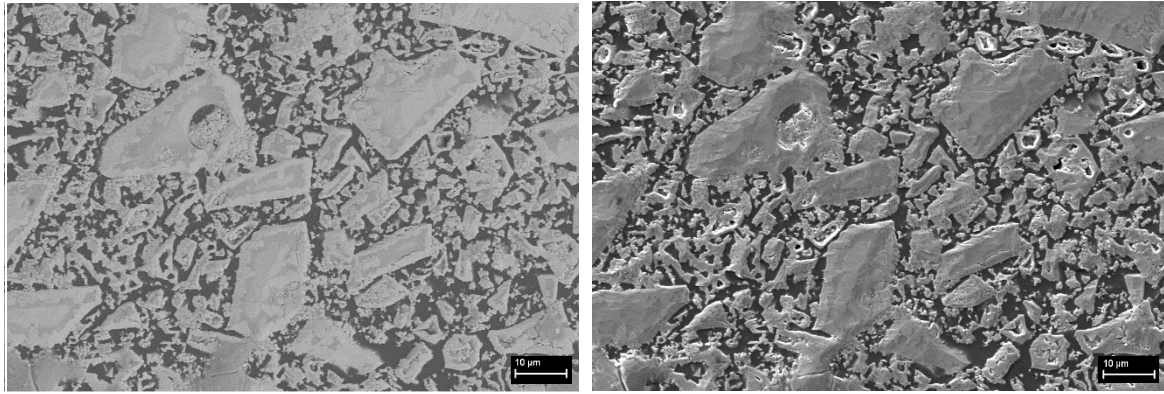


Figure 4.6 – FESEM images of NFP sintered structure at 550 °C in air atmosphere: on the left, figures obtained from detection of Back-Scattered Electrons, on the right of Secondary-Electrons (Source: IKTS)

As visible, the structure is formed by big crystalline grains (NaSICON phase $\text{Na}_3\text{Fe}_2(\text{PO}_4)_3$) surrounded by less-defined particles and dark areas, probably respectively indicating the amorphous phases and the void spaces. The lack of cohesion is a proof of the poor densification occurred during sintering.

The presence of numerous dark spots is justified by the calculated high average porosity percentage of $28\% \pm 2.3$, indicating that oxidizing atmosphere probably contributed to the creation of some pores and holes in the crystalline structure.

The EDX analysis (Fig. 4.7) highlights the forming elements in the structure: qualitatively, each lattice point is occupied by a prevailing quantity of oxygen, followed by sodium, phosphorous and iron. As visible in the FESEM figure below, there are two distinguishable zones: the darker ones (point n. 61 or 63) are characterised by more relevant presence of Na with respect to lighter points (n.60 or 64). It is also noticeable a difference related to the amount of oxygen: the smaller peaks, corresponding to a lower O_2 quantity, are detected for the dark areas (associable to lightweight zones in the lattice); on the contrary, for white-coloured zones are detected higher O_2 peaks, indicating a heavier structure.

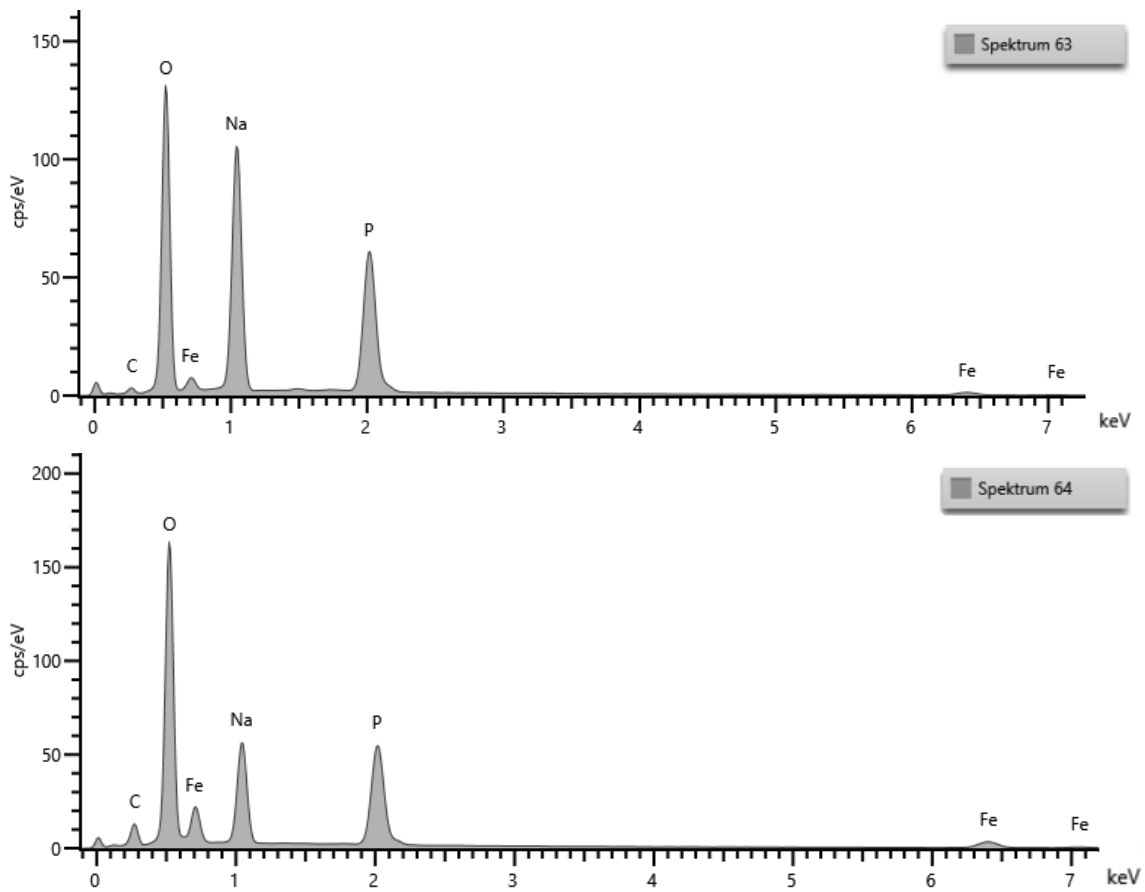
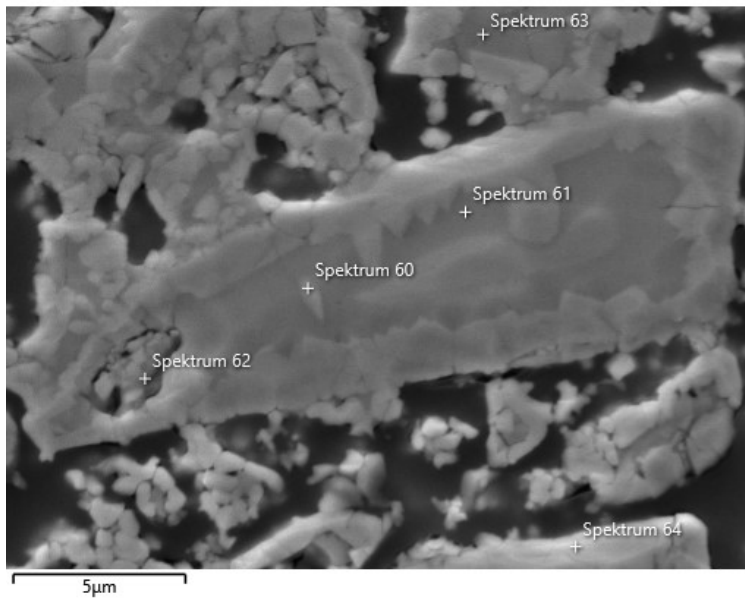


Figure 4.7 – FESEM image, associated to EDX spectra related to different points in the crystalline structure (Source: IKTS)

In air atmosphere, crystallization starts before the starting of sintering, and is especially observed as a surface crystallization. The high porosity and high content of unknown amorphous phases are related to the fact that pores and amorphous particles remain entrapped or surrounded by crystalline phases, therefore the occurring of densification by viscous flow is not possible.

Both the experiments (at sintering temperature of 550 °C and 500 °C) highlight the presence of NaSICON crystalline structure $\text{Na}_3\text{Fe}_2(\text{PO}_4)_3$, exclusively formed by iron in oxidized form (Fe^{3+}).

Therefore, the analyses proved the non-suitability of air conditions for sintering of powders to glass-ceramic material, since not leading to a good structure shrinkage, nor to the required crystalline phases promoting the ionic conduction and migration in the lattice.

4.2 Sintering behaviour in nitrogen

Several studies claim that heating processes performed in nitrogen atmosphere, if compared to procedures in air, enhance the densification of glass particles and the linear shrinkage [24]; the sintering is more pronounced in inert conditions, leading to highly densified and less porous glass-ceramics.

The HSM curves for NFP and NFPr heated in nitrogen, at 5 K/min up to 700 °C, are depicted in Fig. 4.8. The analysis of NFP trend proves the expectations: if compared with HSM curve in air, clearly the linear shrinkage in inert conditions is higher and the material densifies more; the NFPr instead, as in case of heating in air atmosphere, shows small volumetric reduction, hence results not to be suitable for further investigations.

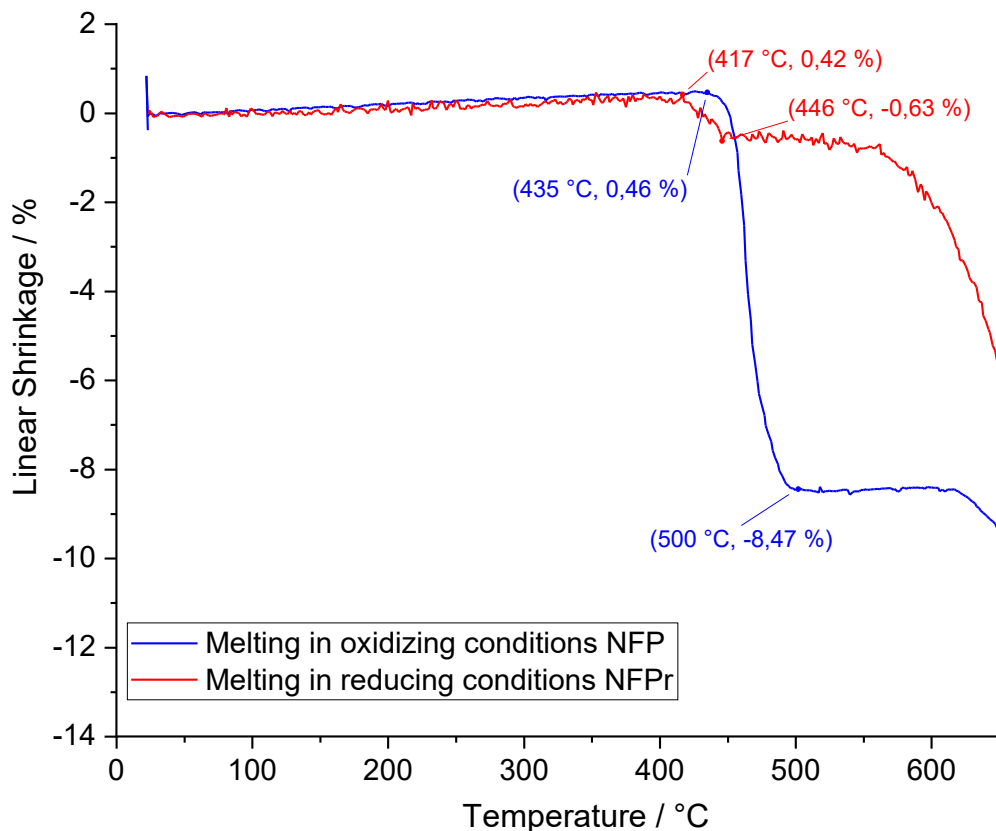


Figure 4.8 - Comparison of linear shrinkage curves for NFP (blue) and NFPr (red), heated in nitrogen atmosphere at 5 K/min, up to 700 °C (Source: IKTS)

Anyway, since the precursor glass matrix is composed by Fe^{3+} ions, it is necessary to reduce from Fe^{3+} to iron Fe^{2+} to obtain the triclinic crystalline form. If the sintering procedure in pure N_2 is compared with heating in H_2/N_2 [5], it comes out that the former leads to a reduction process, but occurring at higher temperatures and with NaFePO_4 among the crystalline phases, which is inactive as cathode material; differently, the addition of hydrogen in sintering atmosphere allows the reduction of Fe ions at lower temperature and the formation of proper crystalline phases.

Basing on these statements, it has been decided not to perform the sintering investigation in nitrogen, but directly experiment the heating treatment in a reducing atmosphere, in the next chapter.

The TGMS technique (Thermogravimetric Mass Spectrometry) has been applied on sodium-iron-phosphate during heating: the analysis consists in ionising the sample material, deflecting the positive ions and detecting them electrically according to the $\frac{m}{z}$ (mass to charge ratio). Since most of the individuated ions bring a single positive charge, it follows that $\frac{m}{z}$ coincides with the molar mass of the molecule or atom identified. Specifically, the investigation aims at detecting differences in the possible formation of H_2O , CO_2 , O_2 molecules while heating in inert atmosphere (N_2), in comparison with a reducing atmosphere (95 vol.% N_2 - 5 vol.% H_2). The latter will be analysed in the following chapter, dealing with treatment in Varigon conditions (95-97 vol.% Ar and 3-5 vol.% H_2). The intent is to demonstrate that reducing conditions are the ideal ones to be applied during sintering, because leading to scarce oxygen formation with respect to the same procedure performed in normal air or in nitrogen.

The collected data are represented in graphs, showing the MS electrical signal (A/mg) in function of the sintering temperature, for a fixed value of $\frac{m}{z}$. The heating procedure was performed at 5 K/min, up to 800 °C.

The following plots (Fig. 4.9) report the results for the heating in nitrogen of NFP material, and NFP mixed with the 5 %wt. of graphite as carbon source. Starting from the graph on top, the Thermo-Gravimetric analysis shows that, as in the case of heating in air atmosphere, the mass loss is limited to 0.2 % and not of considerable relevance. Below, the first plot indicates the ionic current signals for H_2O ions ($\frac{m}{z} = 18$): the water formation

is quite coincident in the two cases, reporting a maximum at 90 °C around $2 \cdot 10^{-14}$ A/mg. This effect is related to the water desorption from the surface of the glass particles, in form of physically sorbed H₂O and chemically sorbed OH-groups: the cause could be related to the previous sorption during grinding process and to the high specific surface of NFP powders. It can be stated that the small values detected correspond to the expectations, since the atmosphere and the carbon addition do not bring any additional contribution for the hydrogen formation.

The next graphs depict the electrical signal deriving from detection of CO₂ ions ($\frac{m}{z} = 44$) and of carbon ions ($\frac{m}{z} = 12$), showing mostly limited values up to 500 °C (signal smaller than $1.0 \cdot 10^{-15}$ A/mg for the former, smaller than $2.0 \cdot 10^{-16}$ A/mg for the latter), therefore proving that it is scarcely probable to face reduction reactions in nitrogen. Differently from the previous graph, the contribution of carbon addition is clearly visible, with black curves abruptly increasing from 600 °C on: the phenomenon is attributed to the tendency of carbon to reduce the oxidized NFP at high temperatures, with consequent higher emission of CO₂ and CO.

Finally, the oxygen formation is showed in the last plot ($\frac{m}{z} = 16$, characteristic of O⁺ ions). It is reported that the ions do not derive from free O₂ in atomic or molecular form, but from fragmentation of H₂O or CO₂ molecules in the ioniser of the spectrometer. As detectable, the MS signals derive mainly from H₂O ions, presenting higher values with respect to CO₂ or C signals.

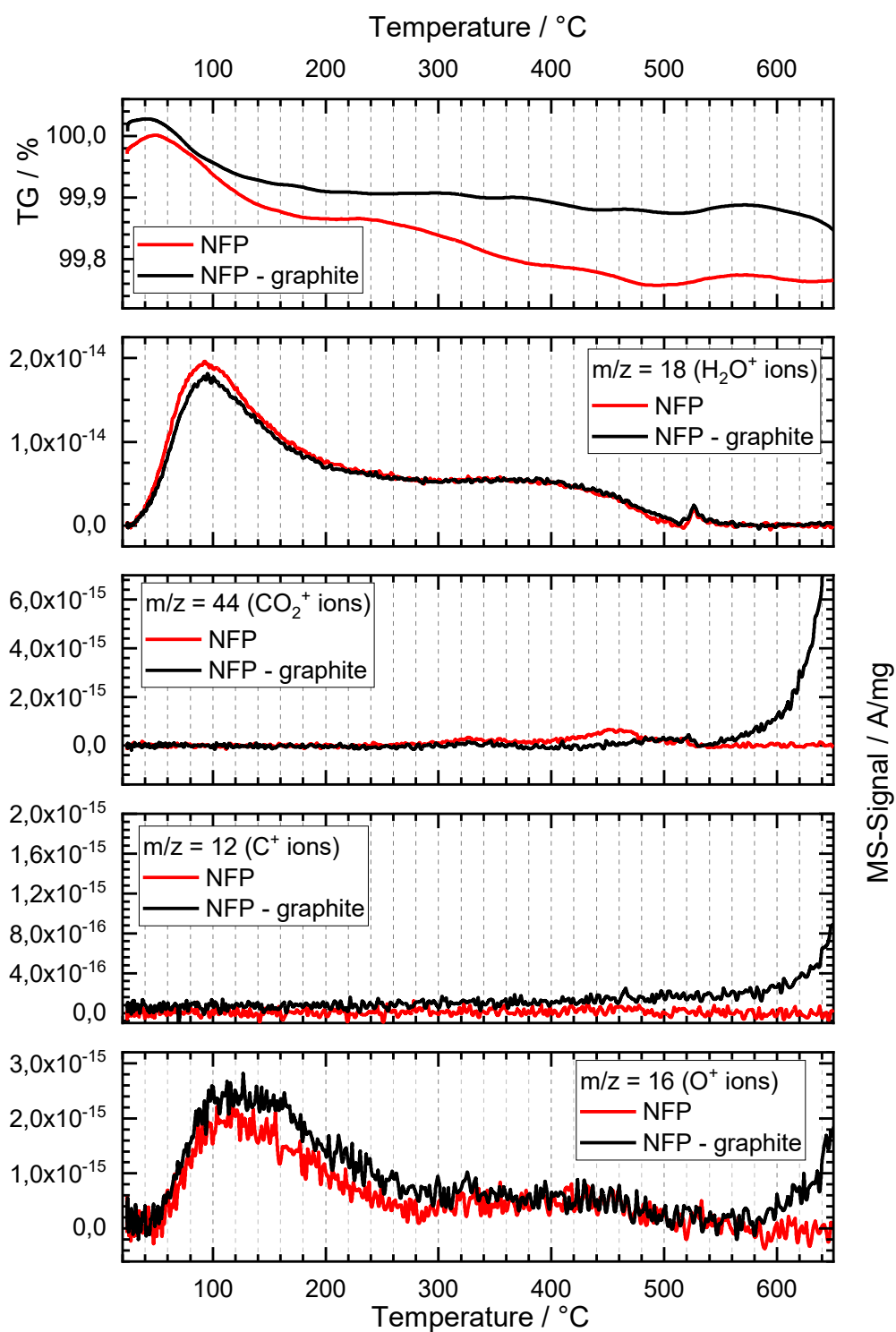


Figure 4.9 – Plots from TGMS analysis on NFP and NFP-5 %wt. of graphite, heated at 5 K/min up to 800 °C in nitrogen atmosphere (Source: IKTS)

4.3 Sintering behaviour in Varigon

Several studies [3,5,17,18] agree on the possibility to create a new active cathode material by glass-ceramic production in reducing atmosphere. The cathode candidate is a triclinic $\bar{P}1$ structure as the sodium-iron-phosphate $\text{Na}_2\text{FeP}_2\text{O}_7$, which provides high current density, high rate performance and good cyclability due to its inner structure. Indeed, the reducing sintering conditions promote the reduction of iron from Fe^{3+} (in the precursor glass) to Fe^{2+} , fundamental for the formation of large tunnel structure for Na^+ migration. The employed gas for reducing atmosphere is the so-called “Varigon”, composed by a variable percentage of 3-5 vol.% of hydrogen and 95-97 vol.% of argon.

Among other techniques, the effectiveness of reducing action can be proved performing a TGMS investigation in a reducing atmosphere composed by 95 vol.% N_2 - 5 vol.% H_2 and comparing the results with the detected data from previous chapter, related to the heating procedure in nitrogen.

4.3.1 HSM and TGA-DTA procedures in Varigon

As in the case of air atmosphere, NFP powders have been analysed in Varigon atmosphere through Hot Stage Microscopy and Thermo-Gravimetric and Differential Thermal Analysis. The heating procedure was the same: the batch has been heated to 700 °C with heating rate of 5 K/min and next cooled down at rate of 10 K/min.

The obtained curves versus temperature are showed in the following image (Fig. 4.10).

As visible from the trend of percentage mass loss, the heated powders are stable and mass reduction does not occur significantly at any temperature (the maximum reduction is around 0.2 %).

The DTA curve shows, as expected, a starting endothermic trend, with change of slope from 473 °C (glass transition temperature) and maximum peak at 501.7 °C. The crystallization phase is represented by two following exothermic peaks, at 519.5 °C and

543 °C respectively: in reducing conditions, the crystallization occurs in two steps at different temperatures, indicating the presence of two main crystalline phases, or a phase transformation from the first to the second one.

In contrast to the experiment in air conditions, the HSM curve shows a good densification: the linear shrinkage seems to start at 416 °C and at 498 °C is more than 9 % (volume reduction of 9.49 %).

In reducing atmosphere, as well as in the oxidizing one, the window of temperatures for sintering experiments is identified to be around 500-550 °C.

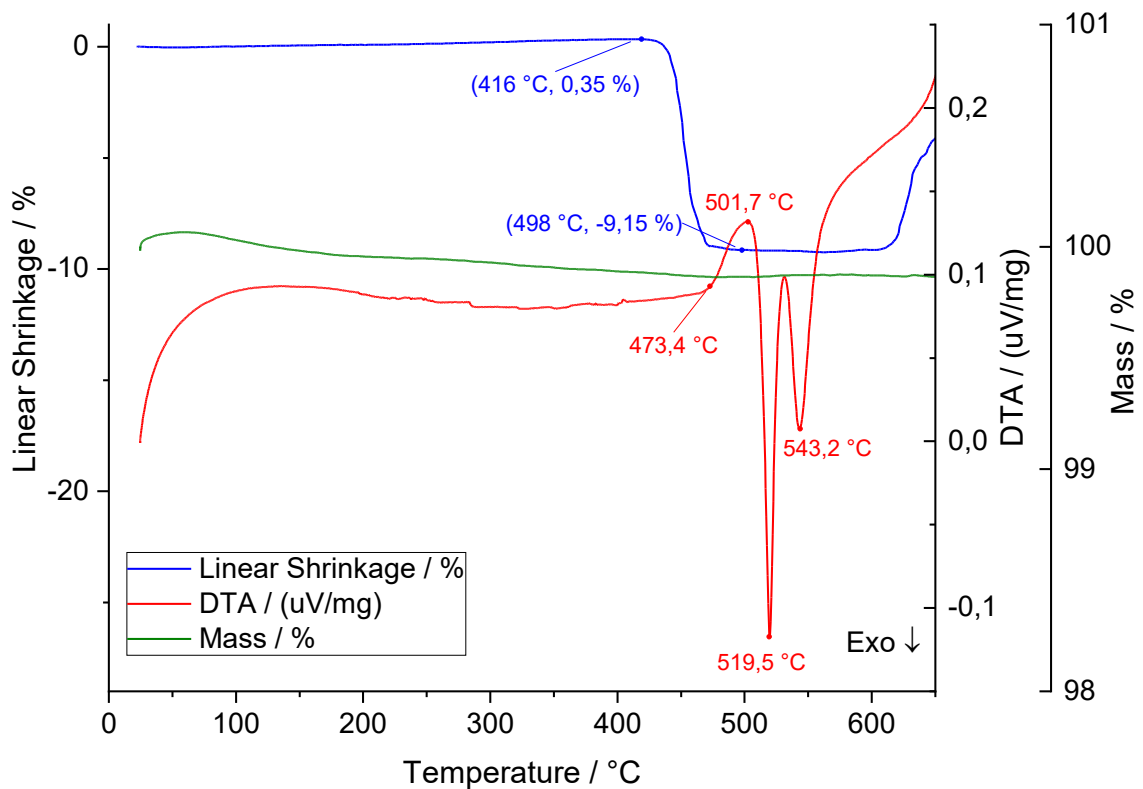


Figure 4.10 – HSM curve (blue), compared with TGA-DTA curves (red and green), for NFP material heated in Varigon atmosphere at 5 K/min, up to 700 °C (Source: IKTS)

The sodium-iron-phosphate melted in reducing conditions (NFPr) has been subject to HSM analysis and the curve of volume reduction in function of temperature has been matched with the trend of NFP (Fig. 4.11). It is verifiable that NFPr powders are characterised by scarce densification even by heating in reducing atmosphere: in fact, in the densification temperature range (400-500 °C) the linear shrinkage is 0.97 % and not

comparable with the values of NFP sintered powders. Moreover, the batch is likely to densify again around 600 °C, which anyway is a too high temperature for a successive sintering.

Thus, the sintering behaviour of NFPr has not been investigated in this study, due to its poor densification between 400 °C and 500 °C.

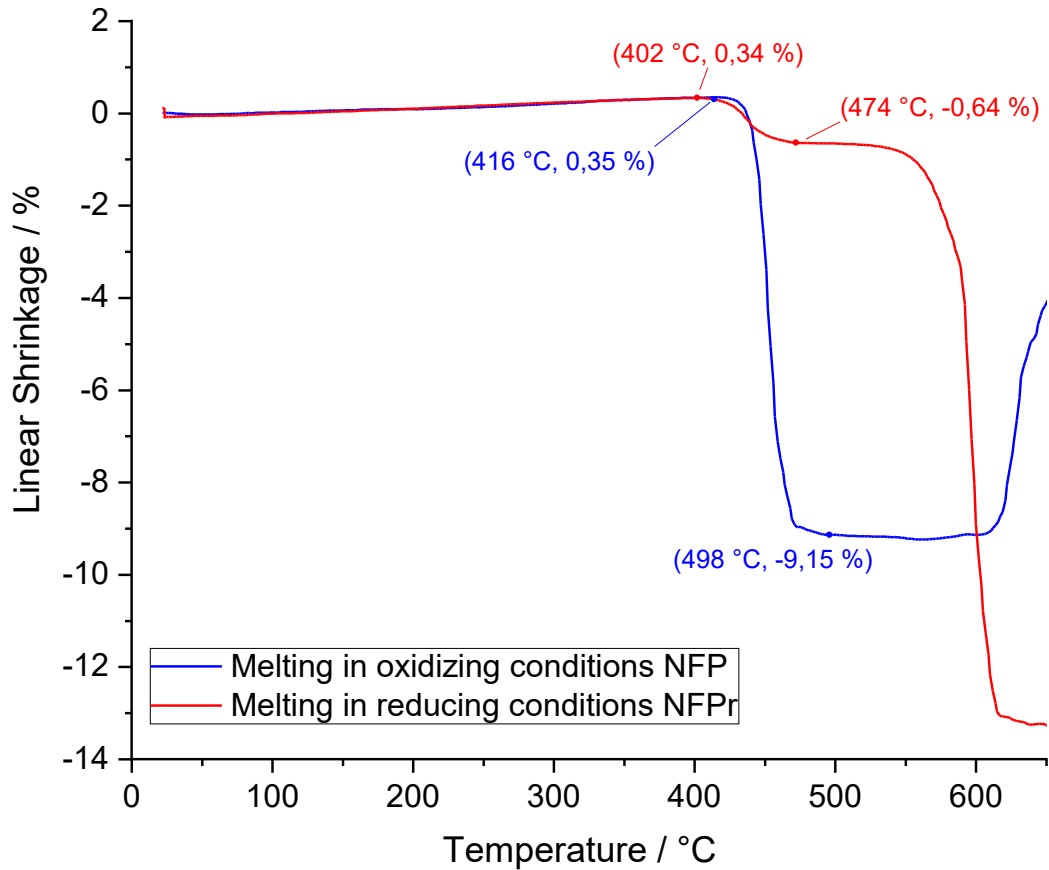


Figure 4.11 – Comparison of linear shrinkage curves for NFP (blue) and NFPr (red), heated in Varigon atmosphere at 5 K/min, up to 700 °C (Source: IKTS)

As previously mentioned, TGMS analysis has been performed on NFP treated in N₂-H₂ reducing atmosphere and compared with the results from TGMS on NFP material heated in nitrogen. The plots are showed in Fig. 4.12 hereunder.

Concerning the mass loss, the trends of mass reduction in N₂ and N₂-H₂ atmosphere are comparable up to 460-480 °C, so up to the glass transition temperature. Above T_g, the diffusion processes and reactions between NFP material and atmosphere are possible: since the curve for reducing heating conditions is more pronounced over T_g, it is deduced that, in comparison to the inert atmosphere, the reducing one is more reactive with NFP.

The curves related to H₂O ions are similar up to 400 °C; over that temperature, the hydrogen in the gas atmosphere (red curve) starts reacting with oxygen in NFP structure and a growth in H₂O formation is detected. The reduction reaction proceeds slowly for temperatures below 600 °C (as visible from the slight increase in the MS signal), probably because of the high viscosity of NFP material, or due to the slow formation of crystalline phases. Over 600 °C, a more intense formation of H₂O is detected, due to the lower viscosity of NFP material and faster diffusion processes, leading to the formation of new crystalline phases.

Differently, the trends related to $\frac{m}{z} = 44$ (CO₂ ions) are quite similar, because there was no additional carbon in the starting material.

The combination of H₂ from heating atmosphere with O₂ from NFP material makes the curve of oxygen ions increasing from 600 °C on (the MS signal reaches the value of $1.6 \cdot 10^{-14}$ A/mg at 640 °C): indeed, it is probable that, for high temperatures, the water vapour release is enhanced in reducing atmosphere.

In air conditions some crystallization concurred with the sintering process, limiting therefore the densification of glass material; conversely, for reducing atmosphere the TGMS results demonstrate that the crystallization process seems to be limited to some extent, and densification of amorphous phase is possible.

Hence, it has been proved that the employment of a reducing atmosphere promotes reducing reactions in the batch and the formation of the desired glass-crystalline cathode material.

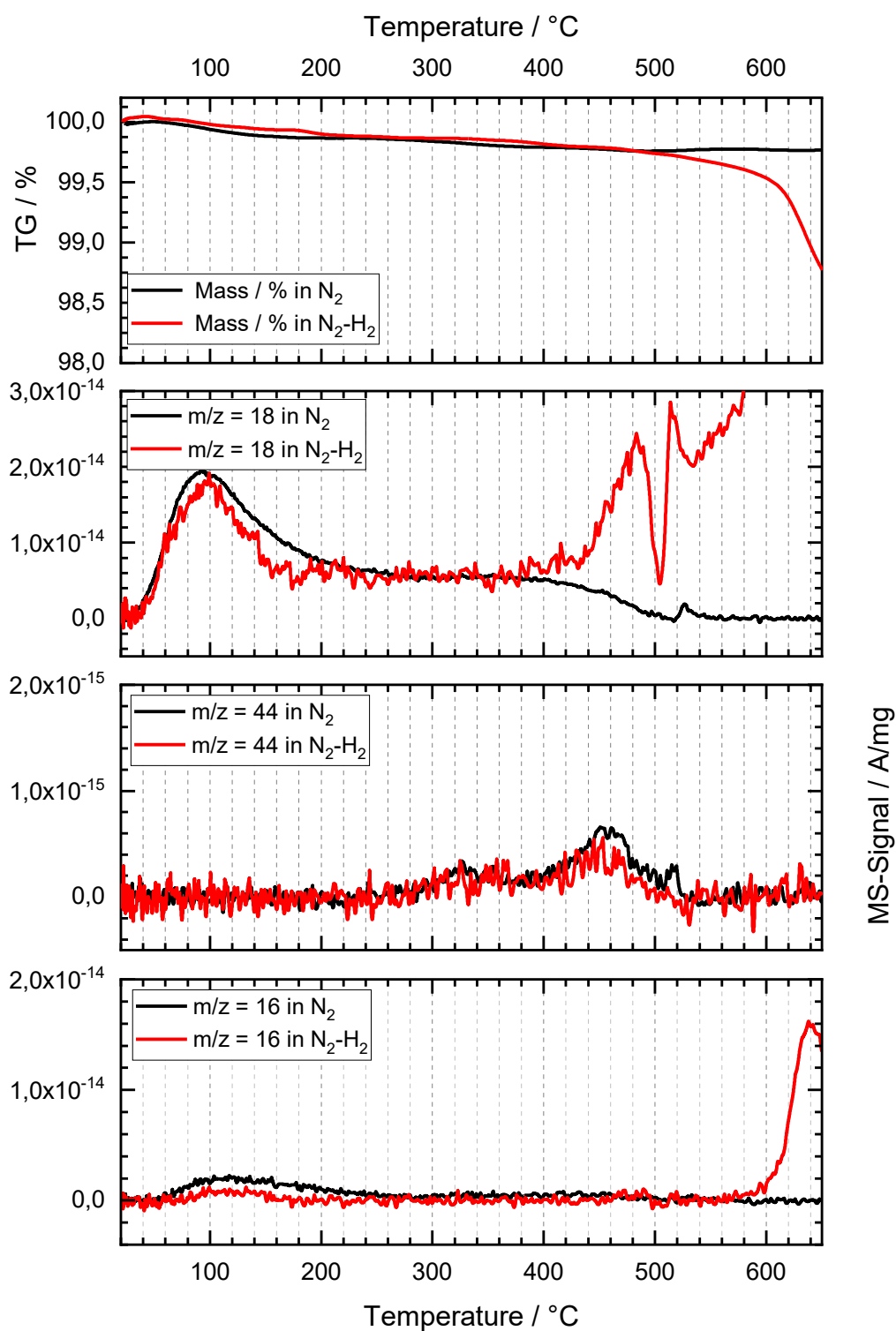


Figure 4.12 – Comparison of plots from TGMS analysis on NFP, heated at 5 K/min up to 800 °C in nitrogen (analysed in previous chapter) and in reducing atmosphere (Source: IKTS)

4.3.2 Sintering and phase formation in Varigon

As anticipated, also the sintering experiment in reducing atmosphere has been carried on at 550 °C, with heating rate of 5 K/min and soaking time of 15 minutes. The chosen sintering temperature, in fact, is expected to be the one at which the crystallization phase is complete and concluded, as visible from DTA curve.

The sintering parameters are the same of the experiment in air atmosphere: therefore, the effects of different heating atmospheres have been compared in terms of densification, crystalline phases and iron content.

As visible from the HSM trend (Fig. 4.10) the batch sintered in reducing environment densifies more than the same material processed in air: the following table (Table 4.4) proves the graphical evidence, showing the increase of density of a unit, with respect to the same sample treated in air, for which the value barely increases.

Experiment	Density Before Sintering ρ [g/cm ³]	Density After Sintering ρ [g/cm ³]
<i>Sintering in air</i>	1.89 ± 0.01	1.90 ± 0.01
<i>Sintering in Varigon</i>	1.92 ± 0.01	2.58 ± 0.01

Table 4.4 – Calculated density values, before and after sintering procedure, for NFP samples treated in air and Varigon conditions (Source: IKTS)

The difference in the structure shrinkage is evident if the sintered coin-shaped samples are observed: from the picture hereunder (Fig. 4.13) the tablet sintered in air is clearly distinguishable, because of whitish colour but especially of the bigger dimension, due to poor shrinkage; the reduced sample instead, not subject to oxidation process, is darker and less bulky, because of proper densification occurred during sintering.

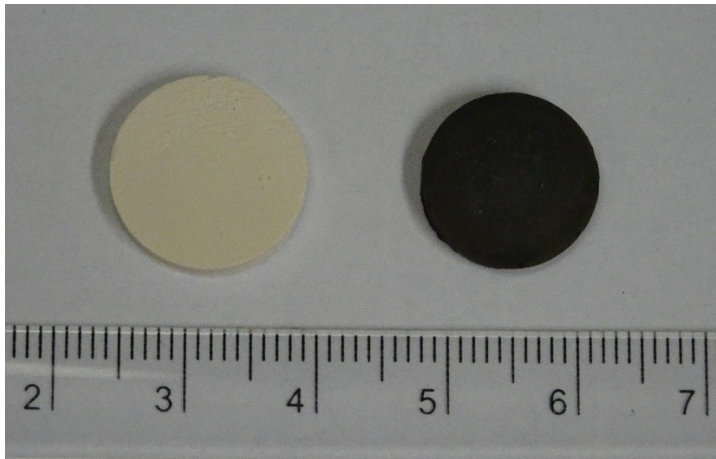


Figure 4.13 – Picture of sintered tablets: on the left-hand side, the one treated in air atmosphere, on the opposite side the one treated in Varigon

The crystalline phases detected are illustrated in the following graph (Fig. 4.14), which correlates the diffracted pattern obtained with XRD analysis of sintered NFP powders in Varigon with the one in air atmosphere.

Contrarily to the latter, mainly characterised by NaSICON phase $\text{Na}_3\text{Fe}_2(\text{PO}_4)_3$, the experiment in reducing conditions produces glass-ceramics whose responsible crystalline phases are $\text{Na}_3\text{Fe}_2(\text{PO}_4)_3$ and the monoclinic structures $\text{Na}_7\text{Fe}_3(\text{P}_2\text{O}_7)_4$ and $\text{NaFe}_3\text{P}_3\text{O}_{12}$. Hence, it can be deduced that treatment in reducing conditions generates more complex structures, determined by the co-existence of several crystalline phases.

As evident, the NaSICON phase is still responsible for the higher crystalline peaks (at 2θ angles of 20° , 24° , 32° , 36°), while the monoclinic ones are related to smaller peaks, especially for diffraction angles minor than 20° and in the range 25° - 35° .

The monoclinic sodium-iron-pyrophosphate $\text{Na}_7\text{Fe}_3(\text{P}_2\text{O}_7)_4$ is a crystalline structure formed by FeO_6 octahedra and diphosphates P_2O_7 , combined to form a 3D network made of $[\text{Fe}_3(\text{P}_2\text{O}_7)_4]$ groups [25]. The corners-sharing tetrahedra and octahedra form different parallel planes, which constitute the diffusion paths for Na^+ migration; the sodium ions, as noticeable from Fig. 4.15, are distributed over several sites and form different bonds with oxygen atoms.

The monoclinic structure $\text{NaFe}_3\text{P}_3\text{O}_{12}$, part of family of Alluaudites, is again formed by phosphate tetrahedra PO_4 and iron oxides octahedra FeO_6 , creating tunnels for intercalation and de-intercalation of sodium ions. Unlike NaSICON structure

$\text{Na}_3\text{Fe}_2(\text{PO}_4)_3$ and monoclinic $\text{Na}_7\text{Fe}_3(\text{P}_2\text{O}_7)_4$, its unit cell is composed by a single sodium atom, reason why the crystalline structure in Fig. 4.16 presents few Na atoms linked to oxygen.

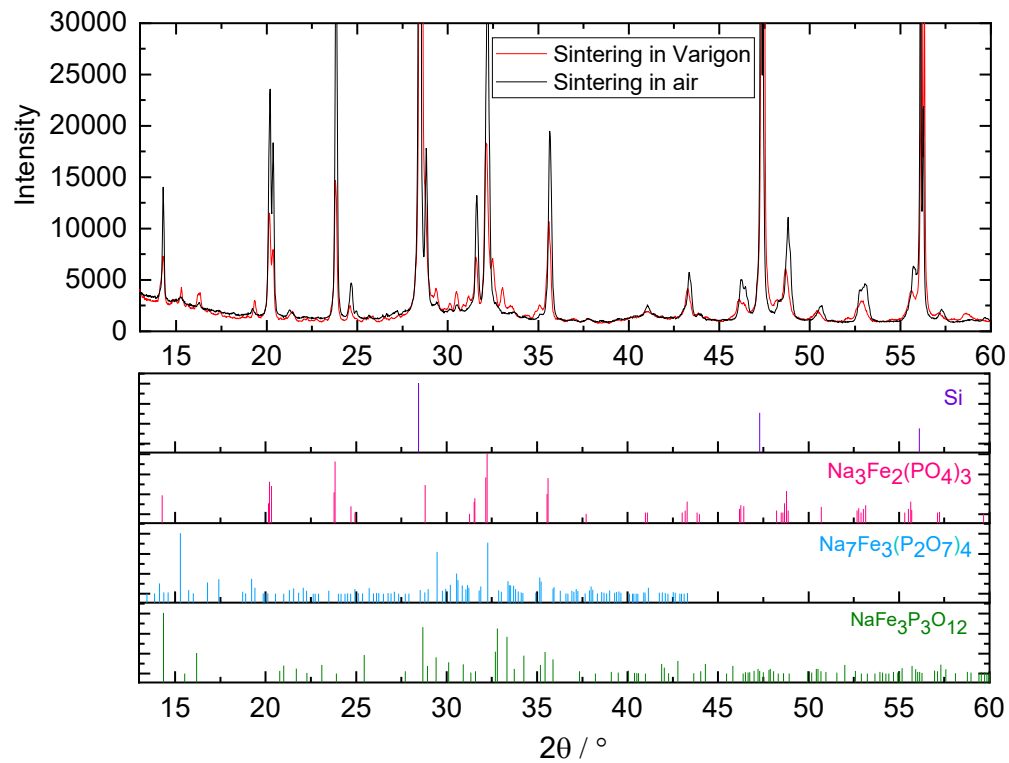


Figure 4.14 – Diffraction path generated by XRD analysis on NFP sintered tablets in air and Varigon atmosphere, with responsible crystalline phases (Source: IKTS)

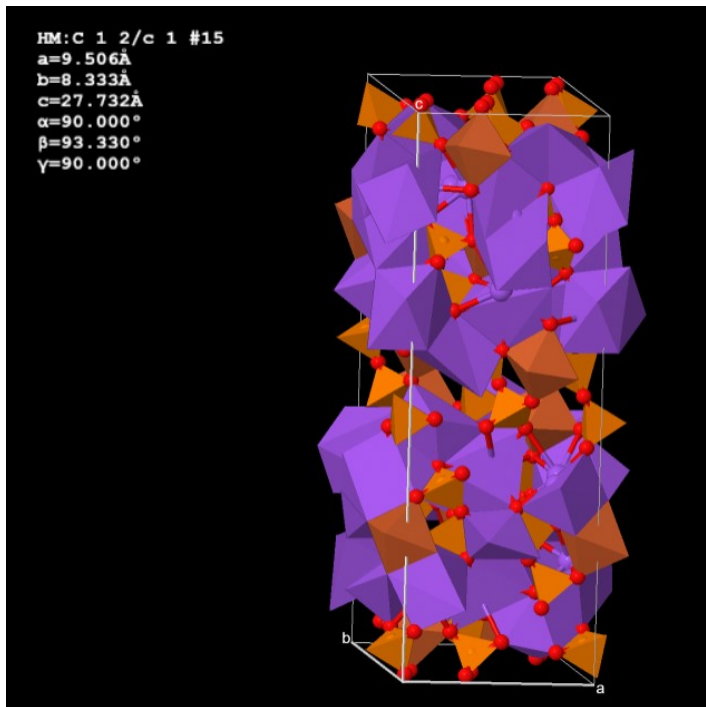


Figure 4.15 – Model of crystalline arrangement of $\text{Na}_7\text{Fe}_3(\text{P}_2\text{O}_7)_4$, with P_2O_7 tetrahedra (light orange), FeO_6 octahedra (dark orange) and Na atoms linked to oxygen (in red) forming trigonal bipyramids and distorted prisms (purple structures)
(Source: ICSD database)

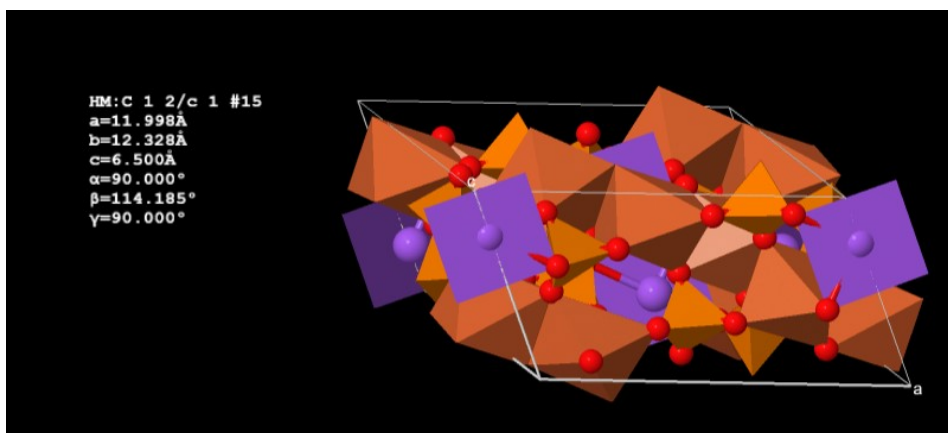


Figure 4.16 - Model of crystalline arrangement of $\text{NaFe}_3\text{P}_3\text{O}_{12}$, with PO_4 tetrahedra (light orange), FeO_6 octahedra (dark orange) and Na atoms (purple) linked to four oxygen atoms (red)
(Source: ICSD database)

The amount of crystalline phases has been calculated with DIFFRAC.SUITE TOPAS and proportioned by subtraction of Si contribution (not present in the effective sintered material): as in case of sintering in air, the remaining not-detected phases have been

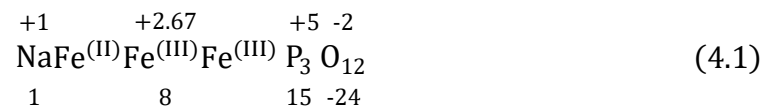
considered as the residual amorphous material in the glass-ceramic structure. The calculated percentages in weight are reported in Table 4.5 and analysed with the ones from experiment in air conditions.

Experiment	Na ₃ Fe ₂ (PO ₄) ₃ phase [%wt.]	Na ₇ Fe ₃ (P ₂ O ₇) ₄ phase [%wt.]	NaFe ₃ P ₃ O ₁₂ phase [%wt.]	Amorphous phases [%wt.]
<i>Sintering in air</i>	58.46	–	–	41.54
<i>Sintering in Varigon</i>	19.37	36.73	3.25	40.65

Table 4.5 – Percentages in weight of crystalline and amorphous phases in NFP glass-ceramics sintered in air and Varigon atmosphere, soaked for 15 minutes at 550 °C (Source: IKTS)

Concerning the crystalline part, the tablets sintered in Varigon are mainly formed by monoclinic phase Na₇Fe₃(P₂O₇)₄ (36.73 %wt.), followed by NaSICON Na₃Fe₂(PO₄)₃ (19.37 %wt.) and by a small part of alluaudite NaFe₃P₃O₁₂ (3.25 %wt.). The amorphous percentage is still high, indicating that the chosen sintering conditions are not likely to be the ideal for the formation of a complete crystalline structure.

Despite the good densification and the development of a complex crystalline framework with respect to the NFP treated in air, nonetheless the iron content is still mainly Fe³⁺ (Table 4.6). Indeed, it can be easily calculated that Na₃Fe₂(PO₄)₃ and Na₇Fe₃(P₂O₇)₄ are respectively formed by two and three atoms of Fe, with oxidation number 3. The monoclinic NaFe₃P₃O₁₂ instead, presents partially reduced iron, as determined below (Eq. 4.1):



Hence, the alluaudite phase is identified by iron with oxidation number equal to 2.67, and each molecule is composed by one atom of Fe²⁺ and two atoms of Fe³⁺.

Crystalline Phases [type]	Crystalline Phases [moles]	Fe ³⁺ [moles]	Fe ²⁺ [moles]
Na ₃ Fe ₂ (PO ₄) ₃	0.042	0.083	–
Na ₇ Fe ₃ (P ₂ O ₇) ₄	0.036	0.108	–
NaFe ₃ P ₃ O ₁₂	0.007	0.014	0.007

Table 4.6 - Moles of crystalline phases and iron content for 1 g of glass-ceramic material, sintered in Varigon atmosphere at 550 °C for 15 minutes (Source: IKTS)

The procedure in Varigon, at sintering temperature of 550 °C held for 15 minutes, provides a glass-ceramic material whose structure contains iron in reduced form (in NaFe₃P₃O₁₂ phase), but just in small quantity. This aspect is proved from the calculation of iron content: hypothesizing 1 g of sintered material, the total moles of Fe³⁺ amount to 0.20, the moles of Fe²⁺ are just 0.007 and the ratio Fe²⁺/Fe³⁺ is 0.03.

Thus, it is evident that the reducing sintering atmosphere partially contributes to the formation of the active cathode material, but it is still fundamental to deeply investigate all the heating parameters, which could modify the framework characteristics.

The FESEM and EDX images show a strongly densified structure, totally different from the material sintered in air (depicted in Fig. 4.6): as visible in Fig. 4.17, the framework is less porous (the calculated porosity percentage amounts to 4.1 % ± 0.8) and definitely more cohesive. It is detectable a distinction between more uniform zones (the crystalline ones, labelled with “1” in picture in bottom-left corner) and disordered and chaotic areas (labelled with “2”) probably due to the massive presence of amorphous unknown phases.

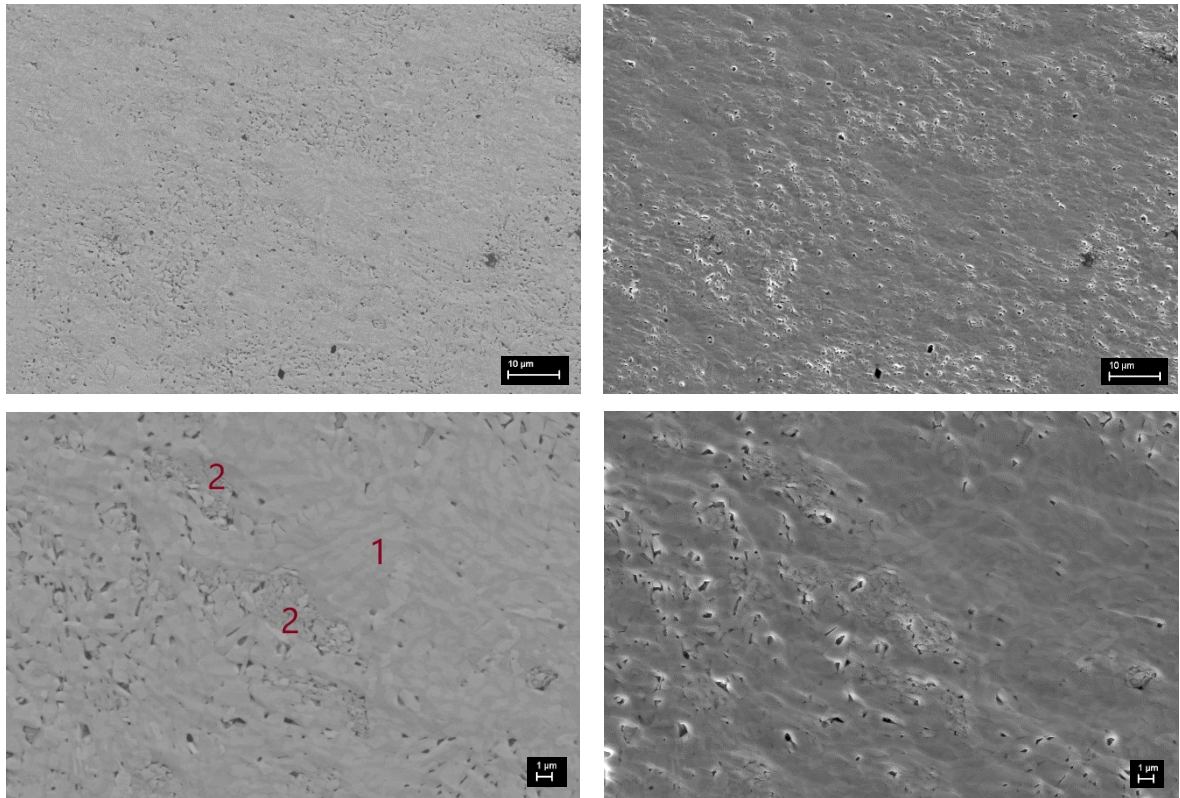


Figure 4.17 – FESEM images of sintered NFP structure at 550 °C in Varigon atmosphere: on the left, figures obtained from detection of Back-Scattered Electrons, on the right of Secondary-Electrons (Source: IKTS)

The EDX spectra hereunder (Fig. 4.18) present the constituting elements in different points of the lattice. As in case of sintering in air, there are some visibly darker zones (points n. 65 and 68), due to elements with small atomic number, and light areas (points n. 66 or 67) generated from the stronger deflection of electronic beams, due to particles with bigger atomic number. From EDX spectra, it is visible that darkened regions are characterised by higher content of Na and P, and smaller content of O₂, with respect to the lighter points.

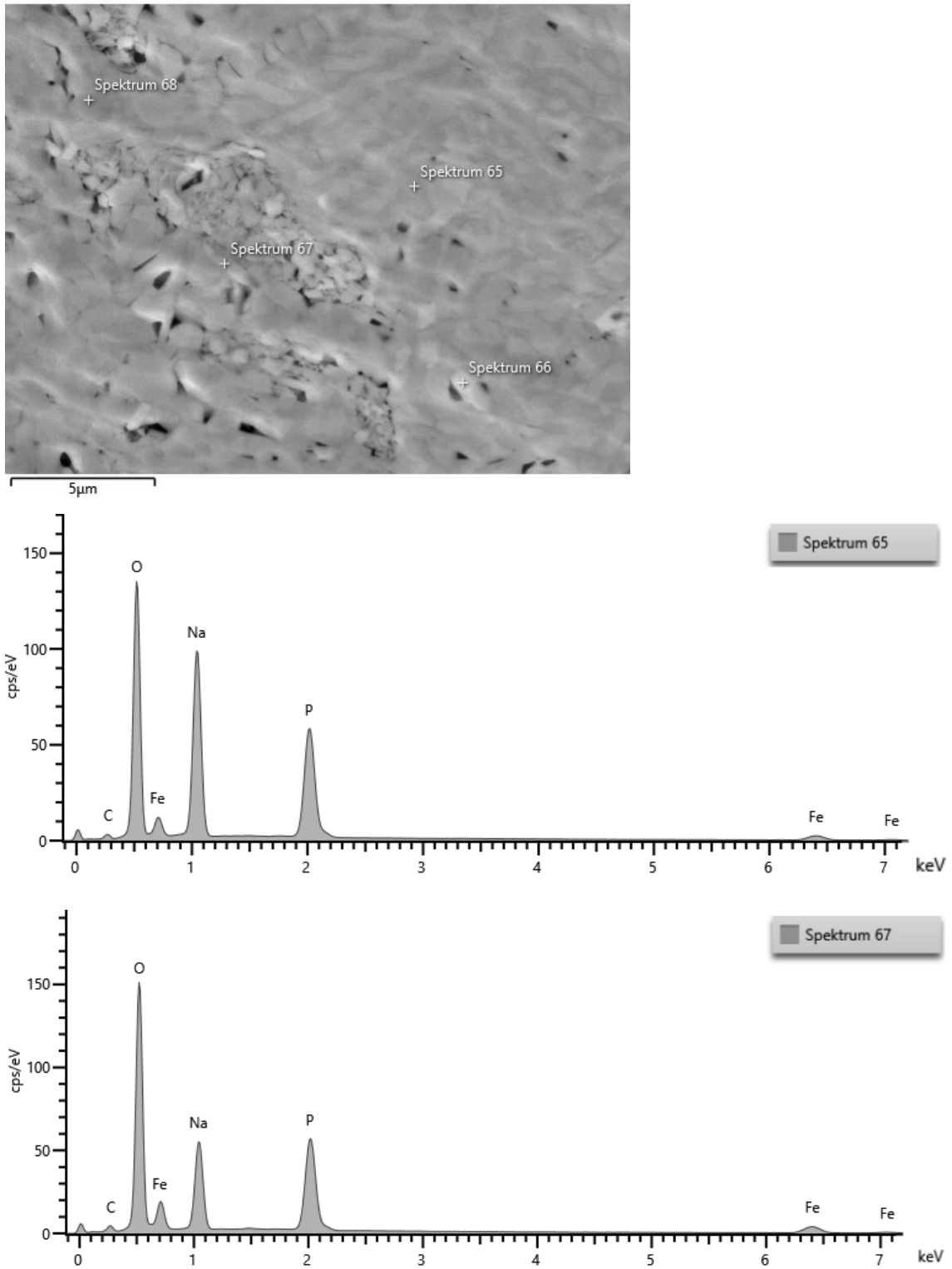


Figure 4.18 - FESEM image, associated to EDX spectra related to different points in the crystalline structure (Source: IKTS)

4.3.2.1 Optimization of sintering temperature and soaking time

The experiment in Varignon conditions, with heating rate of 5 K/min, sintering temperature 550 °C and soaking time of 15 minutes, demonstrated that change of heating atmosphere promotes the reduction of iron in the glass material structure, giving however a small contribution. It has been proved that the sintered framework is still formed by a considerable amount of amorphous phases, and that the crystalline components are mainly with Fe³⁺, rather than Fe²⁺. Thus, it has been necessary to investigate the variation of other sintering parameters, with the aim of identifying a sufficiently densified structure, whose crystalline phases are composed by iron in reduced form.

From DTA curve, the sintering temperature was previously set at 550 °C, because indicating the point at which the crystallization phase is probably completed; however, it was still not clear whether both exothermic peaks were related to crystallization phases, or if instead the one at higher temperature was the result of a phase transformation. Hence, the first modification consisted in lowering the sintering temperature to 500 °C and 520 °C: the aim was to understand if the crystalline phases are already forming at lower temperatures and, in case, if they are different from the detected phases at the higher temperature.

Moreover, the soaking time has been increased from 15 to 60 minutes, exposing samples to higher time for crystallization, reduction of Fe³⁺ to Fe²⁺ and possible phase transformations.

Since the heating atmosphere and heating rate (5 K/min) were unchanged, the sintered samples demonstrate a densification similar to the material sintered with previous procedure: from an average density of 1.98±0.01 g/cm³ before sintering, the value is calculated to be 2.62±0.01 g/cm³ after the heat treatment.

The detected crystalline phases are shown in the XRD pattern in the following image (Fig. 4.19) in association to the Bragg peaks of previous experiment (T_{sintering} equal to 550 °C, holding time of 15 minutes).

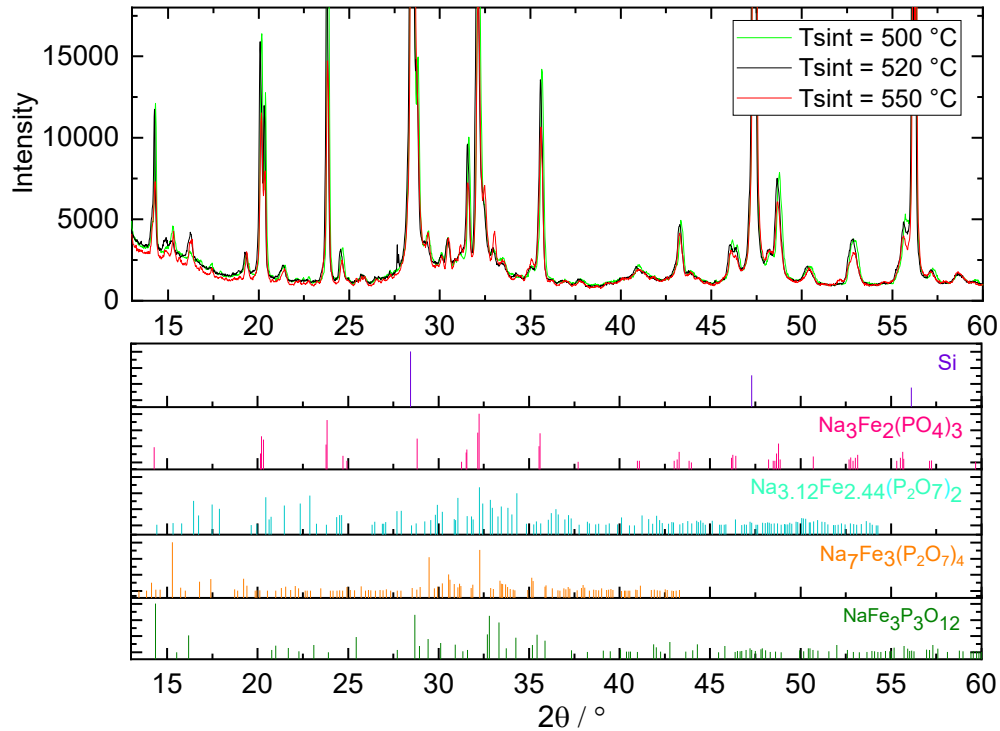


Figure 4.19 – Comparison of diffraction paths generated by XRD analysis on sintered tablets in Varigon, at 500 °C and 520 °C with soaking time of 60 minutes (green and black curves), at 550 °C with soaking time of 15 minutes (red curve), with responsible crystalline phases (Source: IKTS)

The detected crystalline structures are the NaSICON $\text{Na}_3\text{Fe}_2(\text{PO}_4)_3$ and monoclinic pyrophosphate $\text{Na}_7\text{Fe}_3(\text{P}_2\text{O}_7)_4$, as in the previous experiment in Varigon, and the triclinic phase $\text{Na}_{3.12}\text{Fe}_{2.44}(\text{P}_2\text{O}_7)_2$. The prevailing crystalline arrangement is still the monoclinic $\text{Na}_7\text{Fe}_3(\text{P}_2\text{O}_7)_4$, followed by $\text{Na}_3\text{Fe}_2(\text{PO}_4)_3$, as reported in the calculated weight percentages in Table 4.7.

The most relevant aspect is the presence of triclinic framework $\text{Na}_{3.12}\text{Fe}_{2.44}(\text{P}_2\text{O}_7)_2$: the non-stoichiometric pyrophosphate, already detected in previous investigations [5,17], has a crystal structure similar to $\text{Na}_2\text{FeP}_2\text{O}_7$ (with corner-shared FeO_6 octahedra linked to P_2O_7 units to form the 3D path for Na migration [4]).

As demonstrated below (Eq. 4.2), it is exclusively characterised by Fe^{2+} , providing the proper structure for good ionic movement:



The triclinic phase, whose crystalline arrangement is depicted in Fig. 4.20, is reported to reach a theoretical specific capacity of 117.6 mAh/g.

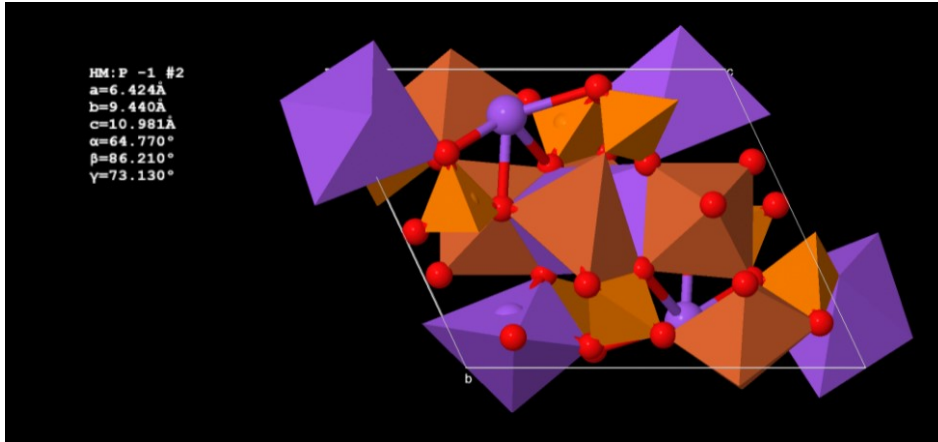


Figure 4.20 - Model of crystalline arrangement of $\text{Na}_{3.12}\text{Fe}_{2.44}(\text{P}_2\text{O}_7)_2$, with P_2O_7 tetrahedra (light orange), FeO_6 octahedra (dark orange) and Na atoms (purple) linked to oxygen atoms (red)
(Source: ICSD database)

Experiment	$\text{Na}_3\text{Fe}_2(\text{PO}_4)_3$ phase [%wt.]	$\text{Na}_7\text{Fe}_3(\text{P}_2\text{O}_7)_4$ phase [%wt.]	$\text{Na}_{3.12}\text{Fe}_{2.44}(\text{P}_2\text{O}_7)_2$ phase [%wt.]	Amorphous phases [%wt.]
$T_{\text{sintering}} = 500\text{ }^\circ\text{C}$	28.07	29.40	3.10	39.43
$T_{\text{sintering}} = 520\text{ }^\circ\text{C}$	26.25	41.92	7.36	24.48

Table 4.7 - Percentages in weight of crystalline and amorphous phases in glass-ceramics sintered in Varigon atmosphere, at 500 °C and 520 °C, with soaking time of 60 minutes
(Source: IKTS)

Clearly, the weight percentage of amorphous phases is still considerable, but not as high as in previous experiments (550 °C held for 15 minutes, in air and Varigon conditions); this aspect demonstrates that changing the heating parameters can positively influence the crystallization process, and it is particularly evident for sintering at 520 °C (temperature closed to the first crystallization peak).

As already mentioned, it is important that the formed crystalline frameworks are also characterised by $\text{Na}_{3.12}\text{Fe}_{2.44}(\text{P}_2\text{O}_7)_2$, because contributing to increase the Fe^{2+} percentage and the ratio $\text{Fe}^{2+}/\text{Fe}^{3+}$, fundamental for the production of the new active cathode material, with similar structure to $\text{Na}_2\text{FeP}_2\text{O}_7$.

Nevertheless, data from Table 4.7 and Table 4.8 (inherent to the iron content in the whole sintered structure) show that the quantity of reduced iron is still limited in both experiments, suggesting that an additional effort has to be put into the investigation of suitable sintering parameters.

Always hypothesizing a quantity of 1 g of sintered material, the total moles of Fe^{3+} are constantly higher than moles of Fe^{2+} . Ratios $\text{Fe}^{2+}/\text{Fe}^{3+}$ prove that between the two tests, the one at 520 °C is the better for forming crystalline phases (as detected from the weight percentage of amorphous material in Table 4.7) and the closer method to detect the desired active material structure, because containing a higher quantity of triclinic phase (therefore higher percentage of reduced iron) with respect to sintering procedure at 500 °C.

Experiment	Crystalline Phases [type]	Crystalline Phases [moles]	Fe^{3+} [moles]	Fe^{2+} [moles]	$\text{Fe}^{2+}/\text{Fe}^{3+}$
$T_{\text{sintering}} = 500\text{ °C}$	$\text{Na}_3\text{Fe}_2(\text{PO}_4)_3$	0.060	0.121	–	0.066
	$\text{Na}_7\text{Fe}_3(\text{P}_2\text{O}_7)_4$	0.029	0.086	–	
	$\text{Na}_{3.12}\text{Fe}_{2.44}(\text{P}_2\text{O}_7)_2$	0.006	–	0.014	
$T_{\text{sintering}} = 520\text{ °C}$	$\text{Na}_3\text{Fe}_2(\text{PO}_4)_3$	0.056	0.113	–	0.137
	$\text{Na}_7\text{Fe}_3(\text{P}_2\text{O}_7)_4$	0.041	0.123	–	
	$\text{Na}_{3.12}\text{Fe}_{2.44}(\text{P}_2\text{O}_7)_2$	0.013	–	0.032	

Table 4.8 - Moles of crystalline phases and iron content for 1 g of glass-ceramic material, sintered in Varigon atmosphere at 500 °C and 520 °C (Source: IKTS)

The FESEM and EDX analyses have been performed on structure sintered at 500 °C: it appears as a well densified framework, interrupted by some dark spots possibly referable to some pores (Fig. 4.21). The visible crystalline shape is similar to the crystalline structure of Fig. 4.17 (experiment at 550 °C and holding time of 15 minutes), because mainly constituted by the same phases (monoclinic $\text{Na}_7\text{Fe}_3(\text{P}_2\text{O}_7)_4$ and NaSICON $\text{Na}_3\text{Fe}_2(\text{PO}_4)_3$).

The EDX spectra are not reported, because comparable to the ones of Varigon experiment at 550 °C: this aspect is an additional proof of the presence of quite same crystalline phases, in analogous weight percentages (in fact, the summed contribution of $\text{Na}_3\text{Fe}_2(\text{PO}_4)_3$ and $\text{Na}_7\text{Fe}_3(\text{P}_2\text{O}_7)_4$ is roughly the same for the two experiments).

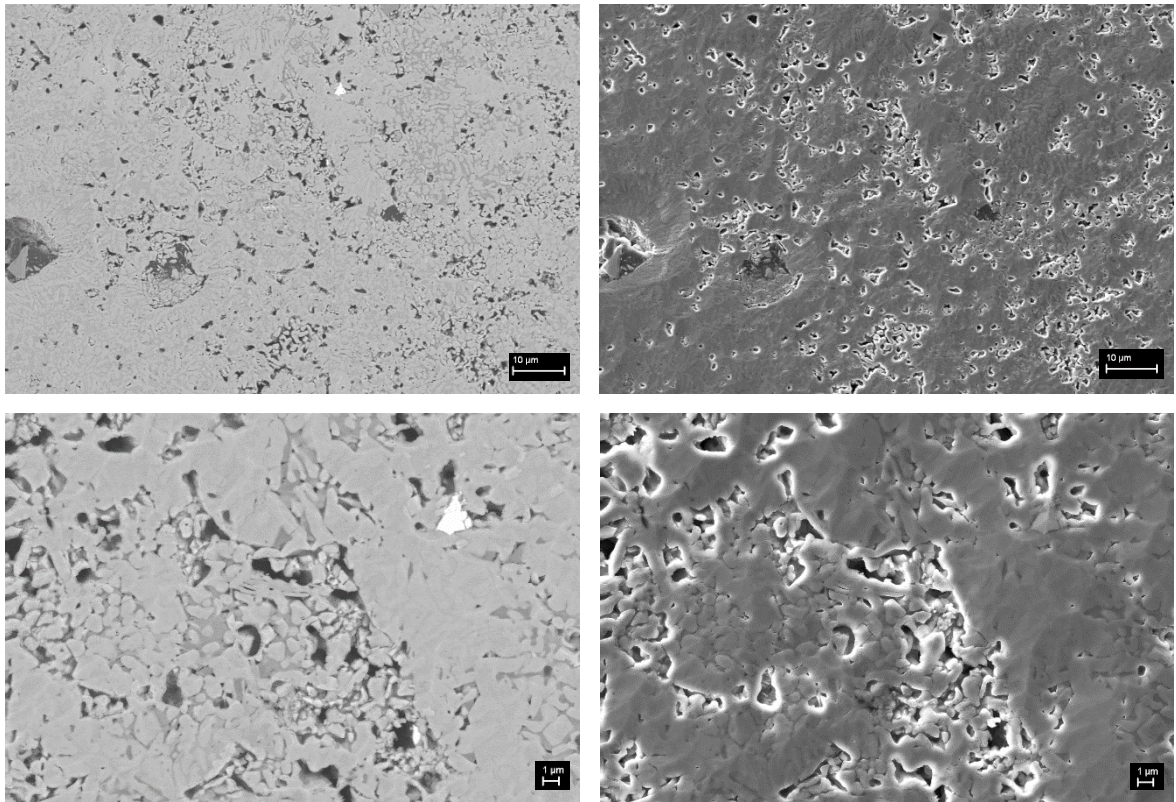


Figure 4.21 - FESEM images of sintered structure at 500 °C in Varigon atmosphere: on the left, figures obtained from detection of Back-Scattered Electrons, on the right of Secondary-Electrons (Source: IKTS)

The next investigation on sintering parameters has been made following the studies from Literature [3,18]: the NFP glass tablets have been submitted to heating at 5 K/min, up to 560 °C with dwelling time of 3 hours.

The chosen sintering temperature is closed to 550 °C, hence at a point for which crystallization is expected to be completed (detectable from the DTA curve). Basing on the test at 550 °C, it is foreseen that the new structure will be characterised by the same main crystalline phases ($\text{Na}_3\text{Fe}_2(\text{PO}_4)_3$ and $\text{Na}_7\text{Fe}_3(\text{P}_2\text{O}_7)_4$); moreover, the increase of soaking time should enhance the crystallization, resulting in a higher percentage of crystalline phases and a reduced amount of unknown amorphous phases.

In the mentioned publications [3,18], the samples to be sintered are made of glass powders and reducing carbon agent (citric acid), helpful to promote the iron reduction during heating and the formation of those crystalline phases identifying the active cathode material. Since the following experiment employs the bare sodium-iron-phosphate

material, it is imagined that not having an additional reduction agent will lead to a scarcer presence of crystalline phases with Fe^{2+} .

As usual, the densification of sintered tablets has been measured: starting from an average density of $1.97 \pm 0.01 \text{ g/cm}^3$, the material shrinks during the heating process, reaching the value of $2.62 \pm 0.01 \text{ g/cm}^3$ after sintering.

The main detected phases, as forecasted, are the NaSICON crystalline phase $\text{Na}_3\text{Fe}_2(\text{PO}_4)_3$ and the monoclinic pyrophosphate $\text{Na}_7\text{Fe}_3(\text{P}_2\text{O}_7)_4$: the diffracted spectrum, obtained from XRD analysis, is depicted in Fig. 4.22 with the characteristic peaks of the two phases. The unique presence of these phases proves the expectations: even if conducted in reducing atmosphere, a sintering procedure without reducing agent is not likely to form structures with iron in reduced form or, if some Fe^{2+} is present, anyway it is not in sufficient quantities.

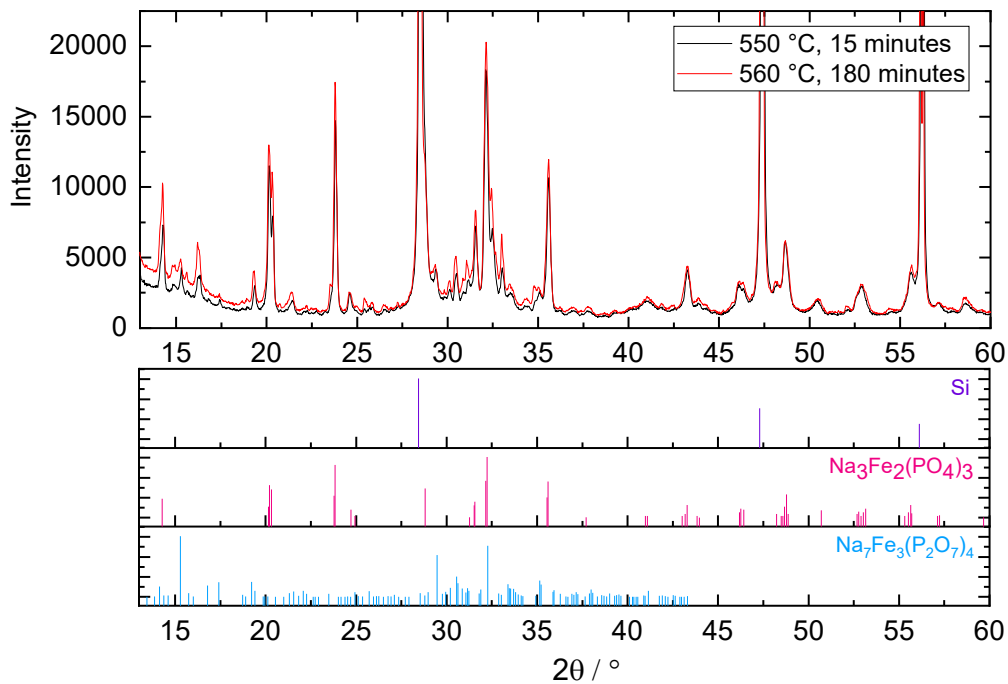


Figure 4.22 - Comparison of diffraction paths generated by XRD analysis on sintered tablets in Varigon, at 550 °C with soaking time of 15 minutes (in black), at 560 °C with soaking time of 180 minutes (in red), with responsible crystalline phases (Source: IKTS)

Nonetheless, the diffraction path of experiment at 560 °C, held for 180 minutes, presents slightly higher-intensity-peaks with respect to the test performed at 550 °C, held for 15 minutes: it seems, as imagined, that the longer the soaking time, the better defined will be the new crystalline framework.

The deduction is confirmed if the weight percentages are calculated with the software DIFFRAC.SUITE TOPAS (Table 4.9): the crystalline phases constitute almost the 81 %wt., and the remaining small weight percentage is referred to amorphous phases.

Experiment	Na ₃ Fe ₂ (PO ₄) ₃ phase [%wt.]	Na ₇ Fe ₃ (P ₂ O ₇) ₄ phase [%wt.]	NaFe ₃ P ₃ O ₁₂ phase [%wt.]	Amorphous phases [%wt.]
<i>T_{sintering} = 550 °C, 15 min.</i>	19.37	36.73	3.25	40.65
<i>T_{sintering} = 560 °C, 180 min.</i>	26.09	54.78	–	19.13

Table 4.9 – Percentages in weight of crystalline and amorphous phases in glass-ceramics sintered in Varigon atmosphere; comparison between sintering procedure at 550 °C with soaking time of 15 minutes, and sintering procedure at 560 °C with soaking time of 180 minutes (Source: IKTS)

The absence of iron in reduced form is reported in Table 4.10 below.

Crystalline Phases [type]	Crystalline Phases [moles]	Fe ³⁺ [moles]	Fe ²⁺ [moles]
Na ₃ Fe ₂ (PO ₄) ₃	0.056	0.112	–
Na ₇ Fe ₃ (P ₂ O ₇) ₄	0.053	0.160	–

Table 4.10 - Moles of crystalline phases and iron content for 1 g of glass-ceramic material, sintered in Varigon atmosphere at 560 °C (Source: IKTS)

The sintered tablets, as the others treated in Varigon, have highly densified structure and compact form, with few pores (the calculated porosity percentage is 5.5 % ± 0.6). As showed in Fig. 4.23 (especially for images in the bottom, with higher magnification), the framework is composed by uniform and repeated grains, of shape comparable to the one of sintered material in Varigon at 550 °C (Fig. 4.17).

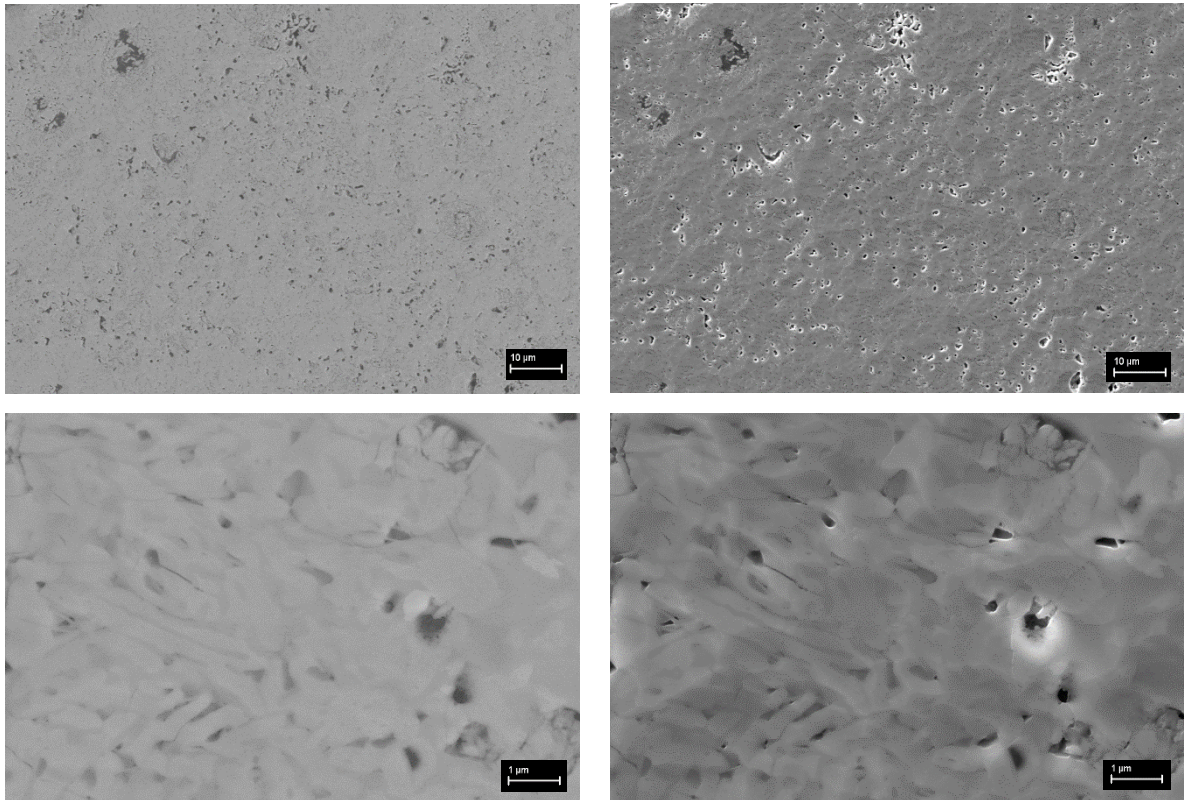


Figure 4.23 - FESEM images of sintered structure at 560 °C in Varigon atmosphere: on the left, figures obtained from detection of Back-Scattered Electrons, on the right of Secondary-Electrons (Source: IKTS)

The variation of temperature and soaking time are useful features to be considered for the realization of a proper cathode material.

The sintering experiments at 500 °C and 520 °C, held for 60 minutes, show the presence of triclinic crystalline phase $\text{Na}_{3.12}\text{Fe}_{2.44}(\text{P}_2\text{O}_7)_2$, exclusively formed by iron Fe^{2+} . Moreover, the increase of holding time improves the crystallization and reduces the residual amorphous phases. Nonetheless, the procedure is far to be the ideal one, due to the small percentage of triclinic phase, hence to the limited $\text{Fe}^{2+}/\text{Fe}^{3+}$ ratio in the structure. The sintering process at 560 °C, with holding time of 3 hours, enhances even more the crystallization, leading to small percentages of amorphous phases. The crystalline pattern by XRD analysis is comparable to the one of previous experiment (at 550 °C for 15 minutes), reporting the same main crystalline phases, with only iron in oxidized form.

In conclusion, it results that the goals of the investigation can be achieved by heating in reducing atmosphere (Varigon), with sufficiently high soaking time, at a temperature suitable for a nearly complete crystallization (hence, at around 550-560 °C). The addition of a carbon agent would be fundamental for the enhancement of reduction process during sintering and for increasing the electronic conductivity of the batch.

4.4 Influence of carbon conducting agent

The following investigations regard the citric acid and graphite addition to the glassy batch, with the purpose of promoting the reducing effect ($\text{Fe}^{3+} \rightarrow \text{Fe}^{2+}$) during sintering and forming an electronic conduction path throughout the crystalline framework. As known, the carbon sources are subject to thermal decomposition while heating in absence of oxygen and, being in contact with the NFP structure, they act as reducing agents as well. From those reactions, it is highly probable that some substances are released in heating chamber (H_2O , CO , CO_2 , amorphous carbon): in particular, part of the solid carbon is expected to be deposited in the semi-crystalline structure, increasing the transfer rate of electrons and therefore enhancing the electronic conductivity.

With pyrolysis performed in Varigon conditions, it is forecasted that the double action of reducing atmosphere and carbon agents will promote the iron reduction and the achievement of the active and conducting crystalline structure.

The quantity of reducing carbon material is limited, in order not to hinder the densification of NFP batch: for this reason, the citric acid is fixed to the 10 %wt., as performed in reference studies [3,18], the graphite is varied in the range 3-5 %wt. according to the previous experience of the institute [20].

4.4.1 Addition of citric acid: HSM and Sintering in Varigon

After the mixing in the mechanical blender, the NFP with 10 %wt. of citric acid has been firstly submitted to the HSM analysis, to investigate the structure reaction during heating and the range of temperatures for the batch densification. The graph is reported hereunder in Fig. 4.24, associated to some shadowed pictures of the cylindrical sample in the heating chamber.

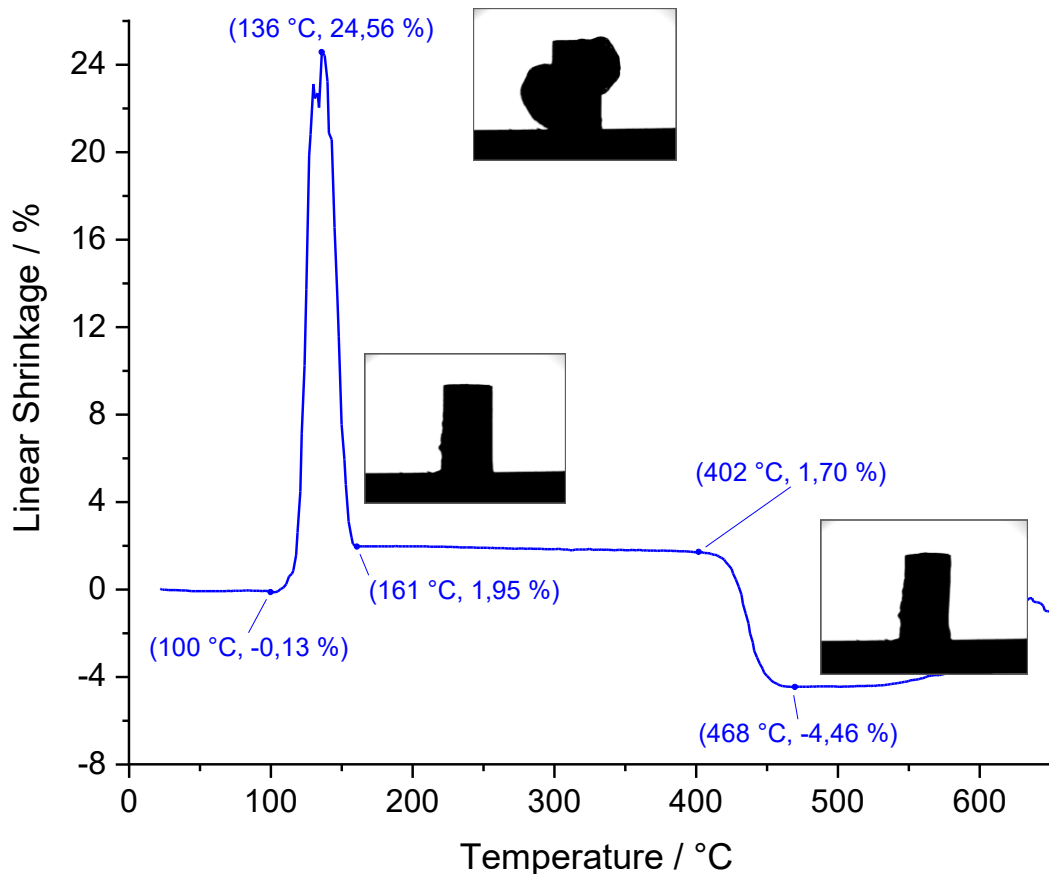


Figure 4.24 - HSM curve for NFP powders mixed with 10 %wt. of $C_6H_8O_7$ and associated pictures of cylindrical sample at precise temperatures; procedure performed heating at 5 K/min, up to 700 °C (Source: IKTS)

The first remarkable aspect is the expansion of sample starting from 100 °C: the cylinder experiences a linear expansion up to the 24.6 %, appearing in form of bubbles and swellings on the lateral surface. The effect could be related to the H_2O desorption from the surface of the sample, strongly enhanced with respect to the case of bare NFP heated in Varigon (HSM curve in Fig. 4.10) because of the hydrogen contained in citric acid. Keeping heating, the sample recovers the original shape and is next subject to volume reduction from 400 °C on. Although the densification occurs in Varigon and in a reasonable window of temperatures, nonetheless it is not so significant: the measured volume reduction in the temperature range 402-468 °C is around 6.2 %, against the linear shrinkage of more than 9 % measured for bare NFP treated in same conditions.

The sintering path is the one already employed for NFP material alone: reduced in tablets form, the mixed glass composition has been heated with rate of 5 K/min to 560 °C and

kept at that temperature for 3 hours. As predicted, the as-sintered samples show signs of expansion and instability while heating, with non-uniform structure and colours (Fig. 4.25). The tablets are scarcely cohesive and with visible holes, due to the probable reactions during heating and emission of gaseous H_2O , CO_2 and CO . The geometry and density have not been calculated, due to the lack of integrity of tablets.



Figure 4.25 – Sample of NFP material mixed with 10 %wt. of citric acid, sintered at 5 K/min to 560 °C, held for 3 hours, in Varigon atmosphere; here, laying on BN substrate

The crystalline pattern obtained with XRD analysis is different from previous investigations: as evident in Fig. 4.26, the Bragg peaks are in higher number, especially for diffraction angles in the range 15° - 35° , demonstrating the occurring of better crystallization during sintering. The main responsible for diffracted peaks is the crystalline triclinic pyrophosphate $Na_{3.12}Fe_{2.44}(P_2O_7)_2$: as mentioned before, it is characterised by iron in reduced form (Fe^{2+}), proving that the chosen sintering path, coupled with a carbon reducing agent, is effective for the generation of a triclinic conducting structure.

As expected from reference studies [18], the $Na_4P_2O_7$ phase has been observed for few isolated peaks (in 2θ equal to 20° , 26° , 38° , 59°): it forms due to structure decomposition at high temperature, with higher measured intensity the higher is the treatment temperature. Some maricite $NaFePO_4$ is detected as well, only for few small peaks (for diffraction angles of 19° , 24° , 33° - 34°): although constituted by iron in reduced form, the phosphate is not ideal in a cathode material, since isolating the sodium sites in the framework [11].

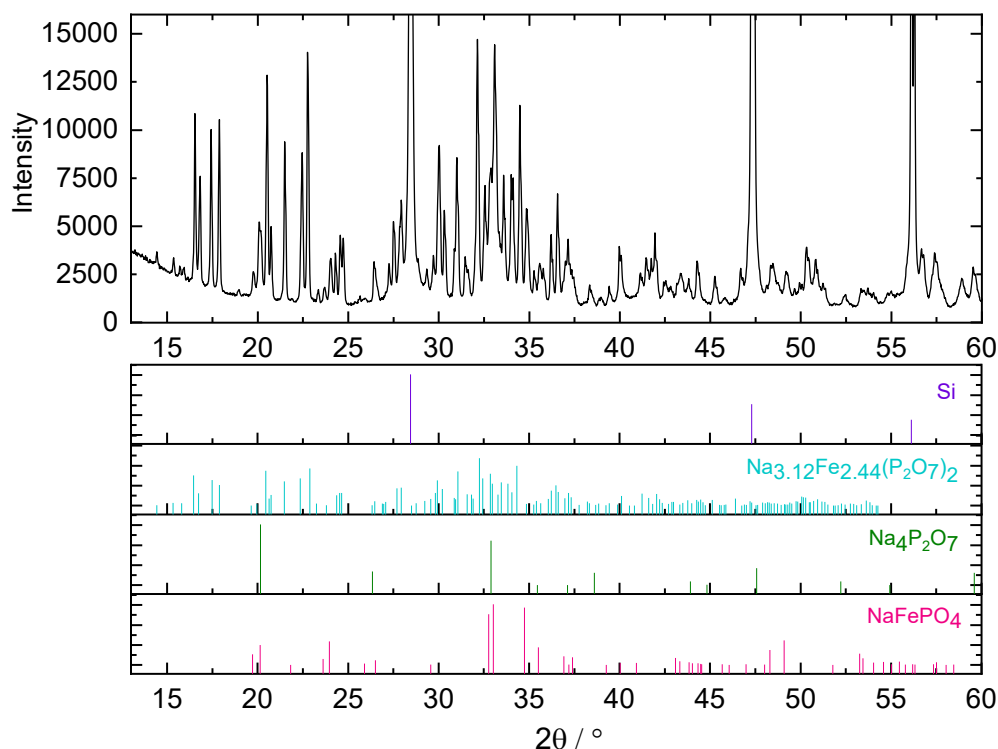


Figure 4.26 - Diffraction path generated by XRD analysis on sintered tablets (90 %wt. NFP - 10 %wt. $C_6H_8O_7$) in Varigon atmosphere, at $T_{sintering}$ of 560 °C, held for 3 hours, with responsible crystalline phases (Source: IKTS)

Due to the several peaks, the diffracted XRD pattern suggests that the sintered structure is prevalently formed by crystalline phases and that the residual amorphous are in small percentage. The impression is confirmed by the DIFFRAC.SUITE TOPAS calculations (Table 4.11), showing that the 76.3 %wt. of the overall structure is crystallized, and only the 23.7 % is still in amorphous and disordered form. As expected, the prevalent phase is the triclinic one, proving the effectiveness of sintering in reducing environment with the addition of a reducing agent; nevertheless, the 11 %wt. is still formed by $NaFePO_4$, which blocks the Na^+ movement due to its inner structure.

Experiment	$Na_{3.12}Fe_{2.44}(P_2O_7)_2$ phase [%wt.]	$Na_4P_2O_7$ phase [%wt.]	$NaFePO_4$ phase [%wt.]	Amorphous phases [%wt.]
10 %wt. citric acid	61.60	3.55	11.11	23.74

Table 4.11 - Percentages in weight of crystalline and amorphous phases in NFP material mixed with citric acid, sintered in Varigon atmosphere, at 560 °C for 3 hours (Source: IKTS)

The calculation of iron content reveals the exclusive presence of Fe^{2+} in the structure: as usual, hypothesizing a quantity of 1 g of material, the calculated moles of iron in reduced form are 0.27 from $\text{Na}_{3.12}\text{Fe}_{2.44}(\text{P}_2\text{O}_7)_2$ and 0.06 from NaFePO_4 .

In conclusion, it is stated that the mixing of NFP glass material with citric acid and its sintering in the defined conditions could be suitable for the production of a good conductive cathode material, as revealed from the iron content and the main triclinic crystalline phase. Despite that, the thermal decomposition during heating and the gaseous emissions expose the samples to high linear expansion at reduced temperatures: this aspect makes the composition not feasible for an integration in a solid state battery and effective charge-discharge characteristics. For that reason, the values of DC resistivity and conductivity have not been calculated.

4.4.2 Addition of graphite: HSM and Sintering in Varigon

Afterwards, the NFP have been blended with graphite, added in 3, 4, 5 %wt., and the densification and sintering behaviour have been investigated. It is predictable that the higher the amount, the better the electronic conductivity and the reducing effect; at the same time, a high quantity of graphite limits more the NFP shrinkage due to the less sinter-active contacts between glass particles, increases the porosity and reduces the mechanical resistance. The proper conductive material to be coupled with the solid electrolyte must be chosen analysing all the various aspects.

The Hot Stage Microscopy, performed as usual at 5 K/min up to 700 °C in Varigon conditions, reports a good densification behaviour for all the samples (Fig. 4.27), demonstrating the expectations: with respect to the NFP powders alone, the linear shrinkage is progressively reduced the more the graphite added to the batch. In any case, the added amount is reasonable and does not significantly hinder the volume reduction (9.2 % for mixing with 3 %wt., 8.75 % with 4 %wt., 8.39 % with 5 %wt.).

The Thermogravimetric Mass Spectrometry has been applied to some NFP powders mixed with 5 %wt. of graphite, heating in reducing atmosphere (95 vol.% N₂ - 5 vol.% H₂). As in the previous cases, the aim is the investigation of the effect of reducing gas atmosphere and carbon addition in the generation of H₂O, CO₂, C and O₂ particles while heating. Having some graphite in the batch, it is presumed to detect higher levels of carbon dioxide and solid carbon; moreover, the quantity of generated oxygen is expected to still be small, as proof of a good reducing sintering environment.

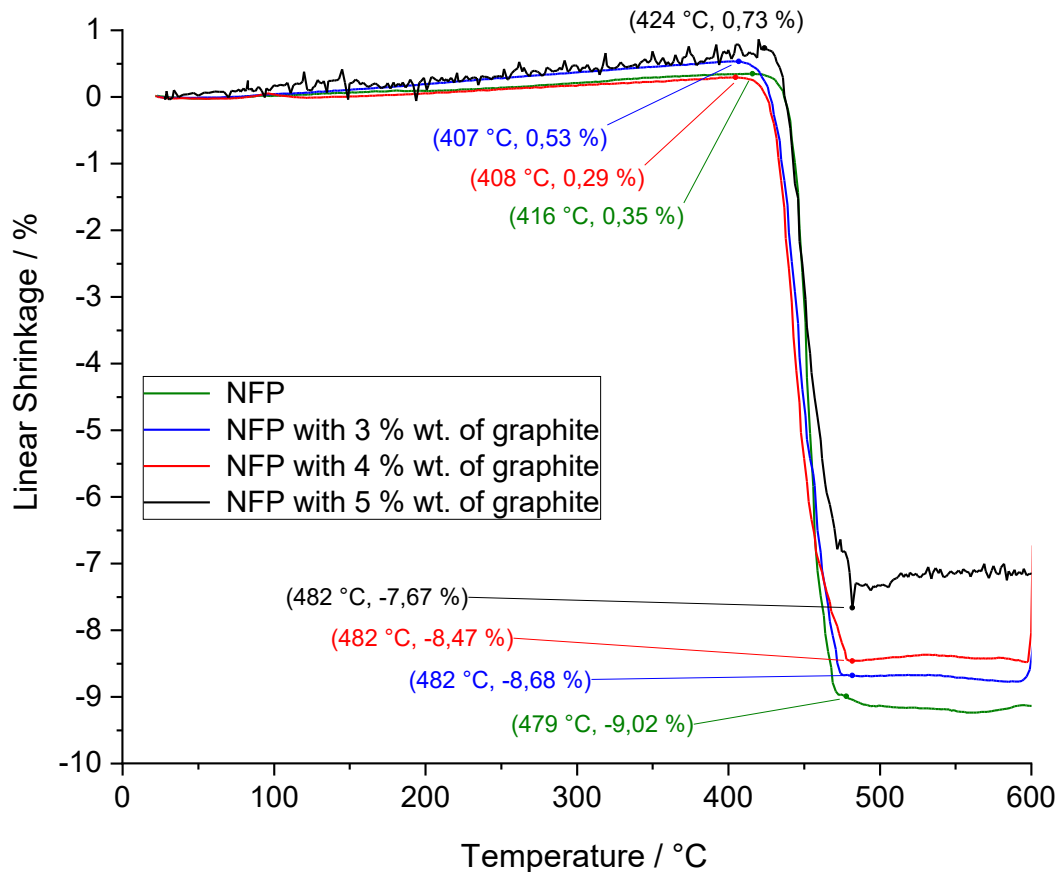


Figure 4.27 - HSM curves for NFP and NFP mixed with 3-4-5 %wt. of graphite, heating in Varigon at 5 K/min, up to 700 °C (Source: IKTS)

The TGMS graphs, comparing the heating processes for NFP and NFP-graphite, are depicted in Fig. 4.28. Clearly, the presence of carbon in the glass-ceramic structure promotes the thermal decomposition and the emission of higher quantity of CO₂ and C (at 624 °C, the MS signals are 4.7·10⁻¹⁵ A/mg and 3.5·10⁻¹⁶ A/mg, respectively). The H₂O emission is more intensive with the addition of carbon source (black curve): product of reduction reaction between NFP-graphite composite and H₂ in the atmosphere, it seems to be the dominant reaction for the reduction of the material. Moreover, it is important to notice that the reduction effect occurs at lower temperatures with respect to the case of bare NFP treated in same atmosphere.

Lastly, also the plot related to oxygen ions presents a growing trend for high temperatures, since deriving from water and carbon dioxide molecules; again, the measured values prove the effectiveness of carbon addition for the reduction reaction, suggesting that those conditions would be effective for the production of active composite electrode.

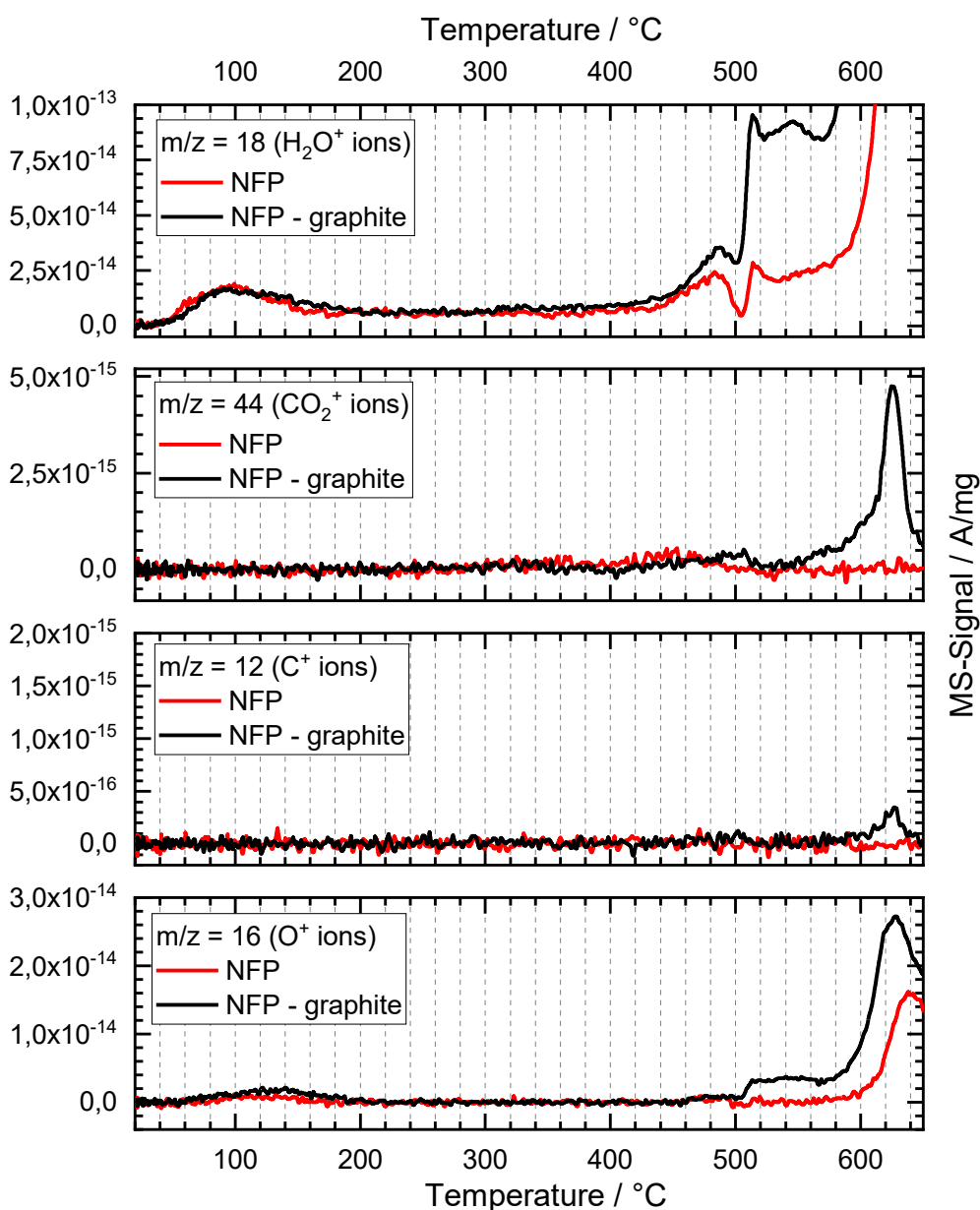


Figure 4.28 - Comparison of plots from TGMS analysis on NFP and NFP mixed with 5 %wt. of graphite, heated at 5 K/min up to 800 °C in reducing atmosphere (Source: IKTS)

The sintering path is the same employed in the case of mixing with citric acid (heating rate of 5 K/min in Varigon, maximum temperature of 560 °C and holding time of 3 hours). After sintering, the density values have been calculated basing on the mass and the geometry of tablets (Table 4.12): again, the density is higher for samples with higher quantity of densifying material (NFP).

Experiment	Density Before Sintering ρ [g/cm ³]	Density After Sintering ρ [g/cm ³]
NFP	1.97 ± 0.01	2.62 ± 0.01
NFP with 3 %wt. graphite KS15	1.94 ± 0.01	2.38 ± 0.01
NFP with 4 %wt. graphite KS15	1.95 ± 0.01	2.18 ± 0.01
NFP with 5 %wt. graphite KS15	1.94 ± 0.01	2.16 ± 0.01

Table 4.12 - Calculated density values, before and after sintering procedure, for NFP and NFP samples mixed with 3-4-5 %wt. of graphite, treated in Varigon conditions (Source: IKTS)

The formed crystalline phases are detected with the spectrum derived from XRD analysis (Fig. 4.29), which shows a diffracted pattern comparable to the one of sintering with citric acid. The crystalline peaks related to the three experiments are almost the same, slightly varying in intensity: it is deducible that they are associated to the same phases, with different contribution according to the quantity of graphite added. The amorphous and crystalline content is expressed in terms of weight percentage in the following page (Table 4.13).

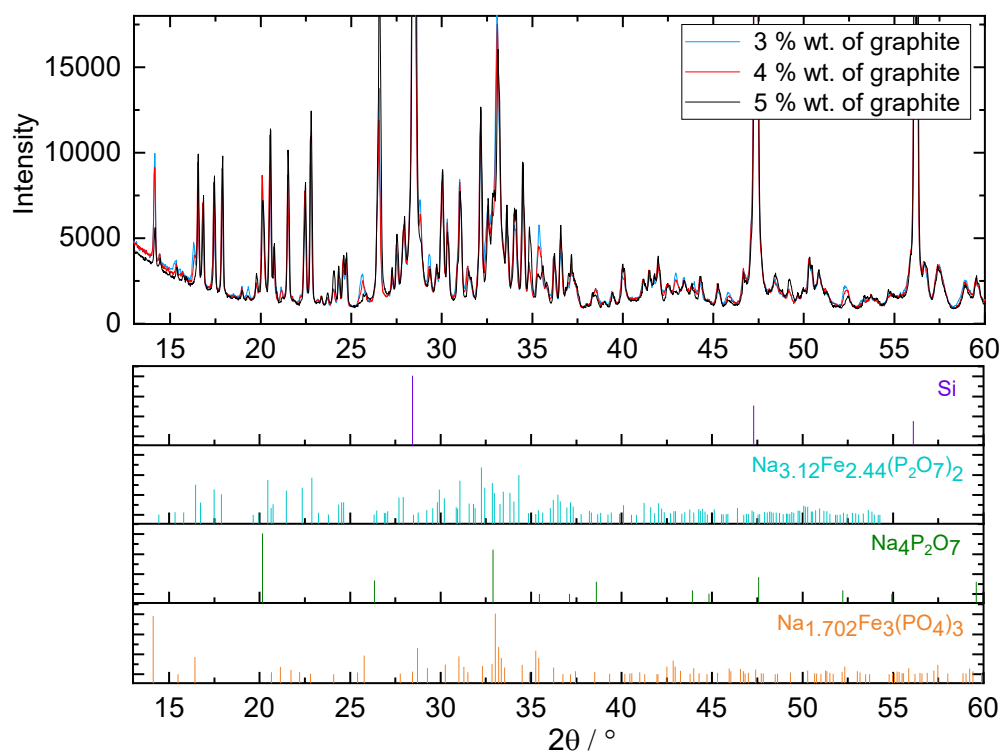


Figure 4.29 - Diffraction path generated by XRD analysis on sintered tablets (NFP mixed with 3-4-5 %wt. of graphite) in Varigon atmosphere, at $T_{\text{sintering}}$ of 560 °C, with responsible crystalline phases (Source: IKTS)

The triclinic $\text{Na}_{3.12}\text{Fe}_{2.44}(\text{P}_2\text{O}_7)_2$ is still the prevailing phase, demonstrating that the properly conductive cathode material can be obtained by combining the reducing effect of Varigon atmosphere and mixing with carbon sources. The $\text{Na}_4\text{P}_2\text{O}_7$ phase, related to thermal decomposition at high temperatures, is detected for reduced-intensity peaks (as at $2\theta = 20^\circ, 26^\circ, 38^\circ$). Moreover, the other identified crystalline phase is $\text{Na}_{1.702}\text{Fe}_3(\text{PO}_4)_3$, behaving to the Alluaudites family as $\text{NaFe}_3\text{P}_3\text{O}_{12}$. As the other phosphates, its monoclinic crystalline framework is composed by corners-sharing PO_4 tetrahedra and FeO_6 octahedra, spaced out by Na atoms, forming octahedra and trigonal prisms with oxygen atoms. An example of the crystalline structure is depicted in Fig. 4.30.

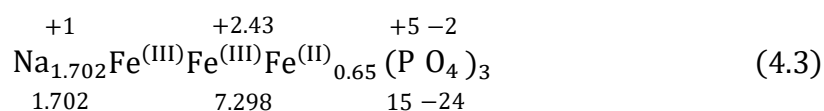
The peak of significant intensity detected at 26.5° , not associable to any crystalline phase, is probably related to the cumulation of some amorphous carbon in the structure.

The amorphous content is still relevant for all the experiments, varying in the range 30-40 %wt..

Experiment	$\text{Na}_{3.12}\text{Fe}_{2.44}(\text{P}_2\text{O}_7)_2$ phase [%wt.]	$\text{Na}_4\text{P}_2\text{O}_7$ phase [%wt.]	$\text{Na}_{1.702}\text{Fe}_3(\text{PO}_4)_3$ phase [%wt.]	Amorphous phases [%wt.]
3 %wt. graphite KS15	38.36	10.05	13.73	37.87
4 %wt. graphite KS15	46.17	9.81	11.23	32.79
5 %wt. graphite KS15	44.35	9.15	5.99	40.51

Table 4.13 - Percentages in weight of crystalline and amorphous phases for NFP material mixed with 3-4-5 %wt. of graphite, sintered in Varigon atmosphere, at 560 °C for 3 hours (Source: IKTS)

The monoclinic Alluaudite contains partially reduced iron (oxidation number of Fe equal to 2.43), as demonstrated from the following calculation (Eq. 4.3):



Hence, the combination of triclinic $\text{Na}_{3.12}\text{Fe}_{2.44}(\text{P}_2\text{O}_7)_2$ and monoclinic $\text{Na}_{1.702}\text{Fe}_3(\text{PO}_4)_3$ should guarantee the formation of a crystalline structure with iron mainly in reduced form, optimal to be employed as an electronic and ionic conductive material.

From a first evaluation, it seems that NFP mixed with 4 %wt. of graphite is the ideal combination, because defined by the smaller amorphous content (32.8 %wt.) and the higher content of crystalline phases with Fe^{2+} (57.4 %wt. of triclinic and monoclinic phase).

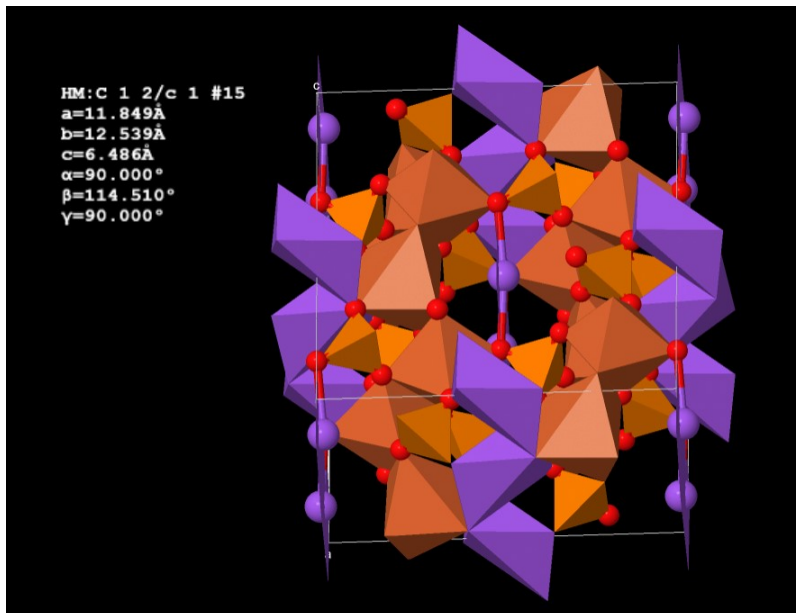


Figure 4.30 - Model of crystalline arrangement of $\text{Na}_{1.702}\text{Fe}_3(\text{PO}_4)_3$, with PO_4 tetrahedra (light orange), FeO_6 octahedra (dark orange) and Na atoms (purple) linked to oxygen atoms (red)
(Source: ICSD database)

The appropriate mix to be coupled with solid electrolyte has been also chosen analysing the DC conductivity values and the iron content.

The electronic resistance, measured via gold sputtering before and silver paste coating after, results to be around 430 k Ω for NFP mixed with 3 %wt. of graphite, 245 k Ω for the addition of 4 %wt. of graphite, 0.125 k Ω for blending with the 5 %wt. of graphite. Clearly, the higher the carbon content, the lower the resistance: this aspect is confirmed by the strong distinction between the third and the other cases, suggesting that the 5 %wt. should be the proper quantity to be added to have a good electronic movement. Indeed, the calculated DC conductivity is $3.6 \cdot 10^{-7}$ S/cm, $6.5 \cdot 10^{-7}$ S/cm and $1.2 \cdot 10^{-3}$ S/cm respectively. If compared with the DC conductivity measured for bare NFP treated in same heating conditions ($2.1 \cdot 10^{-6}$ S/cm), it is clear that the composition 95 %wt. NFP - 5 %wt. graphite is the best in terms of electronic performance.

The values concerning the iron content are reported hereunder in Table 4.14.

Experiment	Crystalline Phases [type]	Crystalline Phases [moles]	Fe ³⁺ [moles]	Fe ²⁺ [moles]	Fe ²⁺ /Fe ³⁺
3 %wt. graphite KS15	Na_{3.12}Fe_{2.44}(P₂O₇)₂	0.069	–	0.168	3.340
	Na₄P₂O₇	0.038	–	–	
	Na_{1.702}Fe₃(PO₄)₃	0.028	0.056	0.018	
4 %wt. graphite KS15	Na_{3.12}Fe_{2.44}(P₂O₇)₂	0.083	–	0.203	4.761
	Na₄P₂O₇	0.037	–	–	
	Na_{1.702}Fe₃(PO₄)₃	0.023	0.046	0.015	
5 %wt. graphite KS15	Na_{3.12}Fe_{2.44}(P₂O₇)₂	0.080	–	0.195	8.315
	Na₄P₂O₇	0.034	–	–	
	Na_{1.702}Fe₃(PO₄)₃	0.012	0.024	0.008	

Table 4.14 - Moles of crystalline phases and iron content (Fe³⁺ and Fe²⁺) for 1 g of glass-ceramic material, mixed with 3-4-5 %wt. of graphite and sintered in Varigon atmosphere at 560 °C for 3 hours (Source: IKTS)

As visible, the NFP composite with 5 %wt. of graphite is the one with greater Fe²⁺ content over Fe³⁺, hence the more promising in terms of electrochemical efficiency if coupled with a solid electrolyte.

In the next pages are reported some FESEM images: the pictures of microscopic structures satisfy the expectations, presenting highly densified glass-ceramic particles, alternated to graphite clusters. The laminar structure of graphite, lighter than the other elements, is shown in dark colour and is clearly distinguishable from the rest of densified crystals (Fig. 4.31). The average porosity percentage, measured for NFP mixed with 5 %wt. of graphite, is 7% ±1.9: the small porosity value is an ulterior proof of the excellent densification occurred.

The graphite percolation is also visible in Fig. 4.32, reporting a comparison between structures with 4 %wt. and 5 %wt.: as clearly noticeable, the framework with higher graphite content guarantees further paths for conduction of electrons.

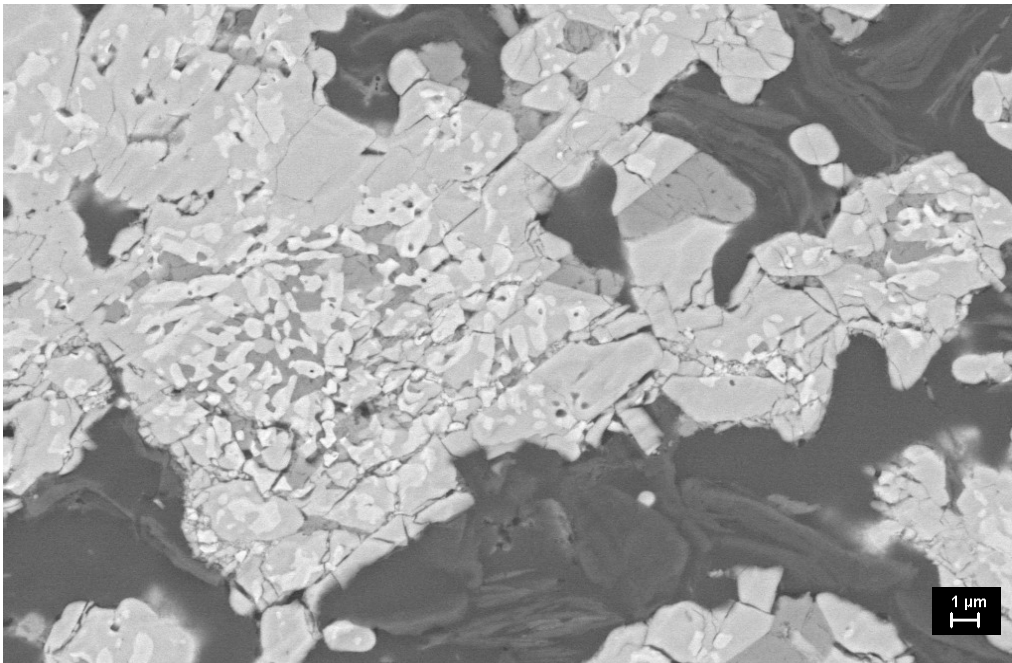
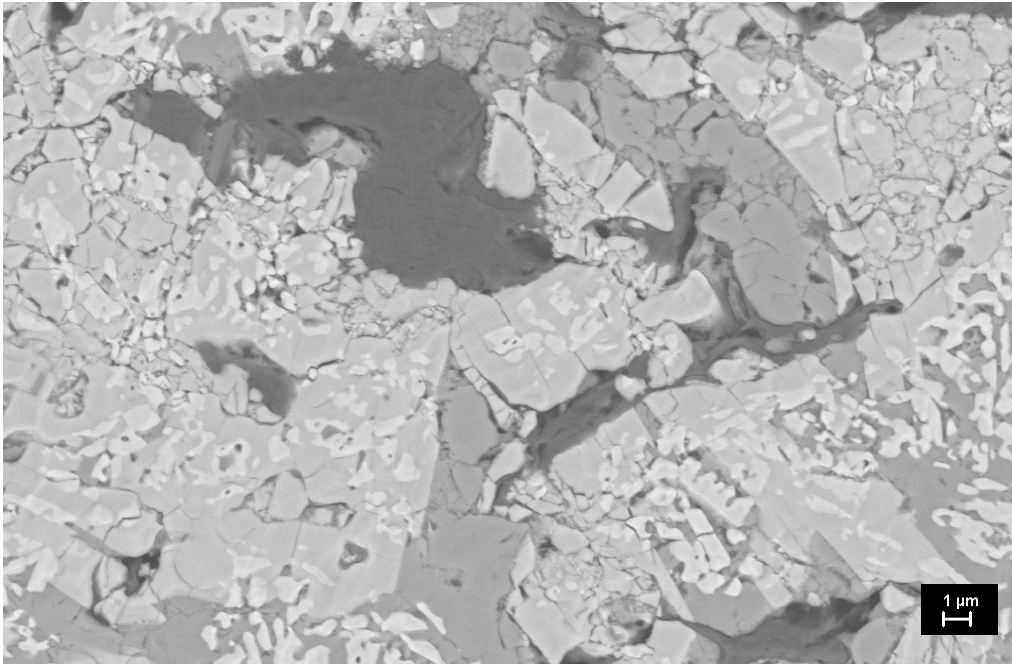


Figure 4.31 - FESEM image of sintered structure, for NFP material mixed with 4 %wt. of graphite (top image) and with 5 %wt. of graphite (bottom image)
(Source: IKTS)

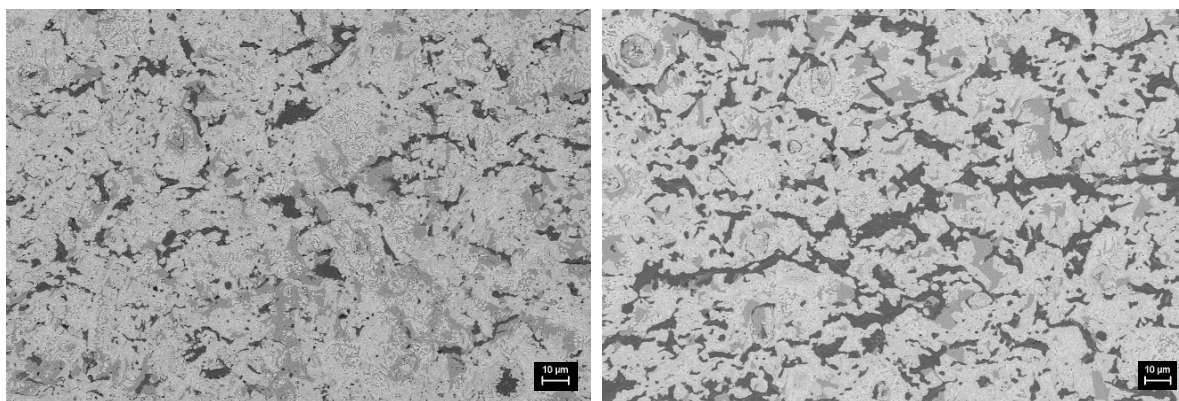
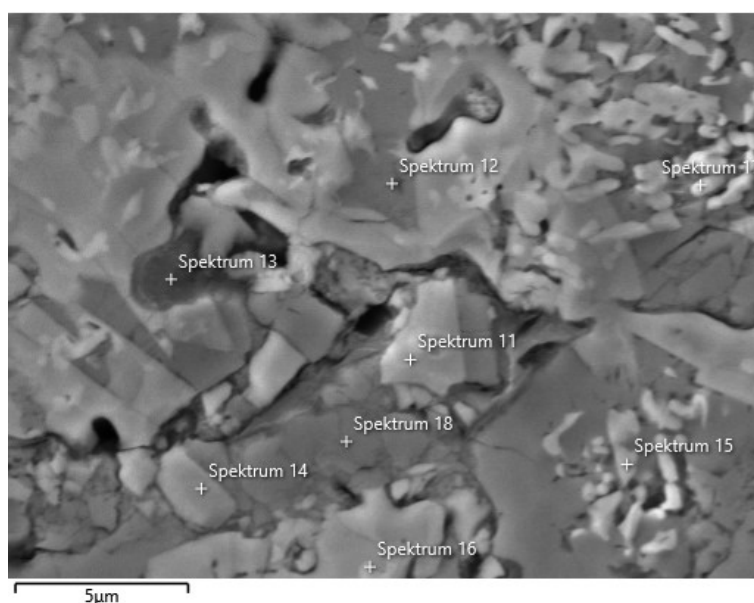
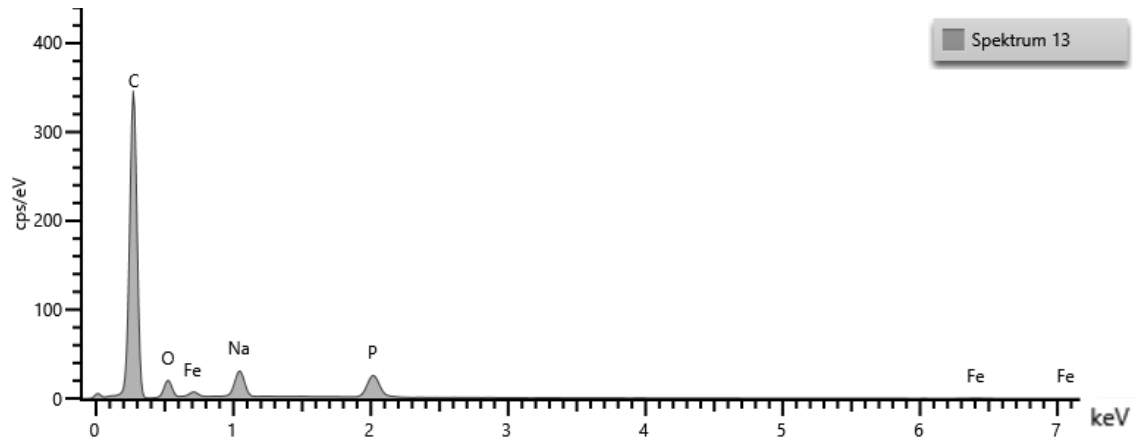
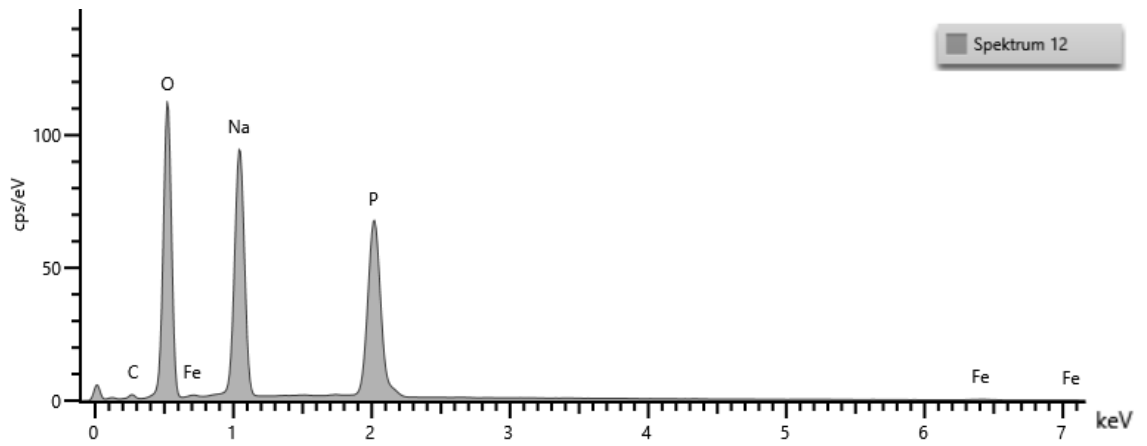
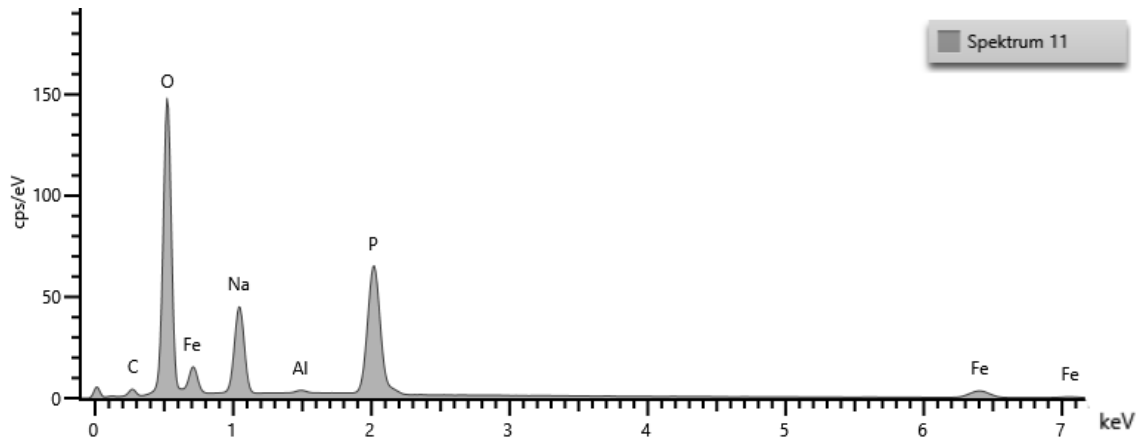


Figure 4.32 – Comparison of FESEM images for NFP mixed with 4 %wt. (left) and 5 %wt. of graphite (right) (Source: IKTS)

The EDX spectra, reported in association with a FESEM picture (Fig. 4.33), delineate several important points: as forecasted, the light spots (n. 11) are characterised by smaller content of Na and higher of O₂, in opposition to darker sections (n. 12). Points as n. 13 show a prevalent amount of carbon, because of graphite deposition; moreover, the spot n. 18 is possibly associable to the crystalline phase Na₄P₂O₇, because of the absence of Fe element in the detected spectrum.





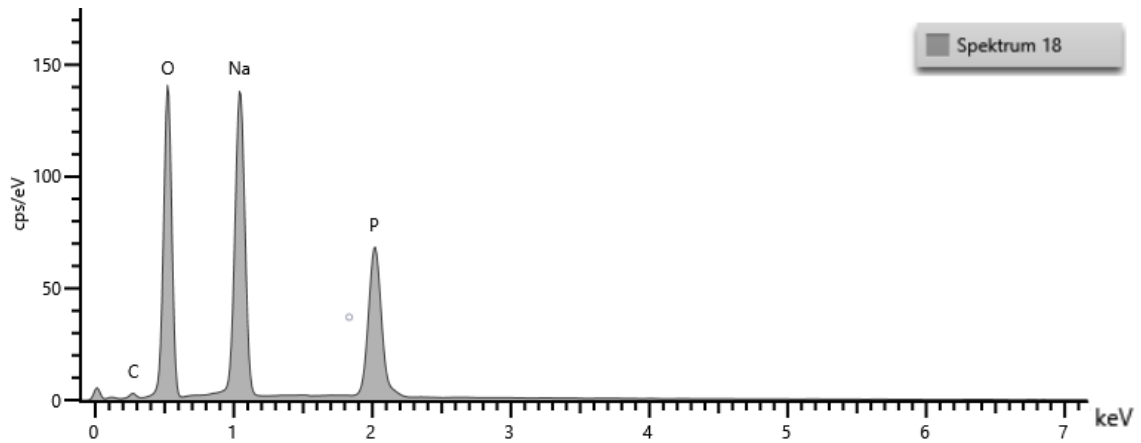


Figure 4.33 - FESEM image, associated to EDX spectra related to different points in the crystalline structure (Source: IKTS)

In the end, the material to be sintered on the solid electrolyte for electrochemical investigation is the sodium-iron-phosphate mixed with 5 %wt. of graphite. The composition shows a sufficiently relevant densification during heating, good electrical conductivity and proper crystalline phases, due to the reducing effect of sintering atmosphere, combined with the employment of a carbon reducing agent in the sintered batch. The framework is mainly formed by iron in reduced form, as noted in $\text{Fe}^{2+}/\text{Fe}^{3+}$ ratio calculations, which for the material under investigation is equal to 8.315. Finally, the FESEM and EDX images confirm a well densified and crystallized microstructure, with several conducting paths for electronic conductivity.

4.5 Electrochemical characterization of solid electrolytes and half-cell composites

Concluded the investigation on the NFP material and the optimal sintering procedure for a suitable cathode element, it is appropriate to characterize the solid electrolyte composition. As anticipated, the subjects of examination have been the glass-ceramic Na07 and the NaSICON-type solid electrolyte powders, pressed in form of disks. The Electrochemical Impedance Spectroscopy analysis has been applied to verify the ionic conductivity of bulk materials and to measure the resistance to the ions movement at the interface with metallic sodium and with the candidate cathode material. Previous investigations from the institute report ionic conductivity values in the range 10^{-4} - 10^{-3} S/cm (25 °C) for Na07, 10^{-3} S/cm (25 °C) for NaSICON electrolyte.

The conductivity and the interface resistance of solid electrolytes in contact with metallic sodium has been measured by stacking the electrolytes in a symmetrical arrangement with Na and graphite foils, pressing the layers at T_{amb} and 50 °C and performing EIS analysis with EI-cells.

An example of collected data, elaborated with the software RelaxIS, is depicted in the Nyquist plot hereunder (Fig. 4.34). The dots, indicating impedance values for the different frequencies applied, follow the shape of two depressed semicircles: the smaller one, for high frequencies, is related to lower impedance phenomena, typical of the electrolyte material; the bigger one, for reduced frequencies, reports higher impedance values and is due to the electrochemical effects through the interface. The fitting of collected points is realized by defining an equivalent electrical circuit, formed by R|CPE circuits disposed in series. In this case, the circuits in series were four, corresponding to the dashed curves represented in image. One circuit represents the impedance effects across the electrolyte grain boundaries (n.2, indicated with the dashed blue curve) and an additional (n.1, with dashed red curve) indicates the impedance in the bulk (in fact, the graph does not start from origin of axes, showing the presence of a small resistance in the electrolyte material). Concerning the other two circuits (n.3,4), they are related to the impedance through the interface, assumed equal for both electrolyte sides facing Na layers: hence, they are indicated with a single curve (dashed green curve).

From the intersection of fitting dashed curves with the horizontal axis, the resistance values have been collected and grouped in two categories: the $R_{\text{electrolyte}}$, sum of resistance to ionic movement in the electrolyte material (resistance of equivalent circuit n.1) and across its grain boundaries (resistance of equivalent circuit n.2), and the $R_{\text{interface}}$, sum of the two resistances encountered in the evaluation of the big part of impedance curve (from equivalent circuits n.3,4).

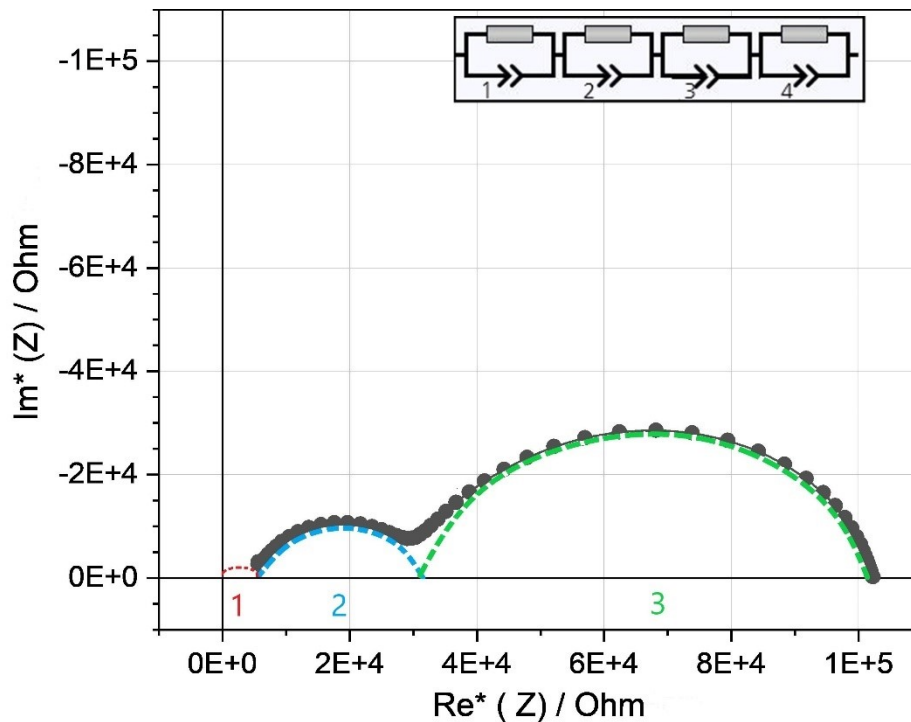


Figure 4.34 – Example of Nyquist plot for symmetrical stack, here with NaSICON-type solid electrolyte, associated with equivalent electrical circuit (Source: IKTS)

The measured impedance values, corrected by the dimensions of the samples, have been represented with temperature variation in the Nyquist plot (Fig. 4.35): as predicted, the higher the temperature, the lower the resistance and capacitance values, hence the narrower the curves.

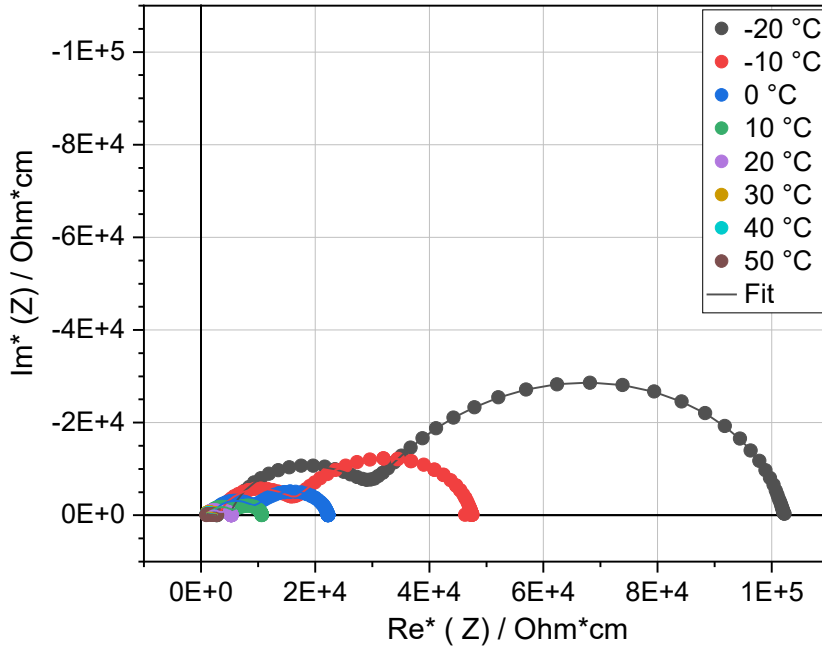


Figure 4.35 - Nyquist plot for symmetrical stack with NaSICON-type solid electrolyte, pressed at ambient temperature and measured in range -20°C - 50°C (Source: IKTS)

The conductivity for electrolyte material and through the interface has been calculated and depicted in function of $1/T$: in Fig. 4.36, it is showed the trend from measurements on Na07 stack, pressed at T_{amb} and 50°C in glovebox, divided in resulting conductivity through the electrolyte material and ability to move ions throughout the interface electrolyte-sodium. As intuitive, the increase of pressing temperature does not influence so much the electrolyte conductivity, but seems to be useful in the reduction of impedance across interface. For instance, the difference in $\sigma_{\text{electrolyte}}$ for measurement at -20°C is minimal ($2.25 \cdot 10^{-4}$ S/cm if the stack is pressed at T_{amb} , $2.70 \cdot 10^{-4}$ S/cm if pressed at 50°C), the same for measurement at 30°C ($1.36 \cdot 10^{-3}$ S/cm and $1.61 \cdot 10^{-3}$ S/cm, respectively). The ionic conduction through the interface instead, changes of one order of magnitude (from $2.54 \cdot 10^{-8}$ to $9.01 \cdot 10^{-7}$ S/cm at -20°C , from $1.34 \cdot 10^{-6}$ to $3.04 \cdot 10^{-5}$ S/cm at 30°C).

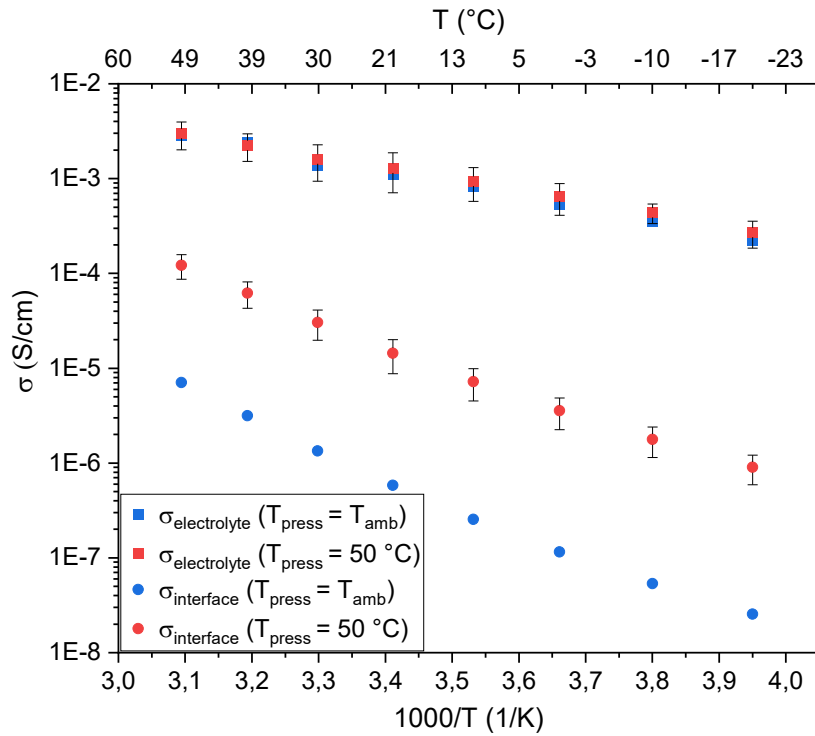


Figure 4.36 – Graph of conductivity in function of $1/T$, for symmetrical stack with Na07 solid electrolyte, pressed at ambient temperature and at 50 °C, measured in range -20 °C - 50 °C (Source: IKTS)

The deduction is confirmed in the analysis on NaSICON-type electrolyte, for which it seems that the higher pressing temperature positively influences the $\sigma_{\text{electrolyte}}$, as well.

The bar graph hereunder (Fig. 4.37) compares the results for investigation on Na07 and NaSICON electrolytes, at 30 °C, on ionic conduction through the electrolyte and the interface. A higher pressing temperature turns out to be a good solution, since enhancing the surface contact between anode material and electrolyte. For that procedure, the electrolyte ionic conductivity of the two materials is quite similar ($1.61 \cdot 10^{-3}$ S/cm for Na07, $1.65 \cdot 10^{-3}$ S/cm for NaSICON) and closed to the expected values at 25 °C from precedent studies. Concerning the ionic migration throughout the interface, the NaSICON guarantees a better performance, since enhanced of an order of magnitude with respect to the same parameter calculated for Na07 ($7.59 \cdot 10^{-4}$ S/cm for the former, $3.04 \cdot 10^{-5}$ S/cm for the latter).

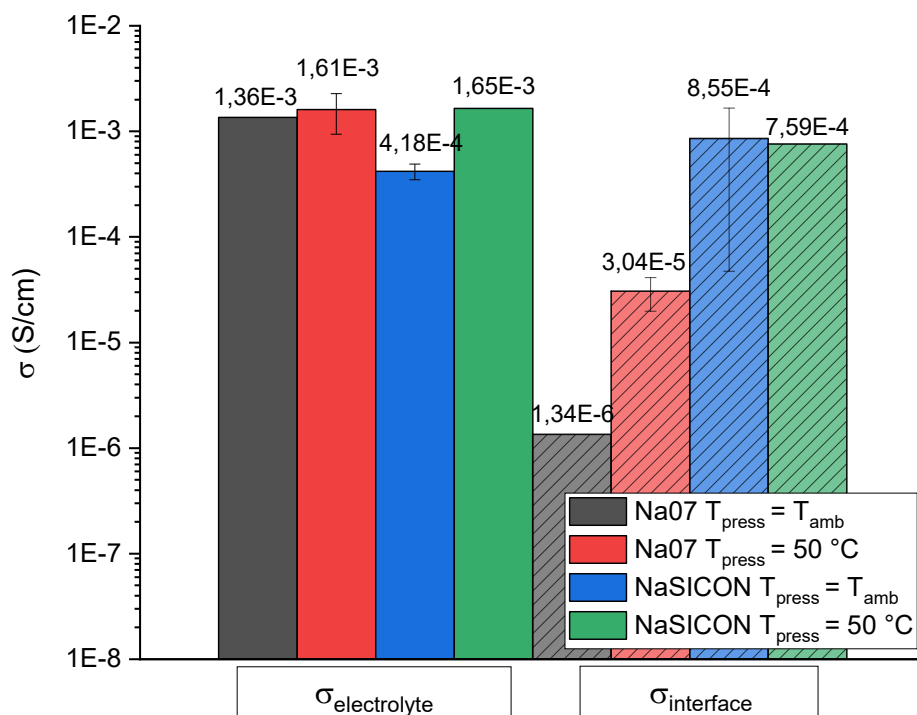


Figure 4.37 – Bar graph for comparison of ionic conduction through solid electrolyte and interface with metallic sodium, for stacks with Na07 and NaSICON-type electrolyte, pressed at T_{amb} and 50 °C, measured at 30 °C (Source: IKTS)

Thus, from the EIS analysis on symmetrical configuration, it comes out that with higher T_{press} during stacking, the performances in terms of ionic migration are enhanced. The $\sigma_{\text{electrolyte}}$ calculated at 30 °C confirms the expectations, for both the solid materials. The ionic conduction at interface, at 30 °C, ranges between 10^{-5} - 10^{-4} S/cm and seems to be better with the use of NaSICON as solid electrolyte.

Afterwards, the interface resistance has been analysed by combination of solid electrolyte materials with metallic Na as anode, and with NFP mixed with 5 %wt. of graphite as cathode. Before stacking, electrolyte and cathode slurry have been cofired according to the chosen sintering path (heating at 5 K/min up to 560 °C, with soaking time of 3 hours, in Varigon atmosphere). Next, the group has been stacked in glovebox with the anode layer and, similarly to the case of symmetrical configuration, submitted to EIS analysis.

The impedance data, only measured at 30 °C because of coupling with charge-discharge measurements, are presented in the Nyquist plot in Fig. 4.38, associated to the equivalent electrical circuit. The interface effects are modelled with one single R|C unit (n.3), considering both the interface with sodium and with the composite cathode. The

impedances in the bulk material and across the grain boundaries are modelled with the electrical circuits n.1 and n.2, respectively. In the previous analysis, the electrolyte was in contact with two equivalent metallic electrodes, therefore it has been possible to easily characterise the ionic conductivity of the electrolyte material and the conduction at interface with Na. In this case instead, one interface is coupled with the composite cathode: since the conductivity results are given as the sum of ionic conductivity in the electrolyte and in the composite electrode, the EIS spectrum is more complex to be interpreted.

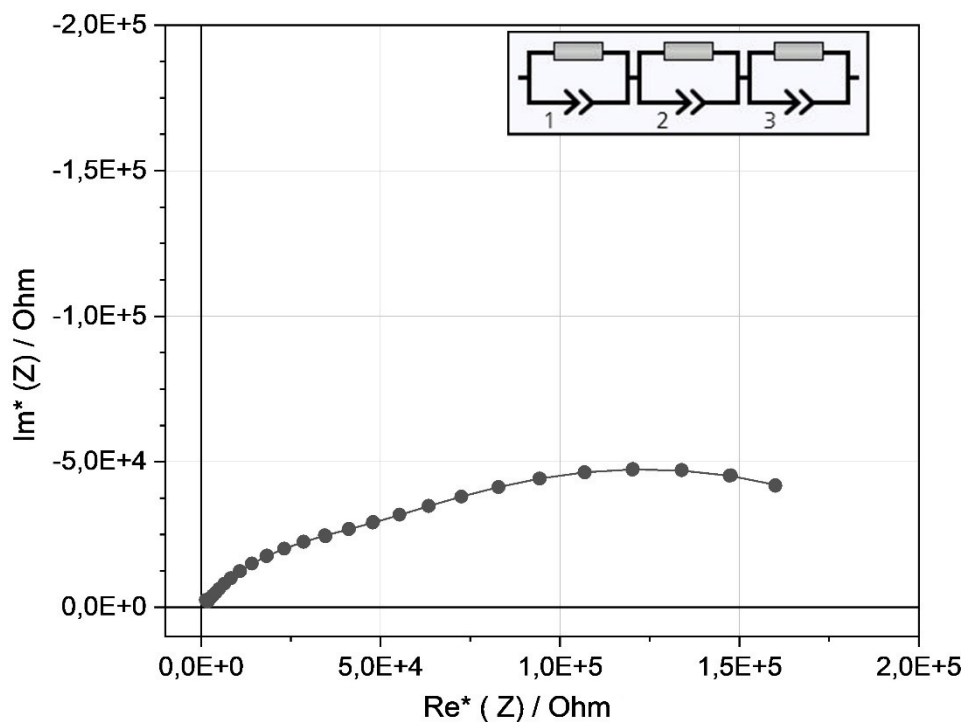


Figure 4.38 – Example of Nyquist plot for asymmetrical stack, here with NaSICON-type solid electrolyte, associated with equivalent electrical circuit (Source: IKTS)

The calculated conductivity values on samples stacked at 50 °C, present a general decrease with respect to the same results obtained with symmetrical configuration, as displayed in the bar graph hereunder (Fig. 4.39). The conductivity of electrolyte and composite electrode is reduced to $6.36 \cdot 10^{-5}$ S/cm for Na07 and to $3.50 \cdot 10^{-5}$ S/cm for NaSICON. Also, an extremely big impedance has been detected at the interface, leading to values of ionic conduction equal to $2.98 \cdot 10^{-8}$ S/cm for stacking with Na07, $5.86 \cdot 10^{-6}$ S/cm with NaSICON.

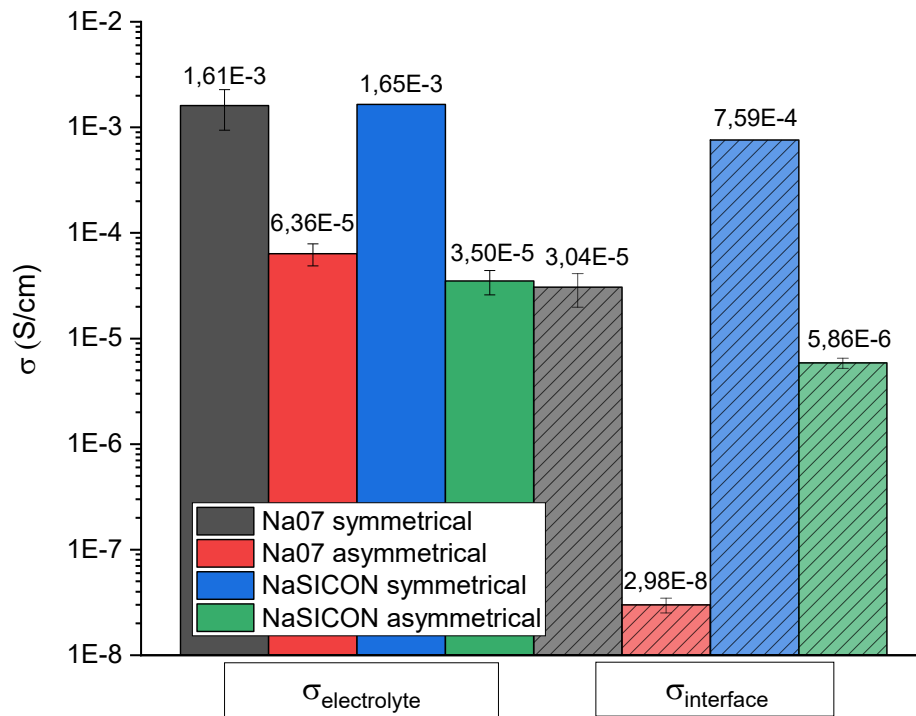


Figure 4.39 - Bar graph for comparison of ionic conduction through solid electrolyte and composite cathode, and interface, for stacks with Na07 and NaSICON-type electrolyte in symmetrical and asymmetrical configuration, pressed at 50 °C, measured at 30 °C (Source: IKTS)

Again, between the two solid electrolytes, the NaSICON-type seems to be the one with reduced impedance values and better ionic migration through electrolyte and interface.

The microstructural investigation with FESEM analysis shows a good cohesion at interface electrolyte-cathode material; a comparison between Na07 and NaSICON-type electrolytes, coupled with NFP-graphite, is depicted in Fig. 4.40. The electrolyte side is showed in the bottom part: as visible, the structure is dense and characterised by few pores; the difference in dark and light spots between the two is due to the distinct inner composition. The interface has the aspect of a tough junction with two materials, without visible cracks. The cathode material above, covered by an epoxy layer, presents densified NFP, spaced out by graphite layers.

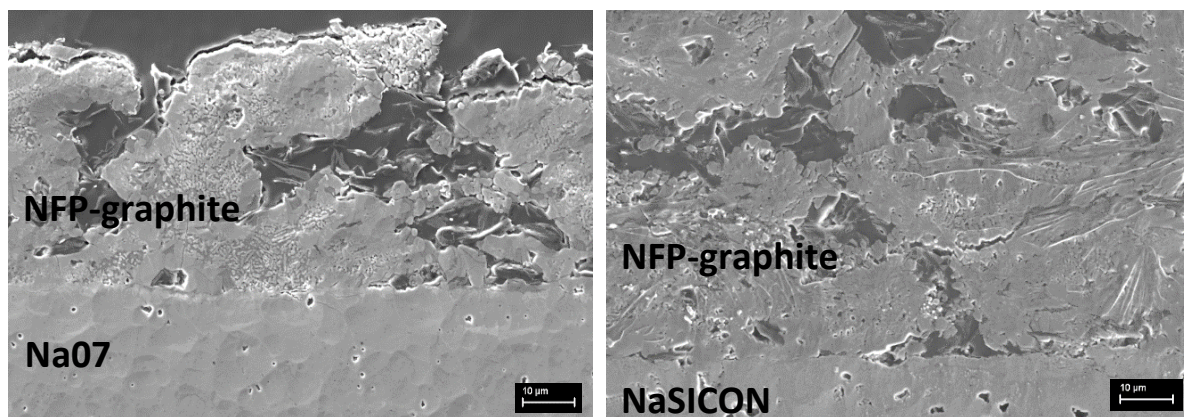


Figure 4.40 – FESEM images of Na07 (left) and NaSICON electrolyte structures (right) coupled with cathode material (Source: IKTS)

The EDX spectra made on Na07 coupled with cathode elements (Fig. 4.41) prove the good interface contact between the two materials: on electrolyte side (spectrum n. 82, 83), the detected elements are the constituting ones for the Na07 composition; on the cathode side, spectra n. 78, 79, 80 show the typical NFP elements, n. 77 identifies a layer of deposited graphite, n. 84 demonstrates the probable presence of $\text{Na}_4\text{P}_2\text{O}_7$ phase, because of the absence of Fe elements.



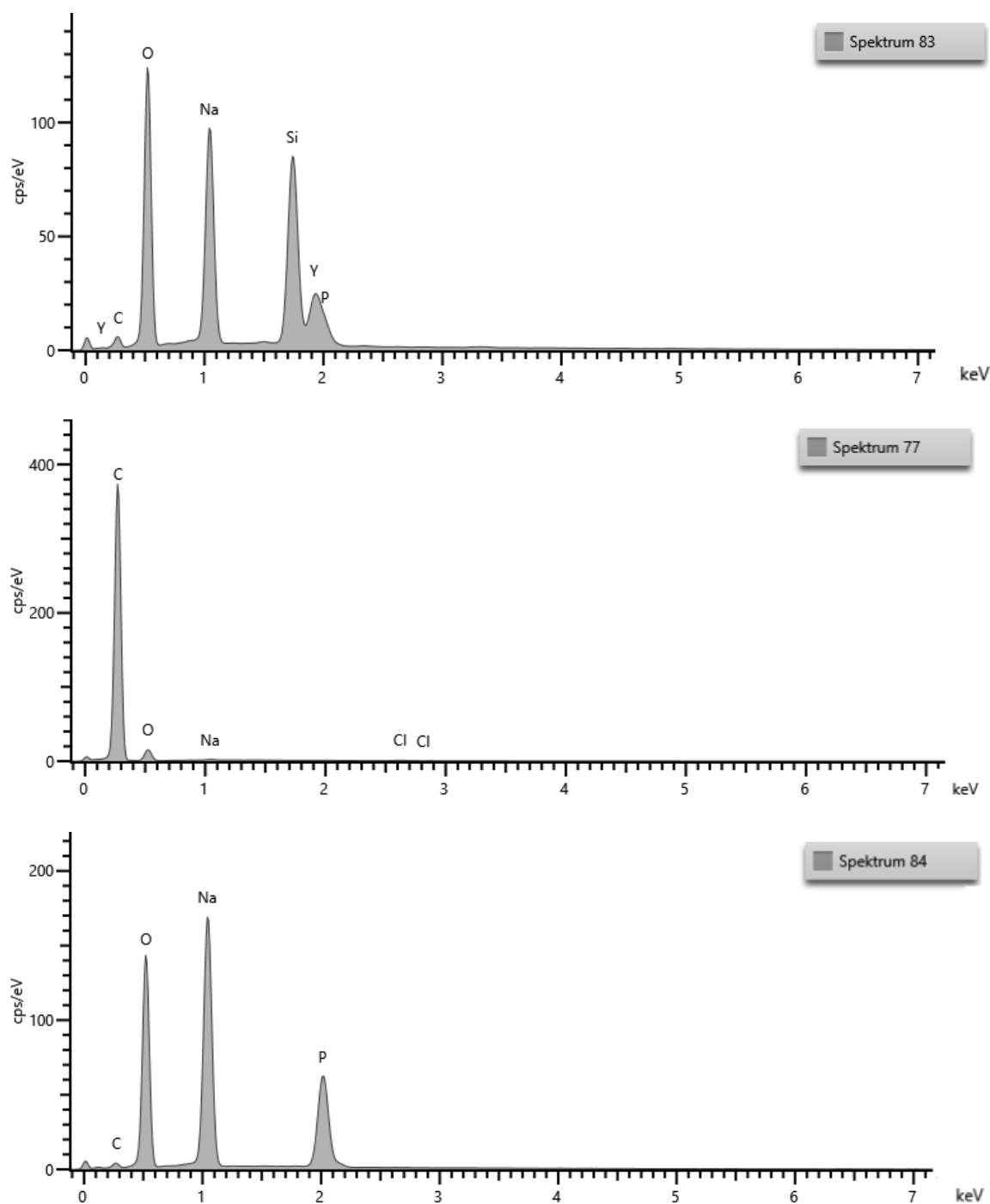


Figure 4.41 - FESEM image, associated to EDX spectra related to different points in the Na07 solid electrolyte-cathode structure (Source: IKTS)

The disposition of elements is similar for the coupling NaSICON-cathode material (Fig. 4.42): spectrum n. 89 highlights the elements composing the electrolyte structure, n. 86, 87 demonstrate the presence of carbon in the cathode and n. 85, 90 are typical for sodium-iron-phosphate composition.

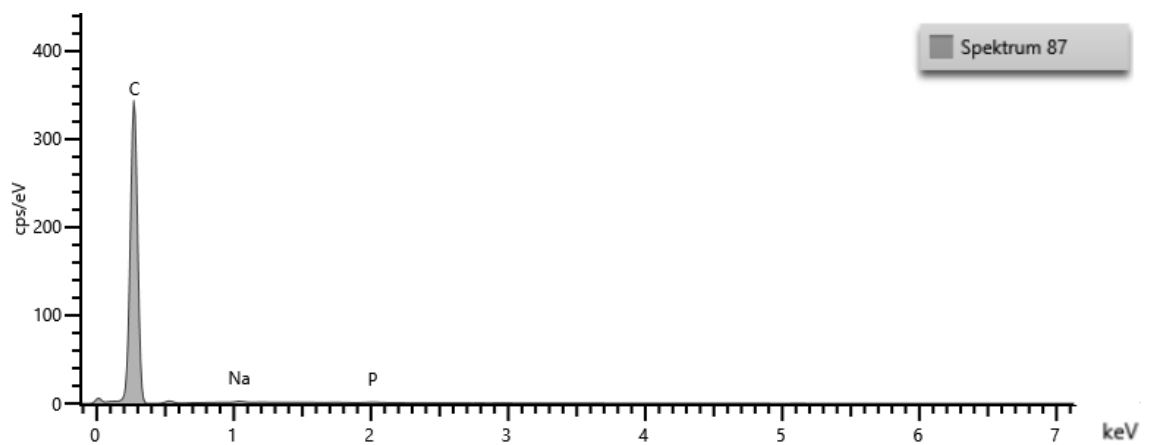
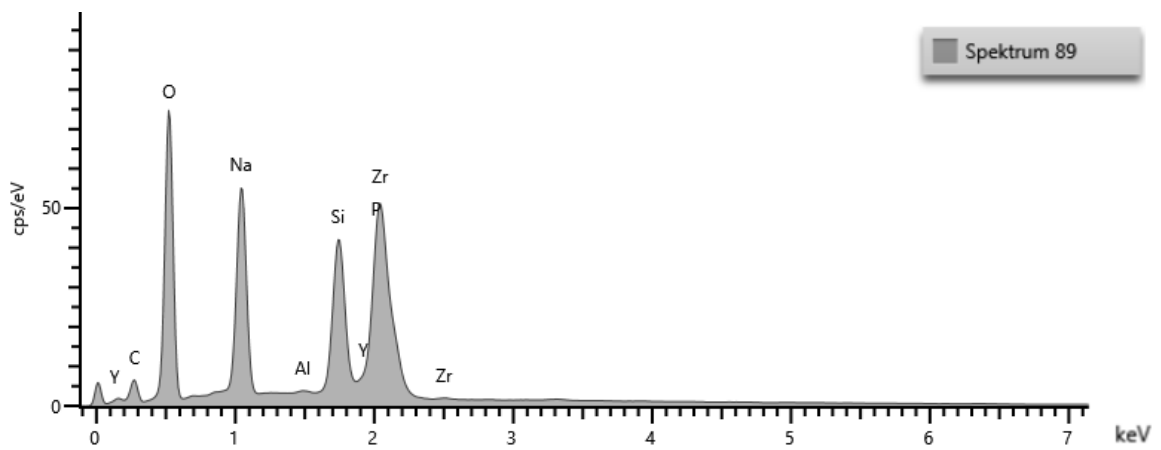
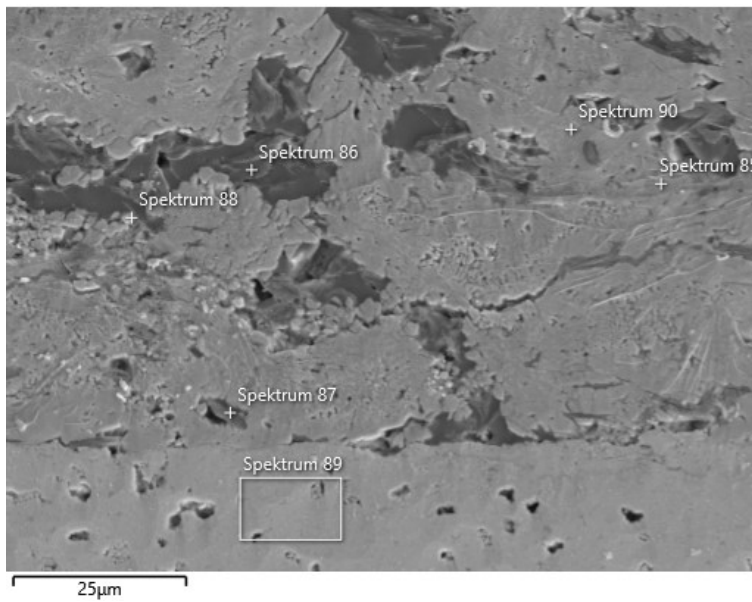


Figure 4.42 - FESEM image, associated to EDX spectra related to different points in the NaSICON solid electrolyte-cathode structure (Source: IKTS)

It is concluded that the ionic conduction across the interface is so reduced because of the ineffective migration through the interface with cathode material. The good interconnection showed in FESEM images suggests that the formation of a passivation layer is hardly improbable. Instead, one possible reason could be scarce presence of sodium in some spots, with consequent limitation of ionic movement in that direction; nonetheless, the type of reaction must still be identified and further investigations are requested.

Moreover, for future analyses it is suggested to intercalate some electrolyte powder in the cathode material mix [5]: in this way, the electrolyte particles should enhance the ionic conductivity and limit the strong impedance at interface with the two layers.

4.6 Electrochemical charge-discharge testing

The solid electrolytes, stacked in asymmetrical configuration with metallic sodium and sintered cathode material, have been subject to charge-discharge measurements to verify the feasibility and effectiveness of the system. The analysis mainly focused on structures pressed at 50 °C, for which the surface contact between solid electrolyte and sodium was enhanced. The results, achieved for measuring temperature of 30 °C, have been compared with performances from a system with conventional liquid electrolyte, tested at ambient temperature: following the preparation procedure from scientific publications [26], the testing have been made on a Swagelok cell employing 1 M NaClO₄ conductive salt (anhydrous, 98-102 %, Alfa Aesar) in PPC (anhydrous, 99,7 %, Sigma-Aldrich) with 5 %wt. of fluoroethylene carbonate (98 %, Alfa Aesar).

The results on stacks, pressed at 50 °C with Na07 solid electrolyte, are reported in the following graphs (Fig. 4.43, 4.44). The outcome is unsatisfactory, since voltage oscillates over limits during testing, and the charge-discharge curves present irrelevant values.

Measurements on stacks pressed at 50 °C with NaSICON-type electrolyte seem more promising (Fig. 4.45, 4.46): starting from OCV value of 2.5 V, the voltage oscillates in the defined range (2-3.8 V) and the charge-discharge curves are better defined, assuming the desired trend. Nonetheless, the capacity values are still not comparable with the ones from Literature studies [3,5,17]: if hypothesized 1 g of active material, the initial discharge capacity barely arrives to 0.01 mAh, while the reported values from scientific publications are around 80 mAh/g.

The reasons for the limited capacity values could be related to the intercalation of electrolyte particles in the electrode material, not performed because of the limited time to complete the experimental investigation in the institute.

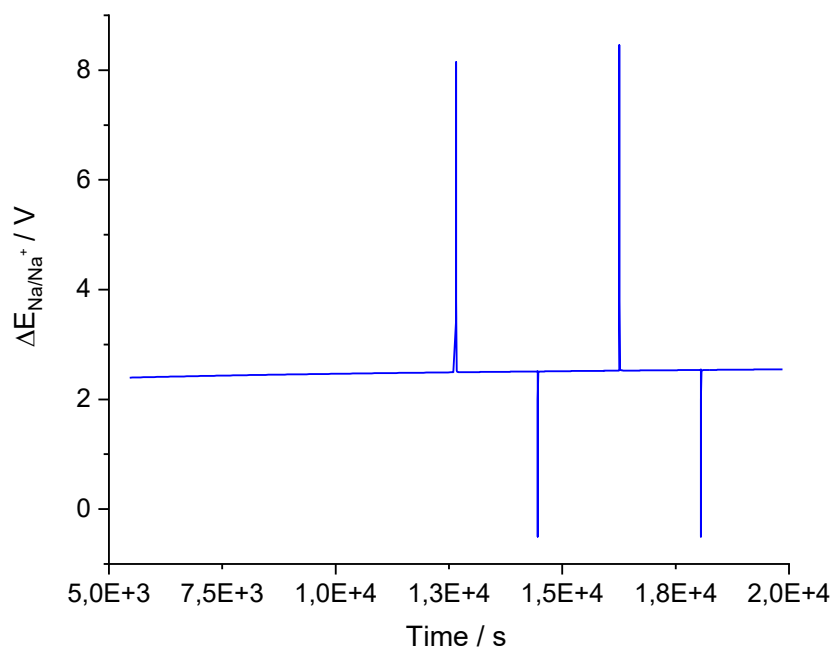


Figure 4.43 – Graph of voltage oscillation in function of time, for measurement on asymmetrical stack with Na07, charged at 30 °C and C/50 rate (Source: IKTS)

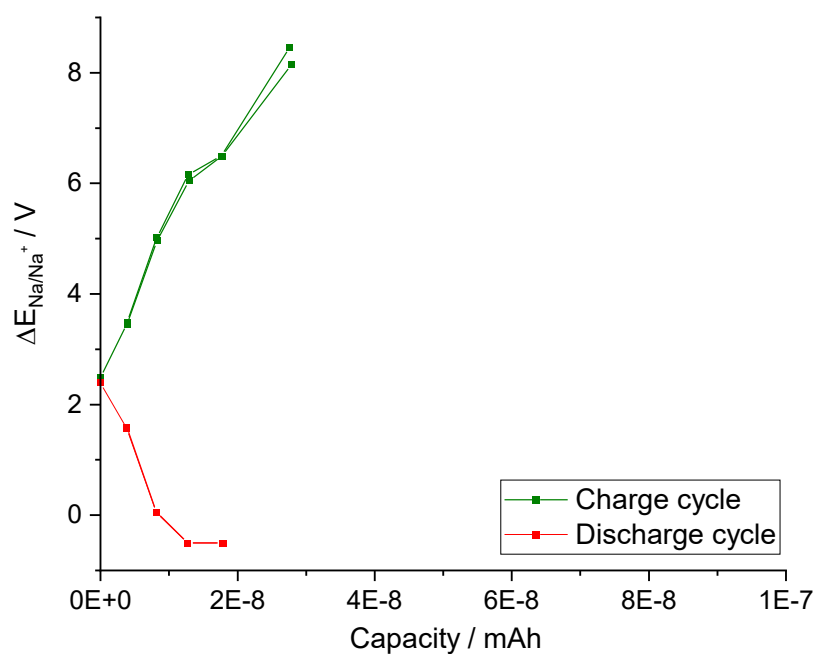


Figure 4.44 – Potential-capacity curve for measurement on asymmetrical stack with Na07, charged at 30 °C and C/50 rate (Source: IKTS)

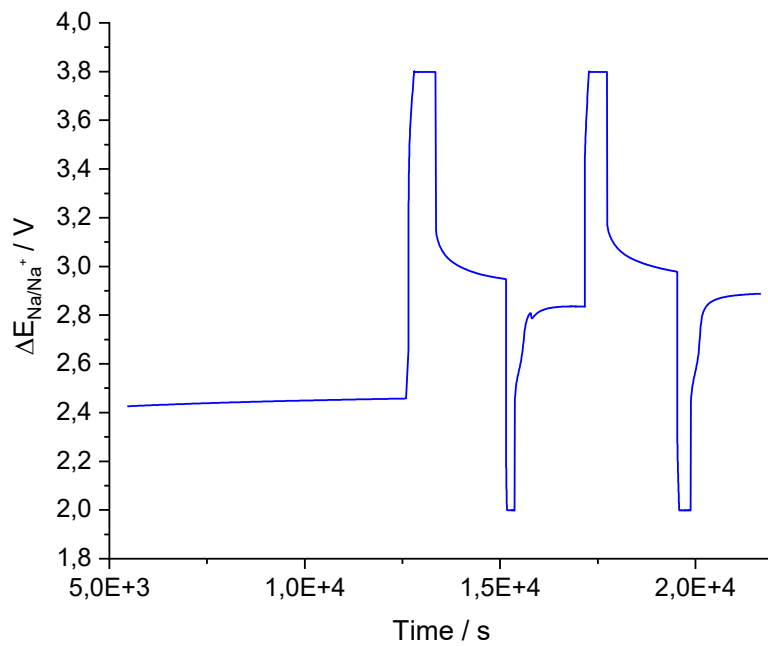


Figure 4.45 - Graph of voltage oscillation in function of time, for measurement on asymmetrical stack with NaSICON, charged at 30 °C and C/50 rate (Source: IKTS)

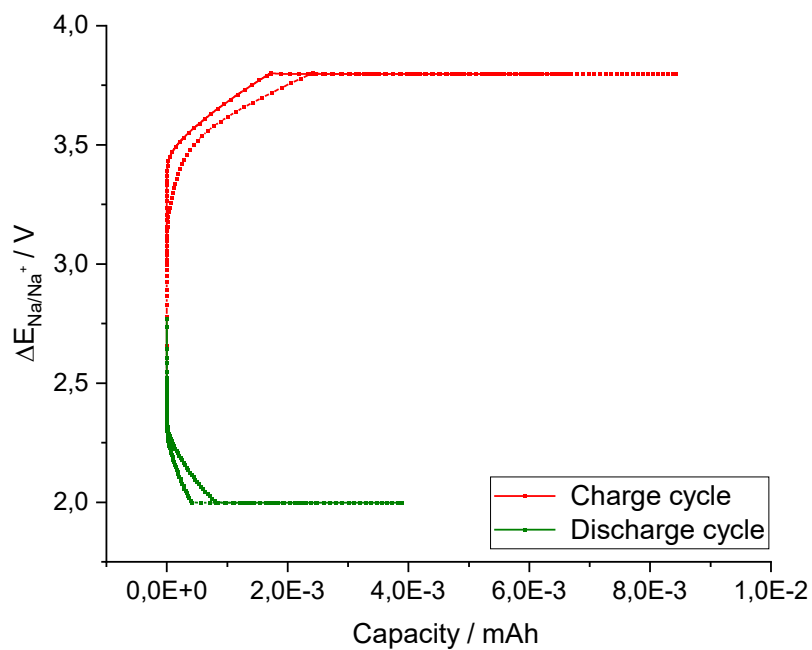


Figure 4.46 - Potential-capacity curve for measurement on asymmetrical stack with NaSICON, charged at 30 °C and C/50 rate (Source: IKTS)

On the other hand, the chosen composition demonstrates to be effective as cathode material, as deduced from measurements with conventional liquid electrolyte (Fig. 4.47). As anticipated in Chapter 2.7, the NFP material was reduced by sintering reaction (heating with 5 K/min rate up to 560 °C and soaking for 3 hours), re-pulverized and mixed with graphite as conductive agent, to be employed in a conventional porous battery; the ionic conductivity is ensured by the infiltration of liquid electrolyte in the electrodes.

Cycled with rate of C/10 for 25 cycles, the composition reports a good electrochemical activity: the voltage oscillates within defined limits (2-4 V) and potential-capacity curves present two plateaux (at 2.9 V and 2.5 V) corresponding to phases of Na extraction in the lattice, as reported in Literature [4,17]. The initial discharge capacity is obtained as 27.1 mAh/g, but still far from results from previous studies. The capacity values are quite constant during cycles: at the 25th, the measured discharge capacity is still 26.0 mAh/g, therefore showing a good C-efficiency during time (Fig. 4.48).

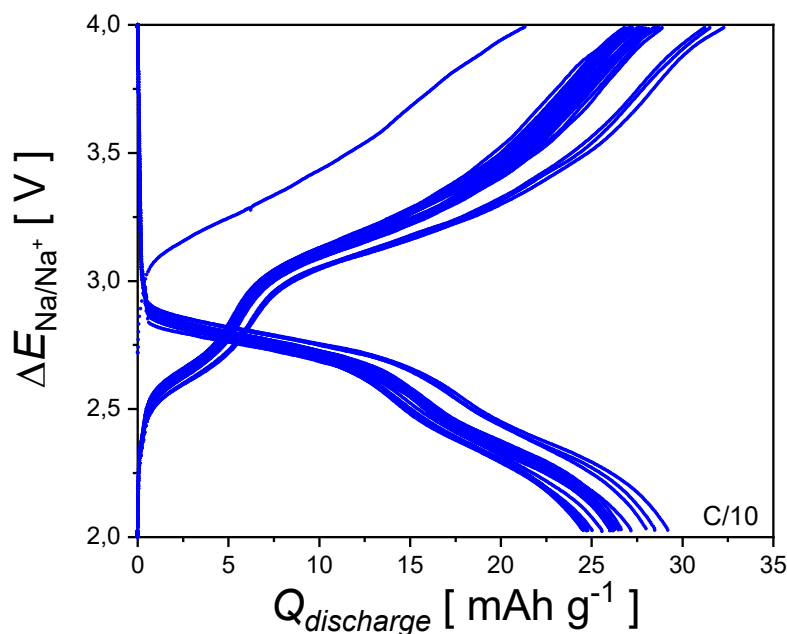


Figure 4.47 - Potential-capacity curves for measurement in Swagelok cell with conventional liquid electrolyte, charged at T_{amb} and C/10 rate (Source: IKTS)

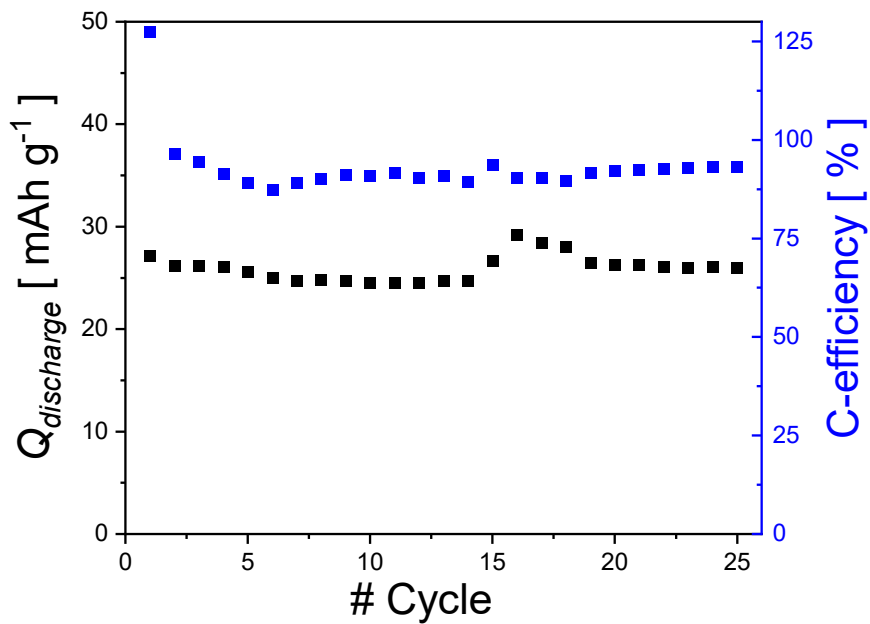


Figure 4.48 – Capacity and C-efficiency values increasing the number of cycles, for measurement in Swagelok cell with conventional liquid electrolyte, charged at T_{amb} and C/10 rate (Source: IKTS)

It is deduced that the chosen cathode composition and the performed sintering path are effective in the formation of active electrochemical material. The starting discharge capacity values could be still enhanced if the cathodic framework were formed by higher percentage of triclinic phase.

Anyway, the main issue is the coupling with a solid electrolyte, so the ionic migration at the interface level. The starting discharge capacity is dependent on operating temperature and on the cathodic thickness [5]: levelling and reducing the slurry layer applied on solid electrolyte tablet should be effective to reduce the resistance and improve the detected capacity. As already mentioned, further investigations should be focused on the intercalation of electrolyte powders in cathode material composition, as well.

Conclusions

The main goal of the investigation has been the sintering of a multicomponent composite cathode electrode, based on sodium-iron-phosphate glass with a desired crystalline modification, working as active material. From previous studies, it is proven the feasibility of a cathode active material mainly formed by triclinic crystalline structure as $\text{Na}_2\text{FeP}_2\text{O}_7$, to be coupled with solid electrolyte in a Na-ion solid state battery.

The first step has been the preparation of the parent amorphous glass, starting from sodium-iron-phosphate powders melt-quenched in oxidizing and reducing atmosphere.

Only the sintering process in inert or reduced atmosphere is effective to achieve a dense microstructure. By considering the realization of parent glass, the melting in oxidizing conditions (NFP glass) shows the more extended linear shrinkage during sintering.

Defined the reducing Varigon as the most suitable heating atmosphere, the heating treatment has been extended after the completion of the sintering step, to promote the desired phase formation: a 3 hours-long soaking time at heating temperature of 560 °C ensures the formation of high percentage of crystalline phases. In air instead, the detected crystalline phases are only formed by Fe^{3+} , proving the non-suitability of air treatment for the formation of proper cathode material.

The integration of 5 %wt. graphite as conductive additive promotes the cathode electronic conductivity and acts as additional reducing agent: the sintered framework is mainly formed by triclinic pyrophosphate $\text{Na}_{3.12}\text{Fe}_{2.44}(\text{P}_2\text{O}_7)_2$, hence identified by high content of Fe^{2+} .

The asymmetrical cell assembling has been carried out co-firing Na07 and NaSICON-type solid electrolytes with the composite cathode material, and pressing on the other side a layer of metallic sodium as anode component: the EIS analysis reveals the presence of a strong impedance, mainly related to the junction electrolyte-cathode.

The electrochemical testing with conventional liquid electrolyte confirms the effectiveness of NFP-graphite as active cathode material: the detected electrochemical activity shows good performance during the 25-cycles test. The investigation with solid electrolytes instead, reveals minimal values of electrochemical capacity. Between the

two, the NaSICON solid electrolyte shows better performances during the battery testing and smaller impedance at interface level with cathode.

Overall, the research demonstrates the feasibility of sintering procedure in the realization of a conductive cathode material, mainly formed by crystalline triclinic structure. The desired composition has been achieved controlling the heating atmosphere, heating rate, sintering temperature, soaking time and cathode material composition. The sintering process is effective in the formation of a strong and cohesive junction between cathode and solid electrolyte material.

The main issue to be solved is the ionic migration through the interface. The intercalation of electrolyte powders in the cathode structure is indicated in previous studies as crucial for increasing the ionic conduction between the two materials. Moreover, further investigation will be required concerning possible side reactions limiting the amount of sodium in the crystalline framework.

References

- [1] U.S. Energy Information Administration EIA, Annual Energy Outlook 2020, *January 2020*
- [2] Verónica Palomares, Paula Serras, Irune Villaluenga, Karina B. Hueso, Javier Carretero-González, Teófilo Rojo, Na-ion batteries, recent advances and present challenges to become low cost energy storage systems, *Energy Environ. Sci.*, 2012, 5, 5884
- [3] Tsuyoshi Honma, Noriko Ito, Takuya Togashi, Atsushi Sato, Takayuki Komatsu, Triclinic $\text{Na}_{2-x}\text{Fe}_{1+x/2}\text{P}_2\text{O}_7/\text{C}$ glass-ceramics with high current density performance for sodium ion battery, *Journal of Power Sources* 227 (2013), 31-34
- [4] Yubin Niu, Yan Zhang, Maowen Xu, A review on pyrophosphate framework cathode materials for sodium-ion batteries, *Journal of Materials Chemistry A* 7 (2019), 15006-15025
- [5] Hideo Yamauchi, Junichi Ikejiri, Fumio Sato, Hiroyuki Oshita, Tsuyoshi Honma, Takayuki Komatsu, Pressureless all-solid-state sodium-ion battery consisting of sodium iron pyrophosphate glass-ceramic cathode and β'' -alumina solid electrolyte composite, *J. Am. Ceram. Soc.* 102 (2019), 6658-6667
- [6] Robert A. Huggins, *Advanced Batteries – Materials Science Aspects*, 2009, Springer
- [7] Karina B. Hueso, Michel Armand and Teófilo Rojo, High temperature sodium batteries: status, challenges and future trends, *Energy Environ. Sci.*, 2013, 6, 734
- [8] Joo Gon Kim, Byungrak Son, Santanu Mukherjee, Nicholas Schuppert, Alex Bates, Osung Kwon, Moon Jong Choi, Hyun Yeol Chung, Sam Park, A review of lithium and non-lithium based solid state batteries, *Journal of Power Sources* 282 (2015), 299-322
- [9] Marie Guin, Chemical and physical properties of sodium ionic conductors for solid-state batteries, *Energy & Environment* (2017), Vol. 373

- [10] Jang Wook Choi and Doron Aurbach, Promise and reality of post-lithium-ion batteries with high energy densities, *Nature Reviews – Materials* (2016), Vol. 1
- [11] Naoaki Yabuuchi, Shinichi Komaba, Recent research progress on iron- and manganese-based positive electrode materials for rechargeable sodium batteries, *Sci. Technol. Adv. Mater.* 15 (2014), 043501
- [12] Cristina Tealdi, Monica Ricci, Chiara Ferrara, Giovanna Bruni, Eliana Quartarone and Piercarlo Mustarelli, Electrochemical Study of $\text{Na}_2\text{Fe}_{1-x}\text{Mn}_x\text{P}_2\text{O}_7$ ($x = 0, 0.25, 0.5, 0.75, 1$) as Cathode Material for Rechargeable Na-Ion Batteries, *Batteries* 2016, 2, 1
- [13] M. J. Pascual, A. Durán, L. Pascual, Sintering process of glasses in the system $\text{Na}_2\text{O}-\text{B}_2\text{O}_3-\text{SiO}_2$, *Journal of Non-Crystalline Solids* 306 (2002), 58-69
- [14] Yong Lu, Lin Li, Qiu Zhang, Zhiqiang Niu and Jun Chen, Electrolyte and Interface Engineering for Solid-State Sodium Batteries, *Joule* 2 (2018), 1747-1770
- [15] Mark Ladd, Rex Palmer, Structure Determination by X-ray Crystallography – Analysis by X-rays and Neutrons, *Fifth Edition* (2013), Springer
- [16] Joseph I. Goldstein, Dale E. Newbury, Joseph R. Michael. Nicholas W.M. Ritchie, John Henry J. Scott, David C. Joy, Scanning Electron Microscopy and X-Ray Microanalysis, *Fourth Edition* (2018), Springer
- [17] Tsuyoshi Honma, Takuya Togashi, Noriko Ito and Takayuki Komatsu, Fabrication of $\text{Na}_2\text{FeP}_2\text{O}_7$ glass-ceramics for sodium ion battery, *Journal of the Ceramic Society of Japan* 120 (2012), 344-346
- [18] Tsuyoshi Honma, Atsushi Sato, Noriko Ito, Takuya Togashi, Kenji Shinozaki, Takayuki Komatsu, Crystallization behavior of sodium iron phosphate glass $\text{Na}_{2-x}\text{Fe}_{1+0.5x}\text{P}_2\text{O}_7$ for sodium ion batteries, *Journal of Non-Crystalline Solids* 404 (2014), 26-31
- [19] Vadim F. Lvovich, IMPEDANCE SPECTROSCOPY – Applications to Electrochemical and Dielectric Phenomena, (2012) John Wiley & Sons, Inc.
- [20] A. Mannschatz, J. Schilm, A. Müller-Köhn, T. Moritz, Glass-Carbon-Composites for Heating Elements Manufactured by 2C-PIM, *Ceramic Applications* 5 (2017) [2], 2-3

- [21] Sahir Naqash, Qianli Ma, Frank Tietz, Olivier Guillon, $\text{Na}_3\text{Zr}_2(\text{SiO}_4)_2(\text{PO}_4)$ prepared by a solution-assisted solid state reaction, *Solid State Ionics* 302 (2017), 83-91
- [22] E. M. Rabinovich, Review Preparation of glass by sintering, *Journal of Materials Science* 20 (1985), 4259-4297
- [23] Ranjusha Rajagopalan, Bo Chen, Zhicheng Zhang, Xing-Long Wu, Yonghua Du, Ying Huang, Bing Li, Yun Zong, Jie Wang, Gwang-Hyeon Nam, Melinda Sindoro, Shi Xue Dou, Hua Kun Liu, Hua Zhang, Improved Reversibility of $\text{Fe}^{3+}/\text{Fe}^{4+}$ Redox Couple in Sodium Super Ion Conductor Type $\text{Na}_3\text{Fe}_2(\text{PO}_4)_3$ for Sodium-Ion Batteries, *Advanced Materials* 29 (2017), 1-8
- [24] Wen-bin Dai, Yu Li, Da-qiang Cang, Yuan-yuan Zhou, Yong Fan, Effects of sintering atmosphere on the physical and mechanical properties of modified BOF slag glass, *International Journal of Minerals, Metallurgy and Materials*, Vol. 21, n. 5 (2014), 494
- [25] C. Masquelier, F. D'Yvoire, N. Rodier, Crystal Structure of the Sodium Ion Conductor $\alpha\text{-Na}_7\text{Fe}_3(\text{P}_2\text{O}_7)_4$: Evidence for a Long-Range Ordering of the Na^+ ions, *Journal of Solid State Chemistry* 95 (1991), 156-167
- [26] Prabeer Barpanda, Guandong Liu, Chris D. Ling, Mao Tamaru, Maxim Avdeev, Sai-Cheong Chung, Yuki Yamada, and Atsuo Yamada, $\text{Na}_2\text{FeP}_2\text{O}_7$: A Safe Cathode for Rechargeable Sodium-ion Batteries, *Chem. Mater.* 2013, 25, 17, 3480-3487